OBSERVATIONS OF SURFACE CURRENTS IN PANAY STRAIT, PHILIPPINES

A DISSERTATION SUBMITTED TO THE GRADUATE DIVISION OF THE UNIVERSITY OF HAWAI'I AT MĀNOA IN PARTIAL FULFILLMENT OF THE REQUIREMENTS FOR THE DEGREE OF DOCTOR OF PHILOSOPHY

IN

OCEANOGRAPHY

December 2016

By

Charina Lyn A. Repollo

Dissertation Committee:

Pierre Flament, Chairperson

Mark Merrifield

Glenn Carter

Francois Ascani

Camilo Mora

We certify that we have read this dissertation and that, in our opinion, it is satisfactory in scope and quality as a dissertation for the degree of Doctor of Philosophy in Oceanography.

DISSERTATION COMMITTEE

_____
Chairperson

_____

_____

_____

_____

Acknowledgements

This thesis is the result of hard work whereby I have been accompanied and supported by many people. This is an opportunity for me to express my gratitude for all of them.

I am indebted to the Office of the Naval Research (ONR) through the Philippine Strait Dynamics Experiment (PhilEx) program for the funding support (grant N00014-09-1-0807 to Pierre Flament). To the dedication and skill of the Captain and crew of the R/V Melville and the many U.S. and Philippine students, technicians, volunteers, and scientists who participated, assisted and helped in the fieldwork. Janet Sprintal provided the moored shallow pressure gauges and ADCP data (ONR grant N00014-06-1-690), Craig Lee provided the TRIAXUS data, and Julie Pullen provided the COAMPS winds.

I would like to express my sincere gratitude to my advisor, Pierre Flament, for his patience, motivation and intellectual support. His guidance helped me a lot in all the time of research and writing of this thesis. Also his overly enthusiasm and integral view on research and his dedication towards work has made a deep impression on me. To the other members of my Ph.D. committee, Mark Merrifield, Glenn Carter, Francois Ascani and Camilo Mora for their insightful comments and feedbacks.

I would not have succeeded without the help and support of teams from both the Physical Oceanography Laboratory of the Marine Science Institute, University of the Philippines and the Radio Oceanography Laboratory of the Department of Oceanography, University of Hawai'i at Manoa with radar installation, operation and and maintenance. To Xavier Flores-Vidal who supervised and helped in the field, and taught the initial processing of the data. To Cedric Chavanne who picked me up from the airport when I first arrived at UH and for all his helped on data processing. To Tyson Hilmer for calibration of HF radar and Paul Lethaby for his help on PhilEx data management. Administrative assistance was provided by the Ocean Office particularly, Kristin Momohara, Catalpa Kong, and Lance Samura.

I thank my fellow labmates for the fruitful and stimulating discussions, for all the tiring but fun fieldwork we had, and for the sleepless nights we were working together before deadlines. To the graduate students of Radio Oceanography lab for the friendship and sharing scientific discussions and feedback on this work, particularly Jake Cass, Victoria Futch, Lindsey Benjamin, Alma Castillo, and Ian Quino Fernandez. My cohort, Sherril

Leon Soon, Pavica Srsen, Saulo Soares, Huei-Ting Lin and Eunjun Kim. Also to Yannek Meunier for sharing the opportunity working with radars in the Philippines.

I also appreciate the unyielding moral support from my fellow Filipino students and friends, our family away from home. Lots of gratitude to Cesar Villanoy, who inspired and paved the way to pursue this further studies. Together with Laura David, they play a big part in this Ph.D. journey. Special thanks to Benedicte Dousset for all her support, encouragement and inspiration. Her stories motivated and helped me a lot in staying on the right track. To my family for their unconditional love and support.

And my heartfelt thanks to my husband, Jhobert whose patient love enabled me to complete this work. To Hayden and Kaimalie for changing my life for the better. Words cannot express how grateful I am for all your love and sacrifices on my behalf. You taught me the good things that really matter in life.

Above all my deepest and sincere gratitude to OUR CREATOR for inspiring and guiding this humble being.

Lastly, I would like to thank many individuals, friends and colleagues who have not been mentioned here personally in making this educational process a success. I could not make it without your support.

...

Abstract

OBSERVATIONS OF SURFACE CURRENTS IN PANAY STRAIT, PHILIPPINES

High Frequency Doppler Radar (HFDR), shallow pressure gauges (SPG) and Acoustic Doppler Current Profiler (ADCP) time-series observations during the Philippine Straits Dynamics Experiment (PhilEx) were analyzed to describe the tidal and mesoscale currents in Panay Strait, Philippines.

Low frequency surface currents inferred from three HFDR (July 2008 – July 2009), reveal a clear seasonal signal concurrent with the reversal of the Asian monsoon. A mesoscale cyclonic eddy west of Panay Island is generated during the winter Northeast (NE) monsoon. This causes changes in the strength, depth and width of the intraseasonal Panay coastal (PC) jet as its eastern limb. Winds from QuikSCAT and from a nearby airport indicate that these flow structures correlate with the strength and direction of the prevailing local wind.

An intensive survey in February 8-9, 2009 using 24-hour of successive cross-shore Conductivity - Temperature - Depth (CTD) sections, which in conjunction with shipboard ADCP measurement show a well-developed cyclonic eddy characterized by near-surface velocities of 50 cm/s. This eddy coincides with the intensification of the wind in between Mindoro and Panay Islands generating a positive wind stress curl in the lee of Panay, which in turn induces divergent surface currents. Water column response from the mean transects show a pronounced signal of upwelling, indicated by the doming of isotherms and isopycnals. A pressure gradient then is set up, resulting in the spin-up of a cyclonic eddy in geostrophic balance. Evolution of the vorticity within the vortex core confirms wind stress curl as the dominant forcing.

The Panay Strait constitutes a topographically complex system that is the locale of intense tidal currents. The four major tidal constituents in the total energy spectra inferred from sea level and current profile are K_1, O_1, M_2, and S_2. In terms of spatial variability, O_1 and M_2 are the dominant diurnal and semi-diurnal constituents, respectively. The diurnal tide accounts for the highest variability over the shallow shelf while semi-diurnal tides dominate over the deeper channel of the strait. In addition, inertial frequency peaks

and exhibits an unusually broad spectra between the clockwise and counterclockwise components, possibly shifted by the vorticity of sub-inertial currents prevalent in the region. Vertically, major tidal components in the velocity profile appear in two distinct layers: at 110 m, 10.7% of the variance is associated with semi-diurnal tides, and at 470 m, 16.6% of the variance is due to diurnal tides (K_1 and O_1). Tidal current ellipses of semi-diurnal constituents (M_2 and S_2) exhibit a dominant clockwise motion in time at near-surface depth (110 m), indicative of downward energy propagation and implying a surface energy source. These features observed in the ADCP deployed close to the sill may explain the dominant semi-diurnal tide from the HFDR over the channel of the strait. Comparison of incoherent to coherent tidal energy shows coherent energy is dominant over the shallow Cuyo shelf for both diurnal and semi-diurnal tides while incoherent energy is stronger over the channel, distinctly over the sill and the constricted part of the strait. The incoherent portion of the tide is presumably attributable to the surface expression of the internal tide which seems to be generated near the sill and then is topographically steered west over the edge of the shallow shelf where incoherent energy is dominant.

Contents

List of Figures

Chapter 1

Introduction

Along the Pacific Ocean's western margins lie the Philippine Islands, a northern segment of an archipelago stretching from Southeast Asia to Australia. This island chain constrains the flow between the tropical western Pacific and eastern Indian oceans into a complex configuration of narrow straits and seas of various sizes. This area is subject to the reversal of the Asian monsoon, inter-annual variations such as the El Niño Southern Oscillation (ENSO), and episodic occurrences (e.g monsoon surges and tropical cyclones), making it challenging to observe and model. The Office of Naval Research (ONR) sponsored the PhilEx with a goal of exploring the oceanography and dynamics in the narrow straits and deep basins of the Philippines using integrated in-situ and remote observational methods with global and regional model components [Gordon and Villanoy, 2011].

Flows through Philippine straits are modulated by a range of processes at different spatial and temporal scales. Previous work in the region using ship-drift data [Wrytki, 1961] identified the role of the Asian monsoon in directing the surface flow between the South China Sea (SCS) and the Sulu Sea through the Mindoro Strait-Panay Strait complex (Figure 1.1). During the peak of the Northeast (NE: December-March) monsoon, Pacific Ocean surface waters enter westward through the Surigao and San Bernardino Straits into the Sulu Sea, and exit northward through Mindoro into the SCS and southward through Sibutu Passage into the Sulawesi Sea [Wrytki, 1961]. During the Southwest (SW: June–September) monsoon the surface flow is southward from the SCS in Mindoro Strait,

and circulation within the Sulu Sea is cyclonic [Wrytki, 1961]. However, observations from ship drift records are too scanty and do not give a complete picture of the circulation.

Pullen et al. [2008] used a one-way coupled high-resolution atmosphere and ocean simulation of the Philippine region, to highlight the importance of topographically-induced wind shear in forcing the surface ocean. Monsoon surge events prevalent during winter induce the generation and migration of pairs of counter-rotating oceanic eddies caused by intensified wind jets and wakes in the lee of Luzon and Mindoro. Comparison of high-resolution model and observed near-surface currents in the Philippine Archipelago, also confirmed the strong eddy flow pattern within Mindoro Strait and west of Panay [Han et al., 2009].

A time series of observed velocity and properties from moored ADCP in Mindoro and Panay Straits over a year (2008) revealed a complex response to the surface monsoonal forcing [Sprintall et al., 2012]. ADCP measurements in the upper layer in Mindoro Strait show a distinctly seasonal cycle with northward flow during the boreal summer SW monsoon and southward flow during the winter NE monsoon. In contrast, upper layer flow in Panay Strait is intra-seasonal with no clear monsoonal relationship. It has been suggested that regional wind forcing dynamics are responsible for the upper layer transport variability. Local winds shift the location of the jets and eddies prevalent in the region, and subsequently lead to intermittent reversals and more variable upper layer transport observed in Panay Strait [Sprintall et al., 2012].

Previous studies in Panay Strait, however were inferred from models with known errors, such as coarse resolution, inaccuracy of forcing fields, incorrect heat flux and freshwater parameterizations, and lack of river outflow [Han et al., 2009]. At the same time, missing data in the upper 40m from the moored ADCP [Sprintall et al., 2012] make the connection of the near-surface flow to the monsoon variability problematic. The vertical profiles of currents by single-point moored ADCP also compromise the estimation of across-passage transport [Sprintall et al., 2012]. ADCP data therefore do not fully resolve the spatial and temporal variability of the surface layer flow.

Intensive observations of Panay Strait were carried out to qualitatively and quantitatively describe the mesoscale spatial structure and temporal variability of the surface current within the strait. Measurements of surface currents from three HFDR during the PhilEx program were analyzed to characterize the dominant low-frequency surface flows,

investigate its forcing mechanisms, and determine the structure of the barotropic and baroclinic tides. Analyses were done in conjunction with the wind data from QuikSCAT and from a nearby airport, two SPG, one ADCP mooring, hydrographic data, modeled wind from Coupled Ocean/Atmosphere Mesoscale Prediction System (COAMPS), and satellite images of sea surface temperature, ocean color, and wind speed.

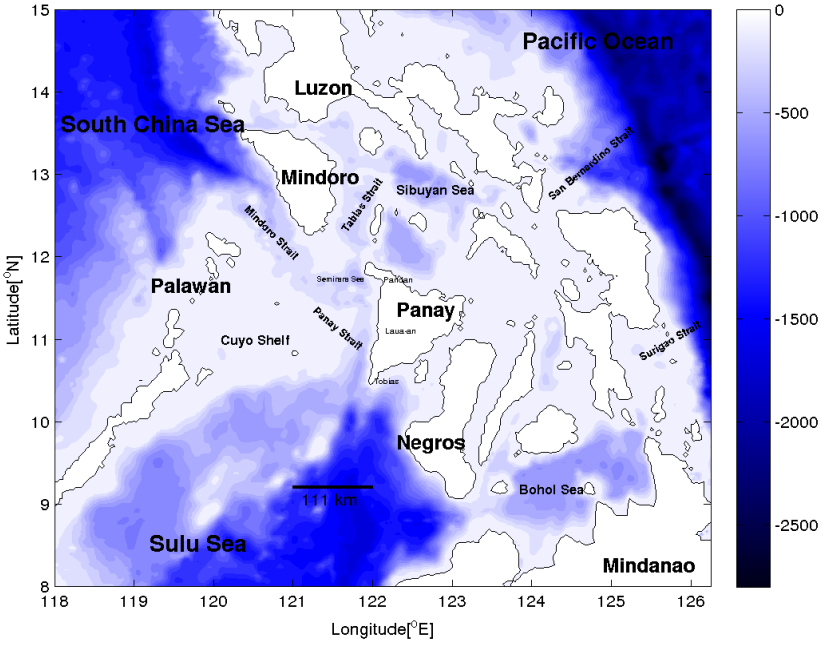

FIGURE 1.1: Bathymetric map showing the major straits and basins of the Philippine archipelago. Bathymetry contours are in meters.

Chapter 2

Environmental and Instrumental Setting

2.1 Physical Setting

The Panay Strait serves as the major pathway of South China Sea water entering through Mindoro Strait into the deep Sulu Sea basin (Figure 2.1). The strait is bounded by the coast of Panay Island on the east and the Palawan Island chain on the west. Along Panay, the shelf is narrow (less than 10 km) while the northern Palawan shelf extends eastward as the shallow Cuyo Shelf. This then forms a deep channel close to the coast of Panay, based on 100 m isobath with sill depth of about 570 m deep. On the shelf lies the low-lying Cuyo Group of Islands and extensive reefs.

The flow within the strait is modulated by a range of processes such as tidal variations, seasonal reversal of the monsoon, sea level variations between SCS and the Pacific Ocean, interannual variations such as ENSO, and episodic occurrence of monsoon surges and tropical cyclones [White et al., 2003; McClean et al., 2005; Pullen et al., 2008; Han et al., 2009; May et al., 2011].

2.2 Instrumental Setting

Three short-wave ocean current-mapping radars were deployed along the west coast of Panay Island to measure surface circulation from July 2008 to August 2009 during the PhilEx program (Figure 2.1). This observational component aims to quantitatively describe the mesoscale spatial structure and the temporal variability of the surface currents within Panay Strait. The antenna at each site are grouped in a receive array and a transmit array. The northernmost and southernmost sites located in Pandan and Tobias Fornier, respectively, include a linear array of 12 receiving antenna, whereas the middle site at Laua-an consists of a linear array of 8 receiving antenna. The four transmit antenna arranged in a rectangular array formed a beam toward the ocean, and a null in the direction of the receive antennas, to reduce the direct path energy. This also reduced the range away from the beam axis.

For each HFDR, radial currents are measured by transmitting a radio signal at 12 Mhz frequency. The radio waves are reflected by surface gravity waves having half the electromagnetic wavelength (λ =25 m, Bragg scattering) of the transmitted signal, and are then recorded by the receive antenna. The backscattered radio waves generate a Doppler shifted signal in which the frequency shift is used to calculate the currents moving toward or away from the site. Vector currents were estimated on a 5 km Cartesian grid by least-square fitting zonal and meridional components of the radial measurements from three sites within a 5 m search radius. The range of HFDR data used for analysis was limited by geometric dilution of precision (GDOP, Figure 2.2) that resulted from the normal velocity component being poorly constrained near the baseline between the sites and the azimuthal component poorly constrained far from the sites. Vector current estimations with a GDOP greater than 0.5 were discarded [Chavanne et al., 2007].

Periodically missing observations at long ranges (presumably due to diurnal variation of ionospheric propagation and absorption) were resolved by linear interpolation carried out on the vector currents (see Appendix B, after [Chavanne et al., 2007]). The least square analysis was carried out on the interpolated time series. Temporal coverage of the individual sites and of vector current estimations are shown in (Figure 2.3). Vector currents with 75% temporal coverage were used for analysis.

Failures in HFDR occurred at sites due to electrical power loss primarily because of burned power cables and generator failures during black-outs. In times when data were lost from one site, two sites were used to calculate vector currents. During the deployment period, the largest data loss was during the bistatic calibration performed from December 22, 2008 to January 9, 2009.

Data quality was evaluated by cross correlations between radial currents from pairs of sites (Figure 2.4). If along-baseline and across-baseline current components were uncorrelated with equal variance, the correlation pattern would follow that of the cosine of the angle between the two sites, indicating accuracy of measurements (Appendix C, [Chavanne et al., 2007]). To further assess the accuracy of the HFDR, beam forming calibration onboard a motorized boat was also conducted for each of the three sites.

In conjunction with the HFDR, an ADCP mooring was deployed as part of the PhilEx Exploratory Cruise onboard the R/V Melville in June 2007 to provide aspects of the full three-dimensional circulation in Panay strait. An upward-looking RDI Long Ranger 75 kHz, bottom mounted ADCP was located inside the region covered by HFDR, 2.5 km downstream from the narrowest constriction of Panay Sill at 578 m water depth. The ADCP included pressure and temperature sensors. Sampling rates, set to resolve the tides, were 30 minutes for the ADCP and 15 minutes for the temperature and salinity sensors. The mooring was recovered in March 2009. The ADCP returned 100% of the velocity time series. However, due to surface reflection contamination, the bottom-mounted ADCP was unable to resolve the near surface velocity (upper 50 m). Pressure time series were corrected from mooring blowover. The velocity data were then linearly interpolated in the vertical onto a 10 m depth grid and a common time base of 1 hour.

The gridded daily wind vector and wind stress fields, estimated over global ocean from QuikSCAT scatterometer were obtained online at IFREMER (`ftp://ftp.ifremer.fr.fr/ifremer/cersat/products/gridded/MWF/L3/QuikSCATDaily`). The daily wind fields were calculated for the full QuikSCAT V3 period: October 1999-November 2009 with spatial resolution of 0.25° in longitude and latitude. The reference height of wind data is 10 m. This new scatterometer product is assumed to have improved wind speed performance in rain and at high wind conditions. In addition, in-situ 10 m daily wind data from the nearby Caticlan Airport was obtained (Figure 2.1).

A Regional Intensive Observational Period in February 2009 (RIOP-09) was conducted covering the Mindoro-Panay Strait complex, a particular focus of PhilEx. Directed by near real-time surface current from HFDR central processing station, an intensive hydrographic survey of the cyclonic eddy observed over Panay Strait was carried out. A 24-hour (Feb 8, 06:07:21 – Feb 9, 07:10:44, 2009) successive cross-shore sections using the MacArtney TRIAXUS towed undulating vehicle equipped with Sea-Bird temperature and conductivity sensors along with hull-mounted shipboard Ocean Surveyor 150 kHz ADCP were obtained. A total of six transects were occupied, each spans 77 km across the strait. Daily atmospheric COAMPS forecasts, described by [May et al., 2011] and satellite images of sea surface temperature, ocean color, and wind speed provided as real time support to the shipboard team were also used for analyses.

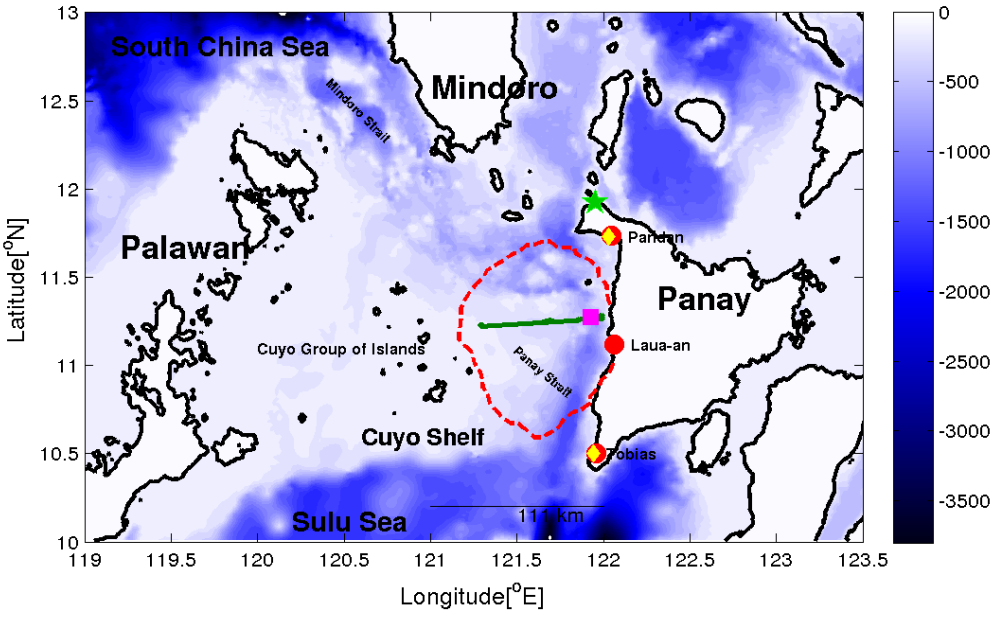

FIGURE 2.1: Bathymetry of study area and the limits of 75% HFDR data coverage indicated by red thick broken line. Locations of observations are marked: HFDR by red circles, SPG by yellow diamonds, ADCP by magenta square, TRIAXUS survey transects by green lines, and the nearby Caticlan airport by green star.

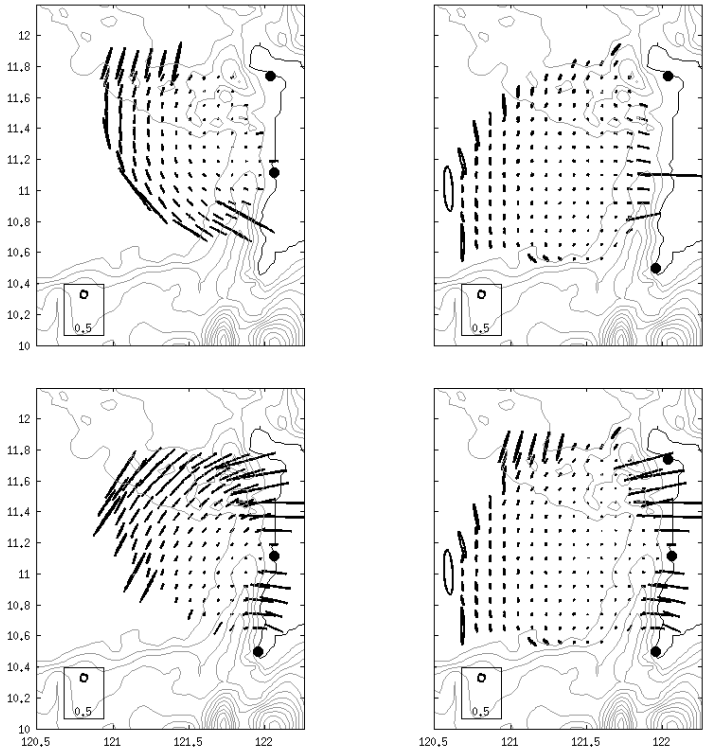

FIGURE 2.2: Geometric dilution of precision (GDOP) ellipses for various geometric configurations: (top left) between Pandan and Laua-an, (top right) Pandan and Tobias Fornier, (bottom left) Laua-an and Tobias Fornier, (bottom right) Pandan, Laua-an and Tobias Fornier. The legend corresponds to the threshold value to discard vector current data that are poorly constrained.

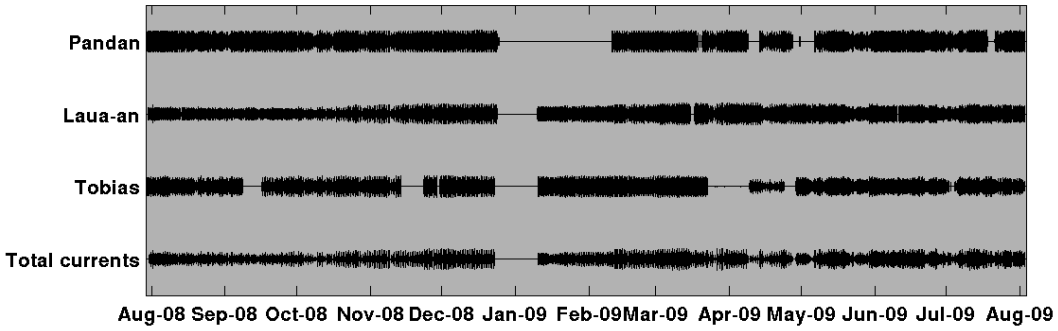

FIGURE 2.3: Temporal coverage of the three HF radar sites and of the combined vector currents. The thickness corresponds to the percentage of grid points with data. The percentage of data obtained during the operation is 70.3% for Pandan, 72% for Laua-an, 70.6% for Tobias and 79.4% for the vector currents.

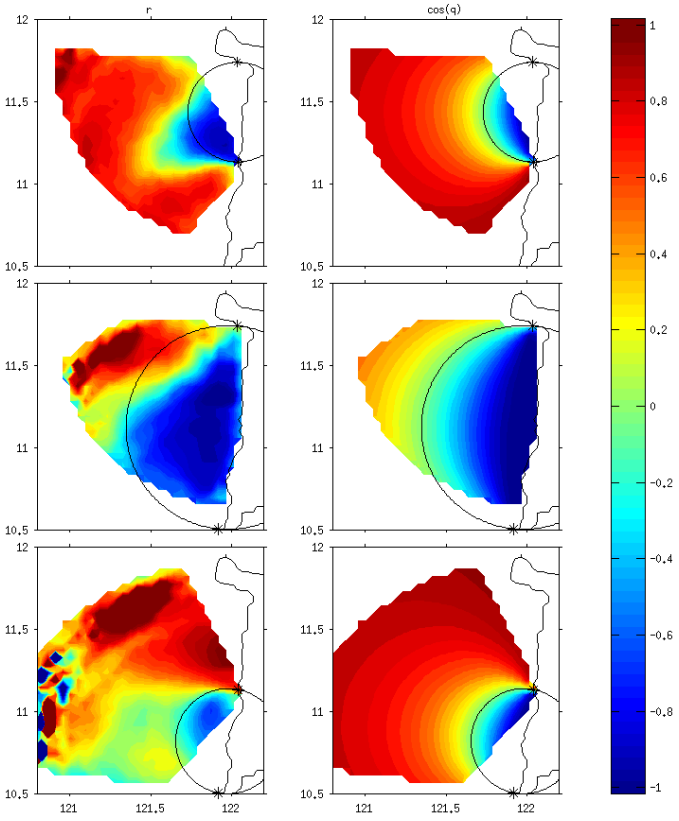

FIGURE 2.4: Cross-correlation between radial currents from pairs of sites (left column), and cosine of the angle between the sites (right column) for Pandan and Laua-an (top row), Pandan and Tobias (middle row) and Lauan-an and Tobias (bottom row). The circle where the angle between the two sites is 90° is overlaid for reference.

Chapter 3

Low Frequency Surface Currents in Panay Strait, Philippines

3.1 Introduction

The mechanisms for the generation of eddies in the wake of islands are due to Ekman pumping induced by wind stress curl [Chavanne et al., 2002; Jiménez et al., 2008], and by instability of lateral shear as oceanic flow passes the island [Dong et al., 2009]. The wind interaction with the island generates positive (negative) wind stress curls on the right (left) side of the island while looking downstream, causing upward (downward) Ekman pumping. As oceanic flow passes an island, horizontal shear and inhomogeneity in bottom stress induces vorticity. Thus, the lee sides of islands (headlands) tend to be areas rich in eddy activity depending on the direction of the prevailing winds and/or oceanic currents [Lumpkin, 1998; Barton et al., 2000; Chavanne et al., 2002; Calil et al., 2008; Pullen et al., 2008; Dong et al., 2009]. The mixture of these two processes on lee eddy generation takes place with almost all islands, and the relative importance of these two forcing mechanisms has been assessed using numerical models and observations.

Wind forcing was identified as the trigger mechanism in the generation of Gran Canaria eddies, but the main mechanism responsible for the eddy shedding was the topographic perturbation of the oceanic flow by the island flanks [Jiménez et al., 2008]. An observational study by Piedeleu et al. [2009] supported this conclusion using data from a mooring

leeward of Gran Canaria Island. In the Hawaiian archipelago, a sensitivity study of the generation of mesoscale eddies using a numerical model suggested that the wind, current and topography have a cumulative effect on the generation of eddies and the complex oceanic circulation pattern [Kersalé et al., 2011; Jia et al., 2011]. The importance of the wind forcing in generating these oceanic eddies has been highlighted [Calil et al., 2008; Yoshida et al., 2010; Jia et al., 2011; Kersalé et al., 2011; Couvelard et al., 2012; Caldeira et al., 2014]. In the Hawaiian archipelago, though the interaction of the North Equatorial Current (NEC) with the major islands is enough to generate eddies, wind observations in high spatial and temporal resolution play an important role in oceanic circulation. Details of the wind shear in the lee of the islands are necessary to correctly calculate the intensities of the vorticities [Calil et al., 2008; Jia et al., 2011; Kersalé et al., 2011]. For the Canary archipelago, the speed of the Canary Current is sufficient to create a flow at high enough Reynolds number to produce eddies, but their generation was suggested to be aided through Ekman pumping by the winds in the lee region of the islands [Sangrà et al., 2009].

Without significant background currents, wind forcing in the Gulf of Tehuantepec [Barton et al., 1993; Trasviña et al., 1995] and leeward of Madeira Island [Caldeira et al., 2014] generates energetic ocean eddies through Ekman pumping. This isolates ocean response to topographically-induced wind shear. The winds channeled through mountain gaps extend as a jet over the Pacific Ocean in the Gulf of Tehuantepec and in the lee of Madeira that spin-up ocean eddies. Wind generated eddies have also been identified in the Philippines in the wake of Mindoro and Luzon Islands in the absence of upstream oceanic currents [Pullen et al., 2008]. Using high-resolution air-sea modeling, monsoon surges during the winter season trigger oceanic eddy formation and propagation in the lee of the Philippines region of the South China Sea (SCS) [Pullen et al., 2008]. They are driven by the wind stress curl associated with the wind jets through the gaps of the island chain and wakes in the lee of the islands [Wang et al., 2008; Pullen et al., 2008]. These wind jets and associated leeside wakes are caused by the airflow over the mountainous terrain of the Philippine Archipelago. The strong winds blowing through gaps in mountain ranges or between islands occur in the presence of along-gap pressure gradients, that are a consequence of the partial blocking of cross-island monsoon flow by the mountains [Gaberšek and Durran, 2004, 2006]. Topographically constrained wind from high to low pressure was identified to be the dominant mechanism in valleys [Whiteman and Doran,

1993] and mountainous terrain [Weber and Kaufmann, 1998].

Additional eddy formation regions have been identified within and around the Philippine archipelago using a high-resolution configuration of the Regional Ocean Modeling System (ROMS) and observations during the Philippine Archipelago Experiment (PhilEx) [Han et al., 2009]. During the winter monsoon, aside from the cyclonic eddy in the lee of Mindoro [Wang et al., 2003; Pullen et al., 2008], cyclonic circulation was identified in the observed and simulated currents flowing northward west of Panay Island [Han et al., 2009]. In contrast during summer, no strong eddy flow pattern within this region has been observed. The Mindoro Strait eddy was found to be in geostrophic balance associated with the positive wind stress curl while the Panay Strait circulation could not be resolved by the model. These eddies were confirmed using the near-surface velocity from the shipboard ADCP during the PhilEx Regional Intensive Observational Period in January 2008 (RIOP-08) cruise [Gordon and Villanoy, 2011] to be a response to complex wind stress curl [Rypina et al., 2010; May et al., 2011; Pullen et al., 2011]. The eddy field seasonal variability however, was not resolved by these one-time hydrographic cruises and model results with known errors and limitations. In addition, the missing data in the upper 40 m from the moored ADCP over Panay Sill made the connection of the near-surface flow to monsoon variability more problematic [Sprintall et al., 2012].

This paper uses integrated in-situ and remote sensing analysis collected over a year (August 2008 - August 2009) to improve understanding of Panay Strait circulation and investigates its forcing mechanisms. The sampling campaign was part of the PhilEx.

The methods used to obtain low-frequency variability of the flow are presented in section 2. The low frequency observations are described in section 3. The forcing mechanisms of the cyclonic eddy are discussed in sections 4 and 5. The results are summarized and discussed in section 6.

3.2 Instruments and Data Processing

An intensive observation of Panay Strait was carried out to describe the mesoscale spatial structure and temporal variability of the surface current within the strait. Figure 3.1 shows the temporal coverage of the data which span over a year, covering the Asian

monsoon reversal. The Northeast (NE) monsoon is between December to March while Southwest (SW) monsoon is between June to October [Wang et al., 2001].

Tidal components of surface currents from HFDR and current profile from moored ADCP were separated out by performing a harmonic tidal analysis using T-Tide, an open source MATLAB toolbox as described by Pawlowicz et al. [2002]. It was then subtracted from the original data to obtain the residuals. The residuals were further subjected to a 6-day running median to reduce spectral leakage and to get the time series in which tides and near-inertial oscillations have been cautiously filtered out to isolate mesoscale processes. The Cartesian velocities were rotated into along-shore velocities based on the orientation of the coast of Panay Island ($9°N$). The similar 6-day running median was also applied to the daily wind data from Caticlan Airport and QuikSCAT satellite. Figure 3.2 shows the spatially averaged rotary spectra of the hourly and 6-day medianed surface current from HFDR where high frequency variability was removed.

3.3 Description of observations

3.3.1 Local wind variability

The monsoon is traditionally defined as a seasonally reversing wind system. The alternation of dry and wet seasons is in concert with the seasonal reversal of the monsoon circulation. The reversal is due to the differential heating of land and the oceans, the Coriolis force and moist processes that determine the strength and location of the major monsoon precipitation [Webster et al., 1998].

Panay Strait in the Philippines is situated within the strong influence of the Asian monsoon winds that blow from the northeast between December and March and from the southwest between June and October. The wind field exhibits pronounced seasonal variations between the NE and SW monsoon periods (Figure 3.3). Northeasterly winds are stronger and more stable than southwesterly winds, producing wind jets in between islands generating a distinctive spatial pattern of alternating bands of positive curl on the left flank and negative curl on the right of Luzon, Mindoro, Panay and Negros Islands. Consequently, positive curl on the north flank of Panay is enhanced, dominating the lee and presenting a favorable condition for the formation of mesoscale eddies during

NE monsoon. These features are not evident during the SW monsoon period, which is characterized by weaker, highly variable winds.

Wind vectors from the nearby airport correspond well with the QuikSCAT wind from the closest grid point. Correlation (R) of zonal (U) and meridional (V) wind components between the two datasets are 0.93 and 0.94 with root-mean-square differences (RMS diff) of 1.69 ms^{-1} and 4.09 ms^{-1}, respectively. An abrupt reversal of the wind regime is evident marked by a well-defined transition period followed by the short phases of weakening (Figure 3.4). Persistent northeasterly winds occur from October to mid-April and southwesterly winds prevail from May to September, with pronounced sub-seasonal breaks. These break periods are an important characteristic of the SW monsoon in Southeast Asia, and they have been associated with westward-propagating atmospheric equatorial waves [Tsing-Chang and Weng, 1996]. The strongest winds during the NE monsoon are in January. October and April-May mark the transition periods between the NE monsoon and the SW monsoon, respectively.

3.3.2 Surface ocean current patterns

Surface wind forcing is particularly evident in the circulation patterns in and around the Philippine Archipelago. In Panay Strait, which is subject to pronounced Asian monsoon reversal, observed surface flow patterns are highly seasonal with well-defined transition periods. Mean flow during the NE monsoon (November 2008 - March 2009) is characterized by a jet-like northward flow, referred to here as the PC jet, and a southwestward return flow forming a cyclonic circulation (Figure 3.5, top). In contrast, the SW monsoon period is characterized by a relatively weak northward PC jet, with significant weakening and modification over the shallow Cuyo shelf (Figure 3.5, bottom) (combined for August-September 2008 and June-July 2009).

Time series of the PC jet and cyclonic eddy over the three cross-shore transects in Figure 3.5 are shown in Figure 3.6. The PC jet is defined as the mean surface current from the coast to the center of the eddy where the mean flow is zero, while the cyclonic eddy is defined as the mean surface current from the center of the eddy to the west over which HFDR data are available. Mean flow time-series clearly exhibit the most dominant features, the steady PC jet and the seasonal cyclonic eddy. The three transects show

comparable strength of the dominant flows over Panay Strait and depict the size of the eddy occupying the whole HFDR domain.

The PC jet is generally northward as indicated by positive mean surface current. It persists from mid-May – September with noticeable weakening during early May and October, which coincides with the relaxation of the monsoon winds during transition periods. In contrast, the cyclonic eddy is highly seasonal. It forms during NE monsoon as indicated by southward (negative) mean surface current in mid-November and intensifies during the peak of NE monsoon (December - February) dominating over the HFDR domain. As the eddy strengthens in January along with progressing NE monsoon, it moves close to the coast resulting in a more southward mean flow and weaker PC jet. By March, a considerable westward shift of the cyclonic eddy leads to an intensified PC jet, which replaces the eastern limb of the eddy.

3.3.3 Evidence for a wind-induced cyclonic eddy formation mechanism

From the analysis of the wind (Figure 3.4) and surface current (Figure 3.6), the first signature of the cyclonic eddy west of Panay appears in mid-November, about a month and a half after the NE monsoon prevails over the area. It strengthens with progressing northeasterly wind then gradually shifts westward and is replaced by the enhanced northward PC jet. Figure 3.7 shows a shift in the location of the eddy as the wind veered to a more easterly orientation during the waning NE monsoon (mid-February to mid-April) from the observed airport wind and in the snapshots of QuikSCAT wind stress and wind stress curl (Figure 3.8). As the eddy shifts westward and widens, it reinforces the PC jet, which is now the dominant flow pattern over the HFDR domain.

During the NE monsoon, variations of the PC jet are mainly influenced by the eddy, evident in the current profile obtained from the moored ADCP (Figure 3.9). Contoured along-shore current profile overlaid with along-shore surface current from the closest HFDR data (thick black line) show a generally northward PC jet with pronounced intensification during the NE monsoon when the cyclonic eddy is generated. A southward flow in January was also captured by ADCP when the cyclonic eddy moves close to the coast as northeasterly winds intensify.

The seasonal evolution of the cyclonic eddy appears to be an oceanic response to the prevailing local wind. Figure 3.10 shows the mean 10 m wind and wind stress curl from COAMPS forecasts supplied to researchers on the PhilEx RIOP-09 cruises in real time, averaged over a 40-day period from mid-February through end of March 2009. The acceleration of the winds on the edges of the islands of Mindoro, Panay, and Negros and the weakening in its lee are well resolved. The surface wind derived from Envisat Synthetic Aperture Radar (SAR) image [see Thompson and Beal, 2000, on how to extract wind speed estimates from SAR] verifies the presence of wind jets and wakes (Figure 3.11). Although the image is a snapshot (0141 UTC 7 March 2009), it was taken during the NE monsoon wind regime and agrees well with the general patterns that are apparent in the mean model winds shown in Figure 3.10. As in the model, the strongest winds, nearly 10 ms^{-1}, are in between Mindoro and Panay through Tablas Strait. Figure 3.10 (right) shows the resulting wind stress curl dipoles reaching the magnitude of 10 $^{-6}Nm^{-3}$ associated with each island. However, due to the orientation of Panay Island with respect to the NE monsoon wind, positive wind stress curl dominates in the lee, drastically affecting the ocean circulation.

Curl of the wind stress causes Ekman flux divergence and convergence which in turn drives Ekman pumping. To conserve mass, a vertical velocity (w) results, which is [Gill, 1982]

$$w_E = w(-H_E) = curl_z \frac{\tau}{\rho f} \tag{3.1}$$

where w_E is the Ekman pumping velocity, τ is the surface wind stress, ρ is the density of seawater (1025 kgm^{-3}), and f is the Coriolis parameter. A vertical velocity (w) at the base of the Ekman depth ($-H_E$) estimates the upwelling or downwelling proportional to the wind stress curl.

Figure 3.12 shows that the largest curl-driven Ekman pumping velocity over the Cuyo shelf is in the lee of Panay Island, indicating an upwelling zone. Although the calculation using satellite wind is weaker than the modeled wind, both exhibit the same general pattern. The value of Ekman pumping velocity reaches up to 15 $m.day^{-1}$ based on the snapshots of wind stress curl calculated from COAMPS wind. The instantaneous Ekman pumping velocities indicate a wind-induced divergent Ekman transport which agrees with

the mean divergence calculated from HFDR in the lee of the island during the same time period (Figure 3.13). As a result of surface divergence, the thermocline is lifted and the water column beneath is stretched, forming the Panay Dome. Figure 3.14 shows the mean profile of (top) temperature and (middle) density from the hydrographic cross-shore sections. The doming of isotherms and isopycnals corresponds well with the return flow in the near-surface along-shore current from the shipboard ADCP, indicating the center of the eddy. The excursion of the isolines reaches around 50 m. In the current profile (Figure 3.14, bottom), the along-shore return flow reaches a depth of about 130 m, indicating the depth of the eddy. Velocities at the surface reached mean values of 50 cms^{-1}. The flow structure is nearly depth-independent over the shallow shelf, whereas a strong southward flow below 150 m is evident at the deep channel in the strait. Sprintall et al. [2012] observed similar southward flows as extraordinarily strong pulses that begin at intermediate depth in the Fall transition and shoal toward the sub-thermocline during the NE monsoon found both in Mindoro and Panay Straits ADCP moorings. These southward flows are strongly correlated with the changes in the South China Sea large-scale circulation and remote wind forcing off Vietnam [Sprintall et al., 2012] .

The uplift in the thermocline sets up a horizontal pressure gradient, which consequently spins up the geostrophic cyclonic eddy. The eddy formation is evident in the mean vorticity overlaid by the surface current from HFDR, in which the center coincides with the location of largest Ekman pumping and the doming (Figure 3.15).

If the divergence is entirely wind-driven and confined within the Ekman depth, divergence should be proportional to the Ekman pumping velocity at the base of the Ekman layer. That is

$$\delta = \nabla_h . \bar{u}_h = \frac{w_E}{H_E} \tag{3.2}$$

where $\delta = \nabla_h . \bar{u}_h$ is the divergence, subscripts h, denote horizontal components, and w_E, is the Ekman pumping velocity at constant Ekman depth, H_E=32 m determined as the best fit between the integrals of Ekman pumping velocity and divergence calculated by Equation **??** and Equation **??**, respectively.

Figure 3.16 shows the correlation between (top) divergence and Ekman pumping velocity and between (bottom) vorticity and Ekman pumping velocity averaged over a specified

region (box in Figure 3.13 and Figure 3.15). All of the terms have been normalized by f in order to facilitate comparison. The divergence and vorticity are significantly linked together to Ekman pumping velocity, with correlation coefficient of R=0.50 and R=0.67 and RMS differences of 0.03 and 0.18, respectively.

3.3.4 Dynamical analysis of the cyclonic eddy

Vorticity input to the ocean from the overlying wind stress curl appears responsible for the cyclonic eddy generation and evolution during the NE monsoon. By estimating the surface vorticity balance of the low frequency surface current, wind contribution to the generation and evolution of the vortex was assessed by

$$\frac{D\zeta}{Dt} = -(f+\zeta)\delta - \nu\beta + R \tag{3.3}$$

where $\frac{D\zeta}{Dt} = \frac{\partial\zeta}{\partial t} + u\cdot\nabla\zeta$ is the rate of change of vorticity following the fluid motion, $(f+\zeta)\delta$ is the vortex stretching, $\nu\beta$ is the Beta-effect term, where ν is the meridional velocity and β is the meridional spatial derivative of f, and R is the residual term, assumed to be due to friction and unresolved noises. Vorticity changes associated with sloping topography was neglected.

Assuming that the momentum flux from the surface is due to wind stress, its contribution to R is:

$$R_w = \frac{1}{\rho H_E} curl_z \tau \tag{3.4}$$

where $\rho = 1025 kgm^{-3}$ is the density of seawater, H_E is the Ekman depth, and $curl_z\tau$ is the wind stress curl computed from QuikSCAT gridded daily wind.

Figure 3.17 (top) shows the temporal variation of each term in the vorticity balance equation averaged over the same box in Figure 3.13 and Figure 3.15. Note that the β term is magnified by a factor of 10 to show the trend. The evolution of the vorticity within the vortex core was generally dominated by frictional processes, R, which drives the formation of cyclonic vorticity from mid-November until mid-April. Observe, however

a significant R lag of about 10 days during NE monsoon, specifically during strengthening of the cyclonic eddy during Dec.08, Feb.09 and Apr.09. R_w from QuikSCAT compares well with the R from the HFDR observations, suggesting that the frictional forcing R is induced dominantly by the wind stress curl driving the cyclonic vorticity growth after a time lag of about 10 days (Figure 3.17, bottom).

Another interesting finding involves the β term. Recall the westward considerable shift in the center of the eddy (Figure 3.7) during the waning NE monsoon. Figure 3.17 shows that the shift coincides with an increasing β, though an order of magnitude less than the other terms. We speculate that the β term causes the cyclonic eddy to propagate westward in the manner of a Rossby wave.

Figure 3.18 and Figure 3.19 show the spatial distribution on 6 different days of each term of the vorticity balance taken within the RIOP-09 period. If the Lagrangian rate of change of vorticity is caused by frictional forcing, their spatial distribution should be comparable. But since there is a considerable time lag between the two terms (Figure 3.17), disparity on their spatial variability notably exist.

3.3.4.1 Time lag between the wind forcing and the ocean response

To clarify the relationship between the cyclonic eddy formation processes and the wind stress curl forcing (correlation shown in Figure 3.16), temporal variability of divergence, δ, and relative vorticity, ζ, were plotted against the Ekman pumping velocity, $\frac{w_E}{H_E}$, proportional to wind stress curl (Figure 3.20). Since a higher correlation exists between divergence and the Ekman pumping velocity (Figure 3.16, top), Figure 3.20 (top) specifically shows that it occurs during strong and persistent NE monsoon winds although peaks and dips occur due to the shifts of the eddy. In contrast, vorticity increases quickly with progressing NE monsoon winds resulting in a relatively higher RMS=0.18 compared to divergence with RMS=0.03. The Ekman pumping velocity is positive during October when the NE monsoon prevail however, the response of the ocean to changes in the wind stress curl is not instantaneous. The cyclonic vortex first appears as a closed circulation in the low frequency current field only in mid-November indicated by positive vorticity ($0.05f$) and attained its maximum in February 2009 ($0.61f$).

To further examine the time lag response of cyclonic eddy generation, the temporal variation of thermocline depth anomaly is compared with the time integrals of the Ekman pumping velocity and divergence. The best fit between the two terms was found at Ekman depth, H_E=32m and used as constant for all calculations.

The time integrals of the Ekman pumping velocity and divergence from a reference time (July 28, 2008) represent their cumulative effect on the vorticity evolution, provided that internal and external drags are neglected. Thermocline depth anomaly on the other hand is proportional to vorticity, assuming a geostrophic balance in a 1.5 layer reduced gravity model,

$$\begin{aligned} fu &= -g\prime\frac{\partial h}{\partial y} \\ -fv &= -g\prime\frac{\partial h}{\partial x} \end{aligned} \tag{3.5}$$

where x and y are the conventional Cartesian coordinates, u and v the horizontal components of velocity, f the Coriolis parameter, $g\prime = g\frac{\nabla\rho}{\rho_b}$ the reduced gravity (g is gravity = 9.8 ms^{-2}, ρ_b is the density at the motionless bottom layer, and $\nabla\rho$ is the density difference between the active top and motionless bottom layer, and $h(x, y)$ the thermocline depth anomaly.

Equations 3.7 were differentiated to obtain the relative vorticity and after some arranging, yields:

$$f(\frac{\partial v}{\partial x} - \frac{\partial u}{\partial y}) = -g\prime\nabla^2 h \tag{3.6}$$

$$\zeta = \frac{-g\prime\nabla^2 h}{f} \tag{3.7}$$

The cyclonic eddy is assumed to be radially symmetric with sea surface height (h) perturbation at radial distance, r from the center of the eddy that has a Gaussian structure of the form:

$$h(r) = h_0 \exp(-\frac{r^2}{L^2}) \tag{3.8}$$

where h_0 is the amplitude of the eddy, and L is the radius of the eddy. This height function was substituted into Equation 3.5 to give:

$$h = \frac{\zeta f L^2}{g\prime} \tag{3.9}$$

L and $g\prime$ were estimated from the mean hydrographic cross-shore section while corresponding vorticity, ζ was calculated from HFDR.

Figure 3.21 shows that the Ekman divergence is an instantaneous response to the positive wind stress curl forcing. When NE monsoon prevails, after a quick transition period in October (Figure 3.4), the integrated wind stress curl becomes positive. Consequently, divergence occurs and increases rapidly along with the wind stress curl from mid-October 14, 2008 until mid-April 2009. After the transition period in April 2009, the wind stress curl becomes very weak with no further increase in the time integral. In contrast, convergence occurs during the SW monsoon period as the region is now dominated by the northward PC jet resulting in relatively higher sea level and warmer temperature evident from the bottom pressure gauges measurements deployed during the same monsoon regime in Pandan (Figure 3.22).

Correspondingly, a time lag response in the vorticity field occurs a month after mid-November 2009 Figure 3.21) when it increases quickly, producing a mature and closed cyclonic eddy circulation shown in Figure 3.6 (bottom). The current vorticity reaches its maximum in January 2009, though HFDR data is missing but can be inferred from the increasing values of vorticity and the strength of wind reaching its maximum during this time of the year (Figure 3.4). After that initial period, ocean vorticity responds effectively to fluctuating local wind magnitude and direction where peaks and dips correspond with the strong and weak NE monsoon wind, respectively. A considerable decrease of vorticity value in March 2009 indicate the westward shift of the center of the eddy in March 2009, though the cumulative wind stress curl and divergence are still proportionally increasing. This further support β term causing the cyclonic eddy to propagate westward.

3.4 Summary and Conclusion

High-resolution observations both in time and space of surface currents resolved the details of the low-frequency mesoscale flow in Panay Strait. The surface circulation in the strait has a distinctly seasonal cycle with the generation of a cyclonic eddy during the NE monsoon, reinforcing the steady PC jet as its eastern limb.

The cyclonic eddy formation is the dynamic response to fluctuations in the monsoon winds, specifically the variations of the wind jets blowing in between the islands of Mindoro and Panay, generating the positive wind stress curl in the lee of Panay during the NE monsoon. Based on observations and satellite-derived winds, wind curl field variations due to the changes in the strength and direction of the prevailing local wind play an important role in the generation and evolution of the eddy, and variability of the PC jet.

The region of positive wind stress curl causes Ekman flux divergence in the upper layer which in turn drives Ekman pumping lifting the thermocline and stretching the water column beneath, forming the Panay Dome. This results in horizontal pressure gradients, which consequently generates a cyclonic eddy in geostrophic balance. The Panay Dome is a subsurface upwelling, but to the west over the shallow Cuyo shelf, notable spreading of isotherms and isopycnals indicate a vertically mixed water column, which destroys the water column stratification. This therefore brings cooler, denser and nutrient-rich waters into the euphotic zone leading to enhanced biological productivity over the region. Satellite images confirmed cooler SST and enhanced chlorophyll concentration over the Cuyo shelf, indicative of an active upwelling zone.

Evaluating all the terms of the surface vorticity balance equation suggests that the wind stress curl via Ekman pumping mechanism provides the necessary input in the formation and evolution of the cyclonic eddy. The Beta-effect on the other hand may led to propagation of the eddy westward.

In particular, the cumulative (time-integrated) effect of the wind stress curl plays a key role on the generation of the cyclonic eddy, showing its robust mechanism to eddy kinetic energy. Further, this study shows that unlike divergence, vorticity response to prevailing

wind stress curl is not instantaneous causing a time-lag, which may help towards understanding the physical development of coastal upwelling due to Ekman pumping in the lee of the island.

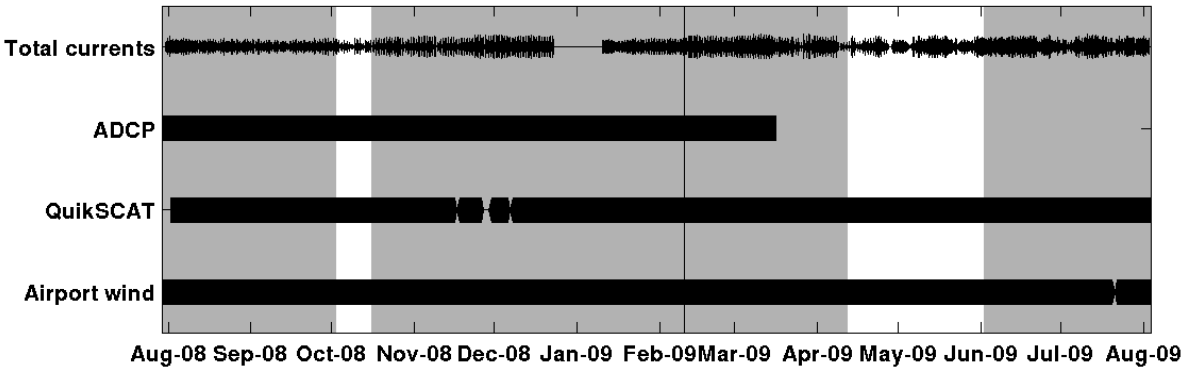

FIGURE 3.1: Temporal coverage of the HFDR combined vector currents, ADCP current profile, QuikSCAT, and Caticlan Airport winds. The thickness corresponds to the percentage of grid points with data. The percentage of data 79.4% for the vector currents, 100% for current profile, 98.7% for QuikSCAT and 99.8% for the airport wind. The thick solid line marked the RIOP-09 cruise in February 2009.

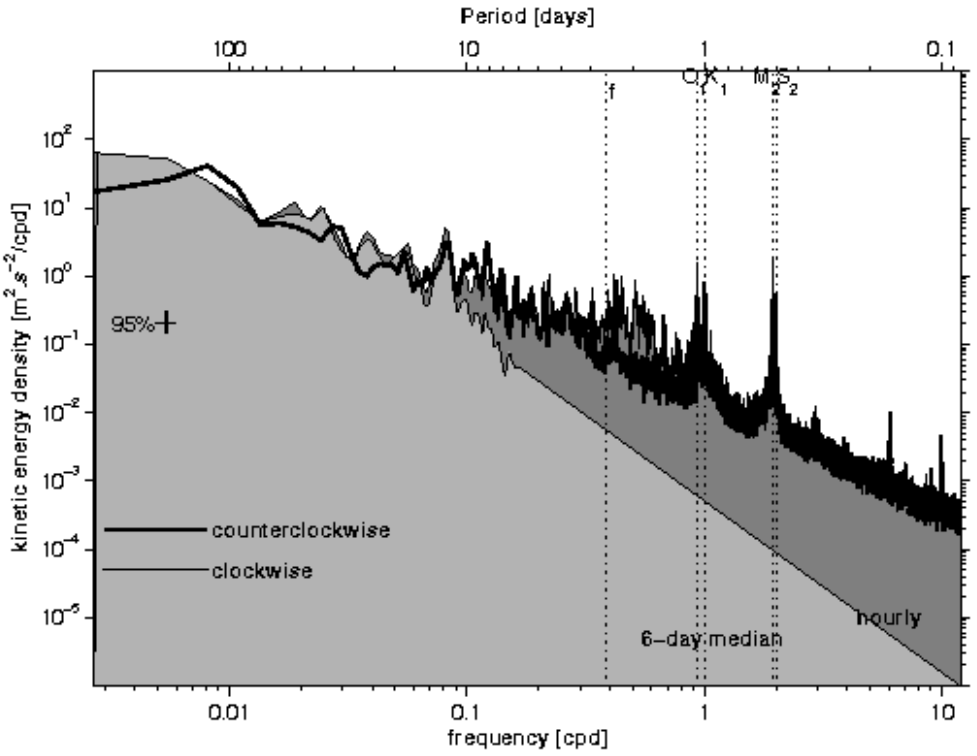

FIGURE 3.2: Rotary power spectra of hourly (dark gray) and 6-day medianed (light gray) HFDR data averaged over an area with more than 75% temporal coverage. Major tidal constituents (O_1, K_1, M_2 and S_1) and inertial frequency (f) are indicated on the top x-axis.

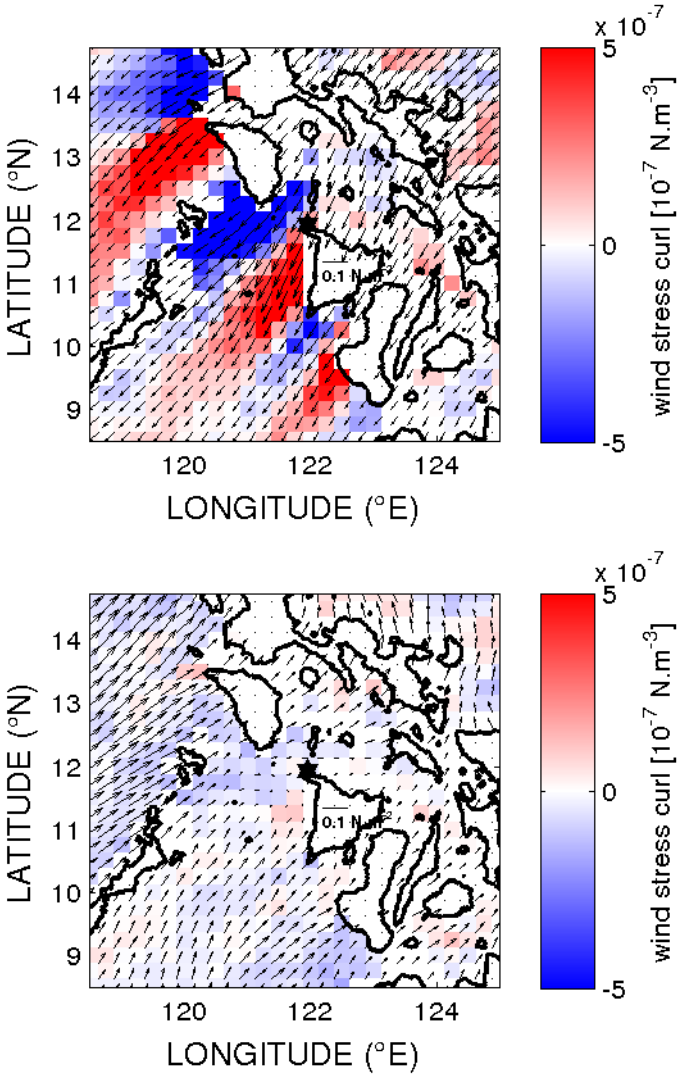

FIGURE 3.3: Wind stress and curl from QuikSCAT at 25-*km* resolution, averaged over HFDR period during (top) NE monsoon (November-March) and (bottom) SW monsoon (May-September). Marked with star is the Caticlan airport where observed wind data was obtained and correlated with the nearest QuikSCAT wind data shown in Figure 3.4.

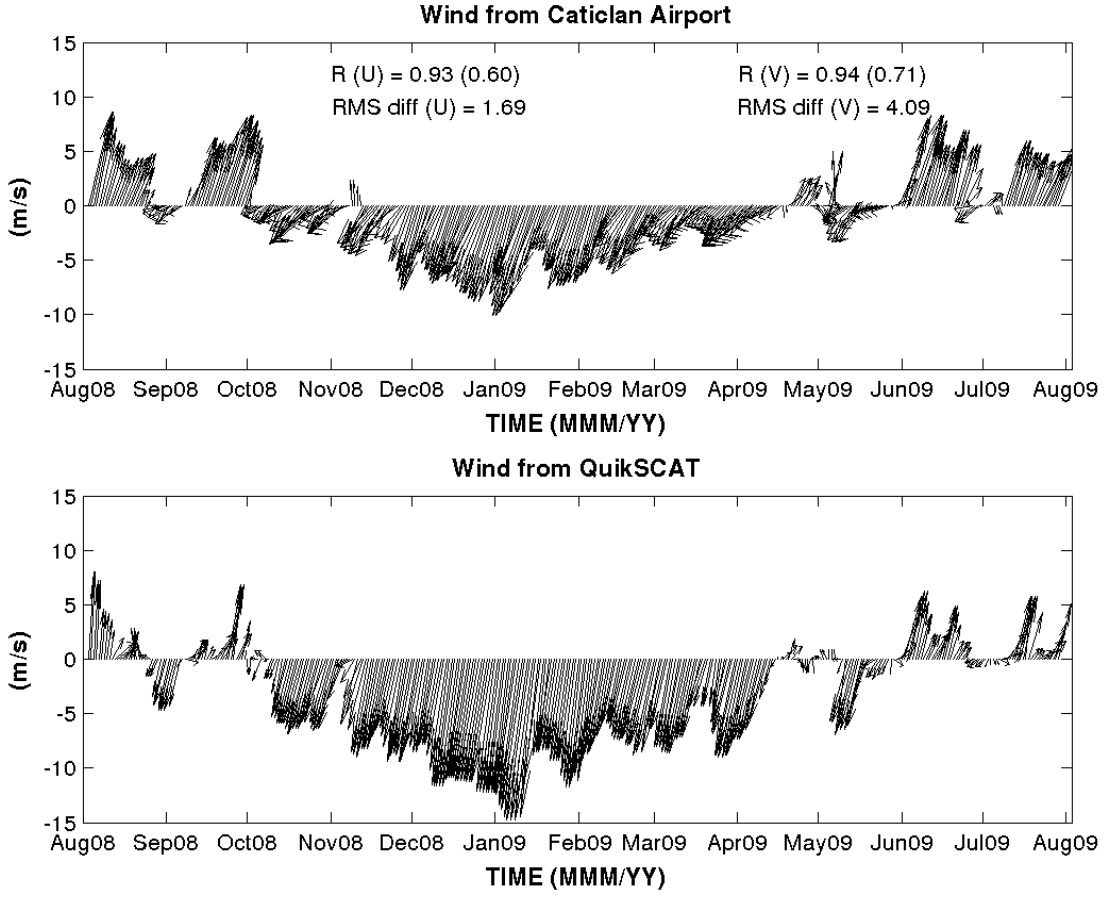

FIGURE 3.4: Time-series wind vectors from nearby Caticlan airport and QuikSCAT from the closest grid point. Correlations (R, the numbers in parentheses indicate the 5 % statistical significant level) and root-mean-square differences (RMS diff) are indicated in the top plot for zonal (U) and meridional (V) components.

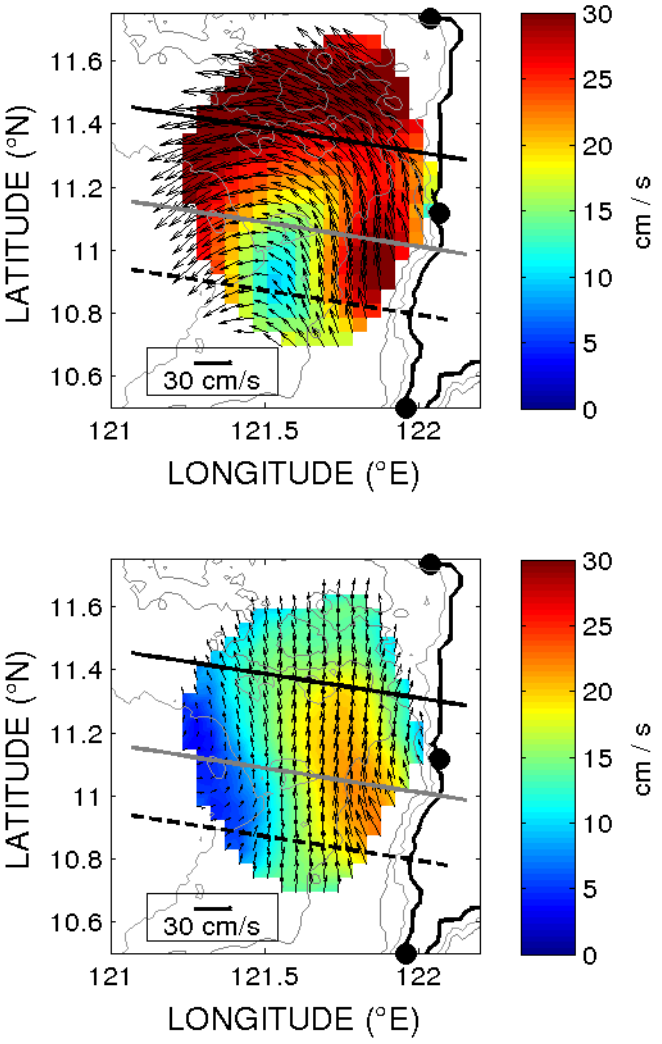

FIGURE 3.5: Mean flow overlaid with speed contoured in cms^{-1} during (top) NE monsoon and (bottom) SW monsoon. Three transects are marked accordingly along which mean surface flow profiles are shown in Figure 3.6.

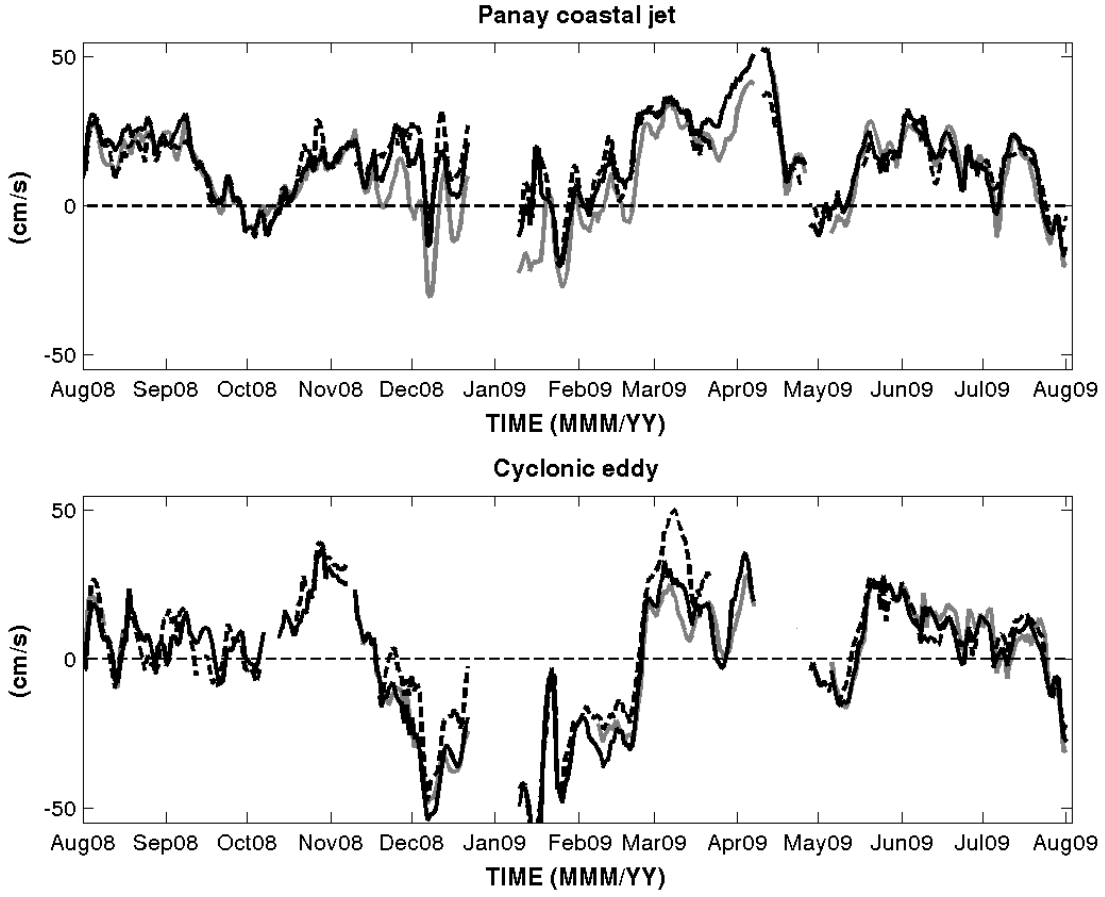

FIGURE 3.6: Time series profiles of (top) PC jet and (bottom) cyclonic eddy. Positive (negative) values indicate flow towards the north (south). The line color and type corresponds to three transects in Figure 3.5.

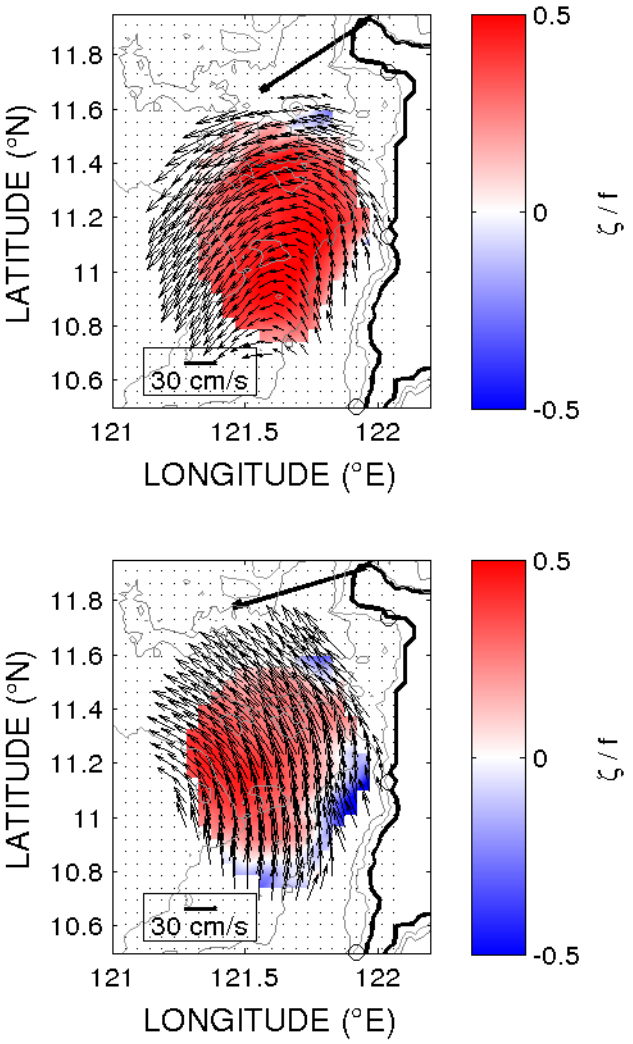

FIGURE 3.7: Mean surface flow overlaying vorticity, ζ, normalized by f contours during peak (top, January 15–February 23, 2009) and waning (bottom, February 25-April 1, 2009) NE monsoon. The arrows indicate the mean prevailing wind vectors from the Caticlan airport.

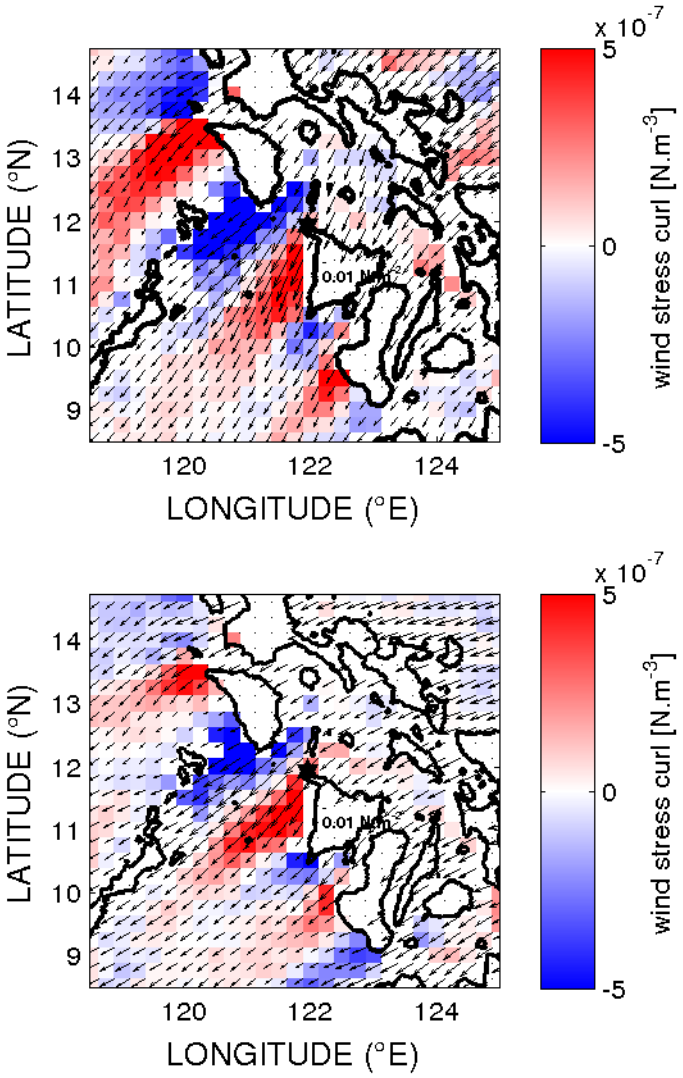

FIGURE 3.8: Wind stress vectors overlaying the wind stress curl contours during peak (top, January 15–February 23, 2009) and waning (bottom, February 25-April 1, 2009) NE monsoon from QuikSCAT.

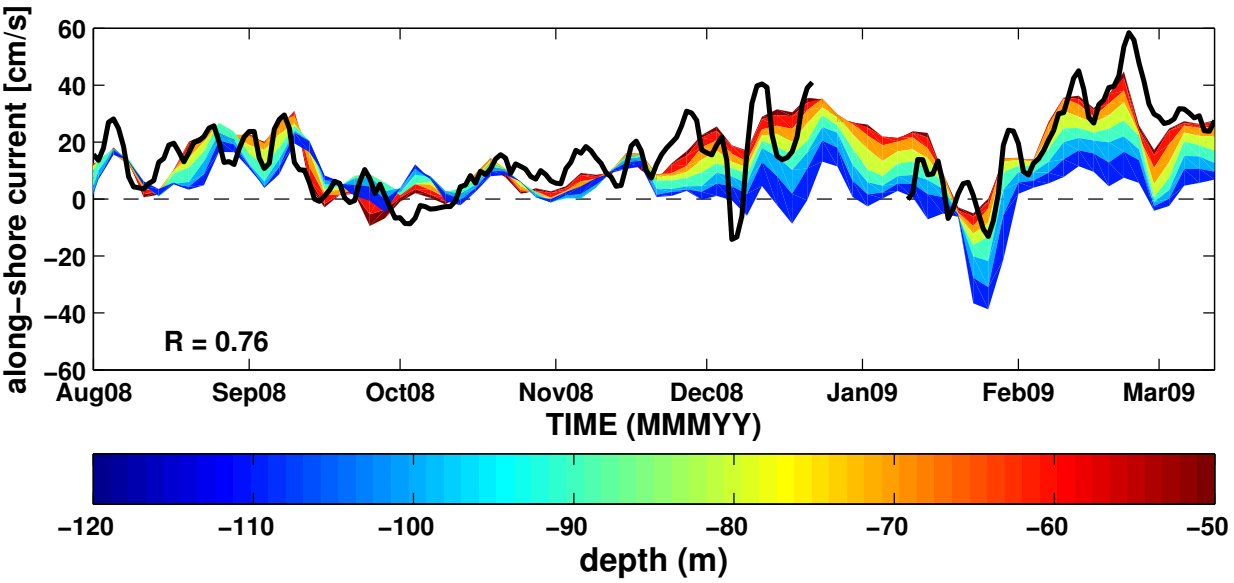

FIGURE 3.9: Time series along-shore current from moored ADCP (contoured) overlaid with along-shore surface current from the closest HFDR data (thick black line). Correlation (R) between HFDR and 50 m depth bin ADCP along-shore currents is indicated.

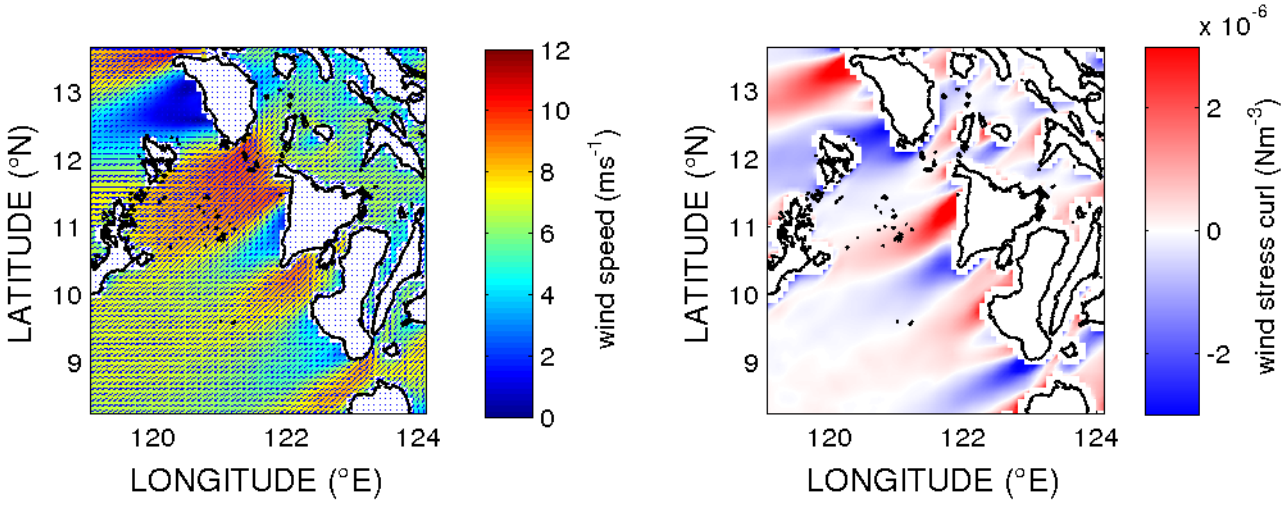

FIGURE 3.10: The Coupled Ocean/Atmosphere Mesoscale Prediction System (COAMPS) left) 10 m mean wind, wind vectors plotted over wind speed contour (ms^{-1} and right) mean wind stress curl contour (Nm^{-3}) from the 9 km computational grids for the Regional Intensive Observational Period, February to March 2009 (RIOP-09).

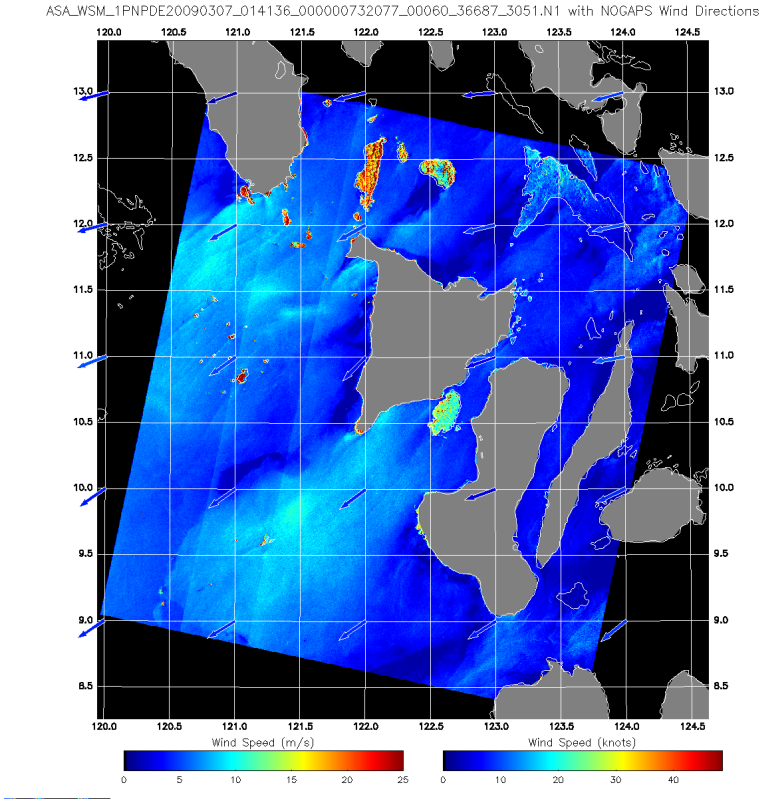

FIGURE 3.11: Surface wind speeds derived from an Envisat Synthetic Aperture Radar (SAR) image with wind vectors from the Navy Operational Global Analysis and Prediction System (NOGAPS) model for 0141 UTC 7 Mar 2009.

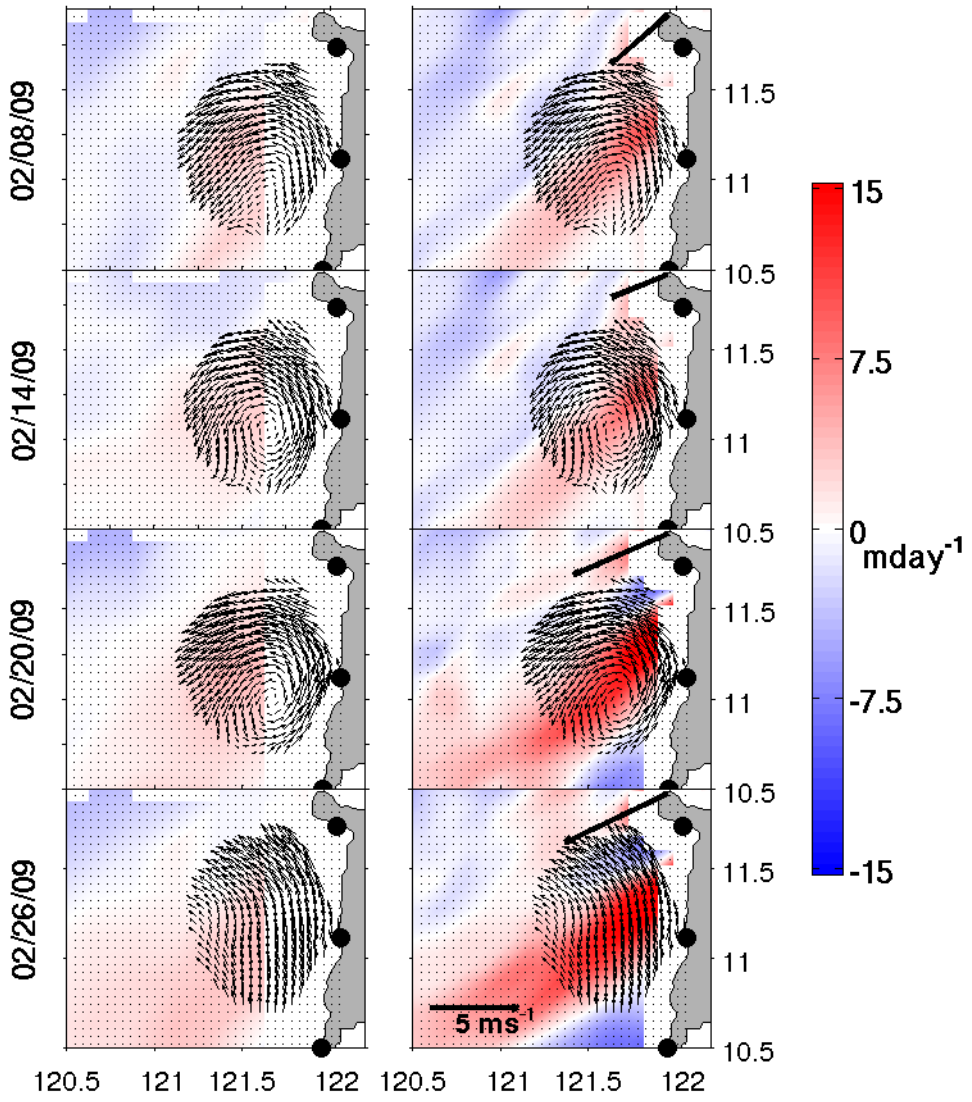

FIGURE 3.12: Snapshots of surface current overlaid with contoured Ekman pumping velocity calculated from (left) QuikSCAT and (right) COAMPS wind. Wind vectors at Caticlan airport (thick arrows) are also indicated.

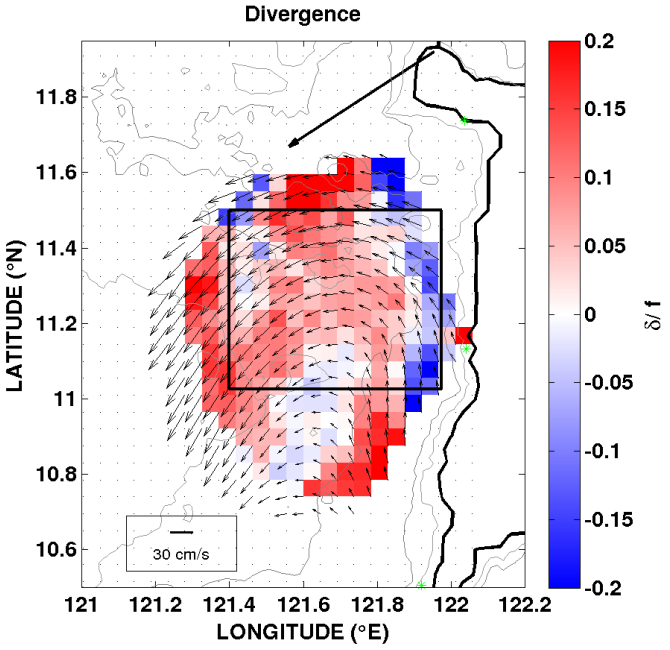

FIGURE 3.13: Mean surface current overlaid with contoured mean divergence for February to March 2009 (RIOP-09).

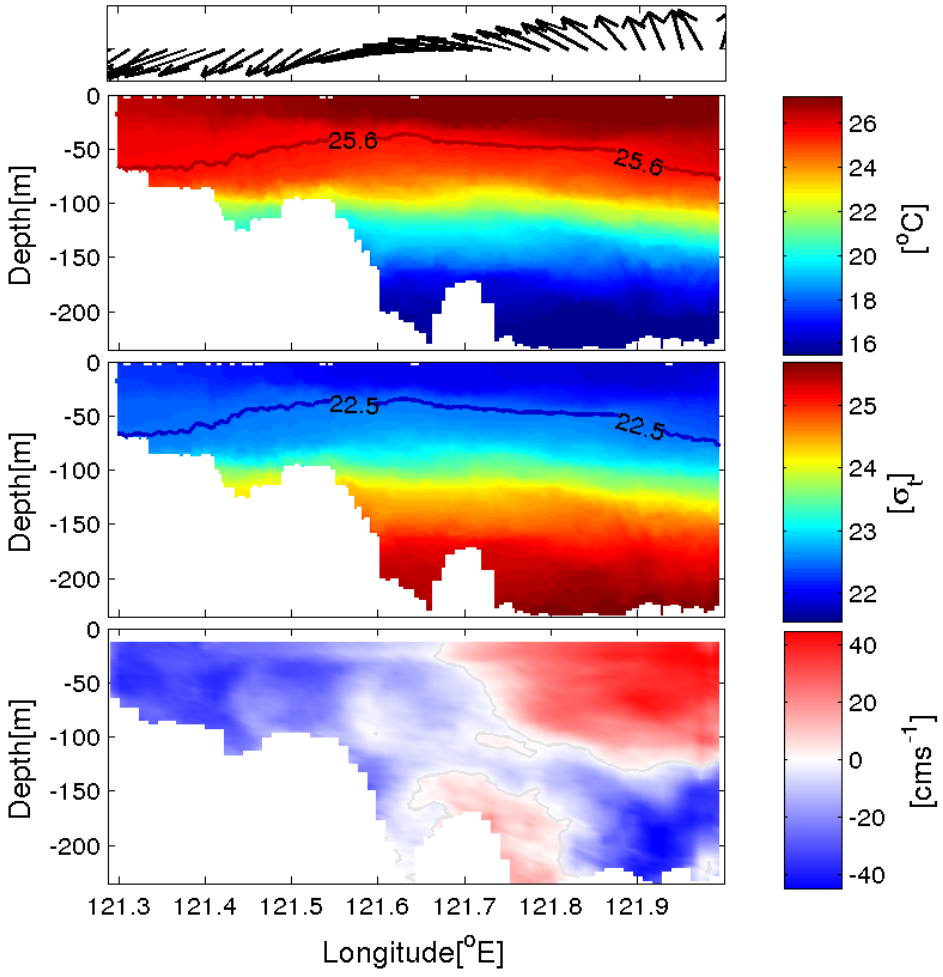

FIGURE 3.14: Vertical transect of mean (top) temperature, (middle) density, and (bottom) along-shore flow from the shipboard ADCP across the Panay Strait during the hydrographic survey (February 8-9, 2009) shown in Figure 2.1. The mean near-surface along-shore flow vectors are indicated above.

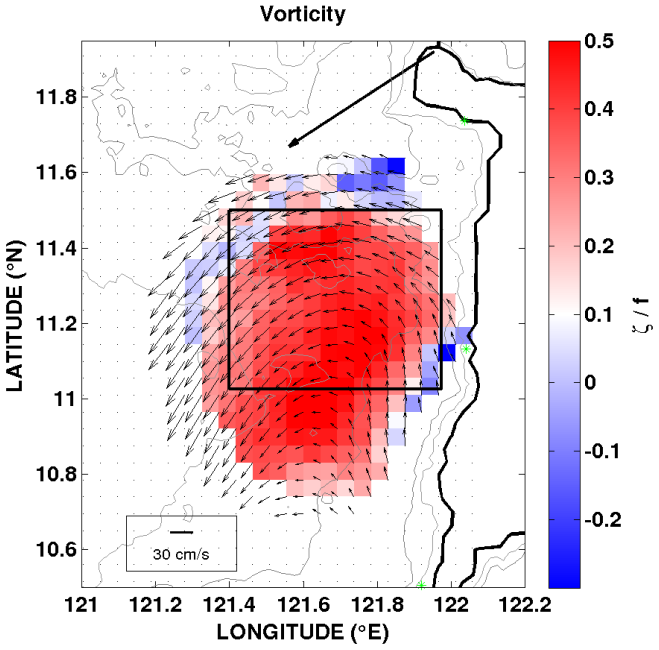

FIGURE 3.15: HFDR mean surface current overlaid with contoured mean vorticity for February to March 2009 (RIOP-09).

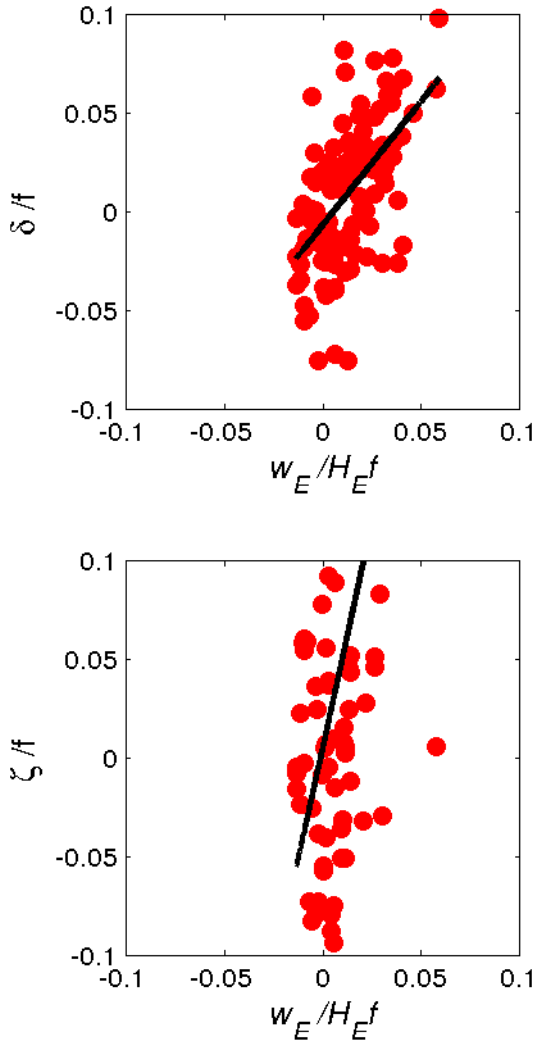

FIGURE 3.16: Scatterplots of mean (top) divergence vs. Ekman pumping velocity, and (bottom) vorticity vs. Ekman pumping velocity. Divergence and vorticity were calculated using HFDR data while Ekman pumping velocity was calculated using COAMPS from the region inside the box shown in Figure 3.13 and Figure 3.15 during February to March 2009 (RIOP-09).

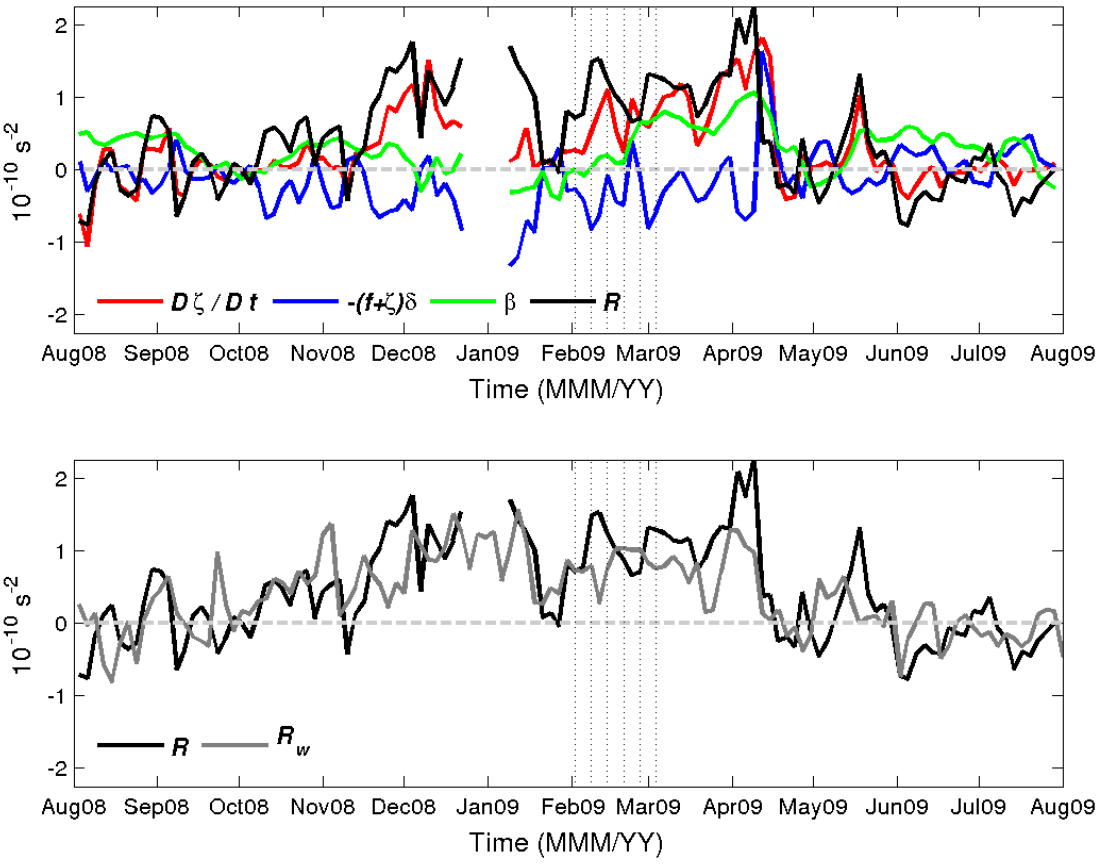

FIGURE 3.17: Time series of vorticity balance terms (Equation 3.3) averaged over the vortex core. The β term is vertically exaggerated. Vertical dotted lines indicate the snapshots in Figure 3.18 and Figure 3.19.

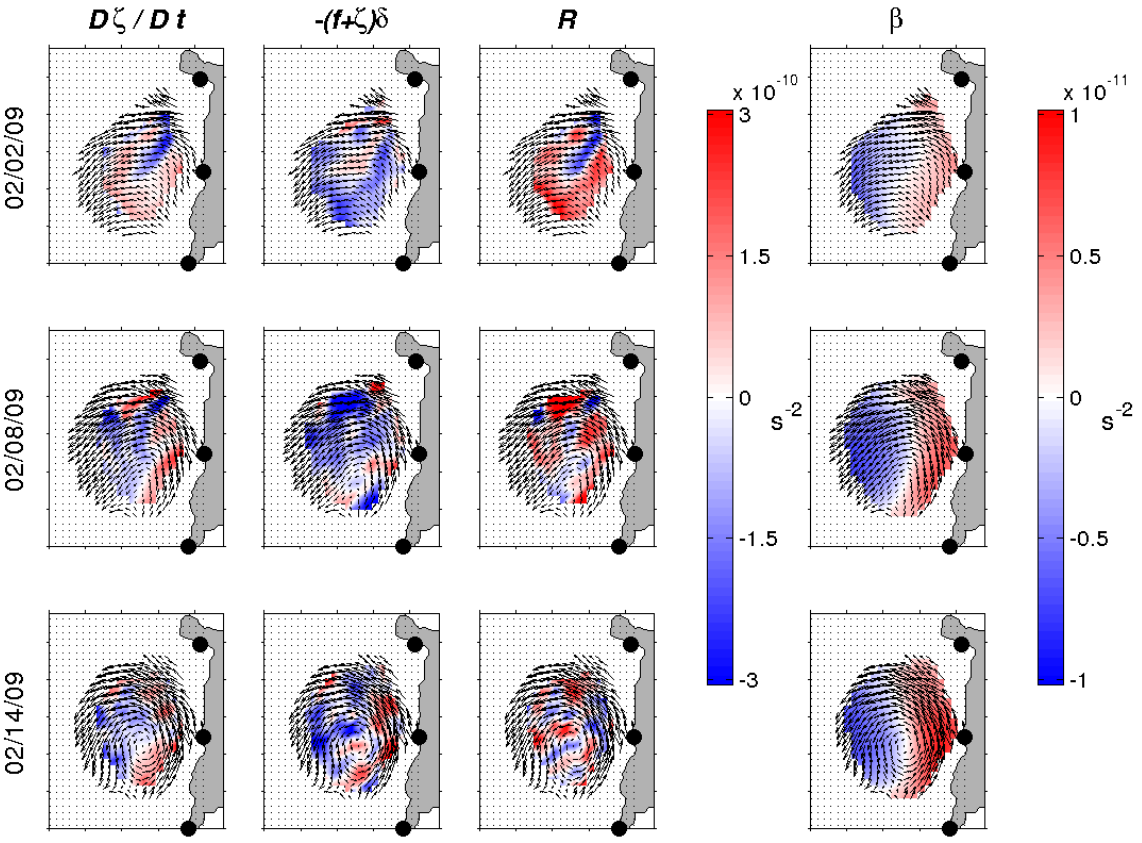

FIGURE 3.18: Snapshots of the terms of the surface vorticity balance (Equation 3.3), overlaid with surface currents. From left to right, Lagrangian rate of change of vorticity, vortex stretching, residual, and Beta-effect terms. The times of snapshots are indicated on the y-axis of the first column.

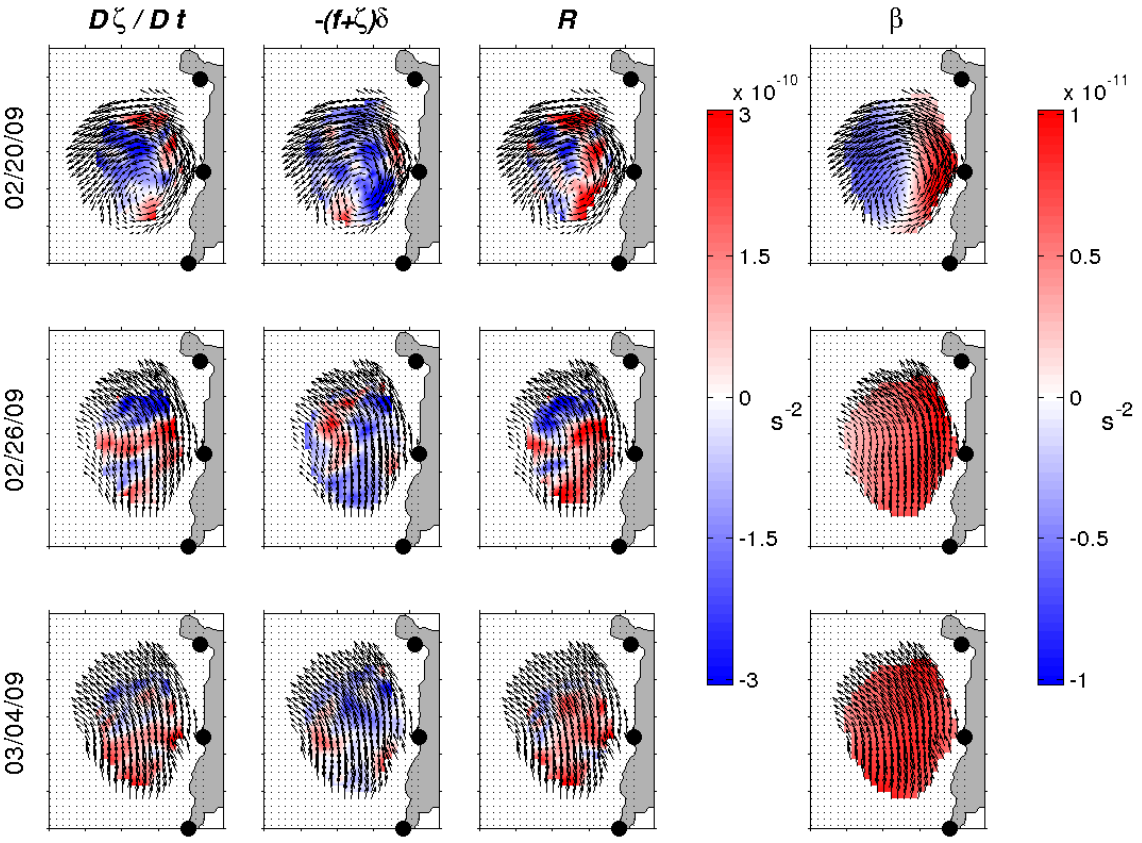

FIGURE 3.19: Snapshots of the terms of the surface vorticity balance (Equation 3.3), overlaid with surface currents. From left to right, Lagrangian rate of change of vorticity, vortex stretching, residual, and Beta-effect terms. The times of snapshots are indicated on the y-axis of the first column.

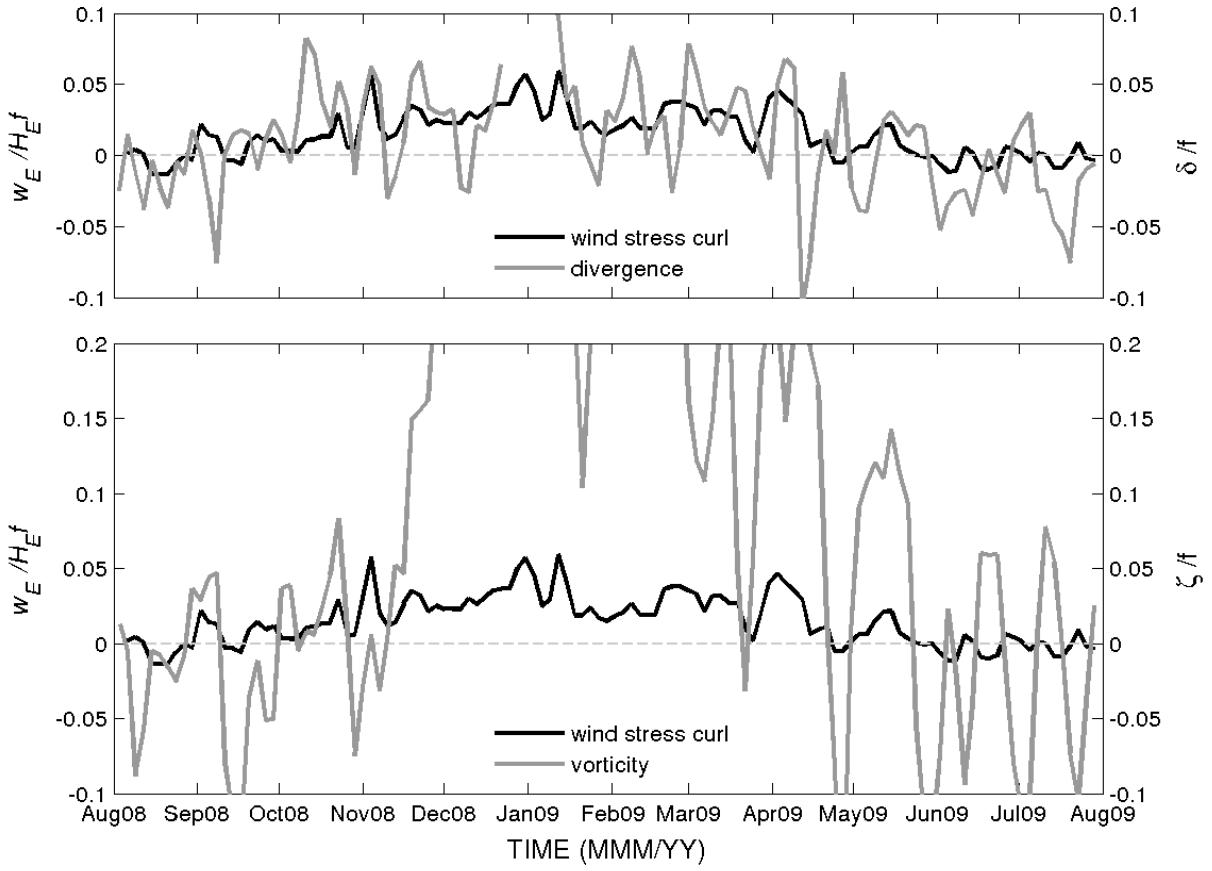

FIGURE 3.20: Time-series of divergence (top) and relative vorticity (bottom) overlaid with scaled Ekman pumping velocity. All terms were normalized by f.

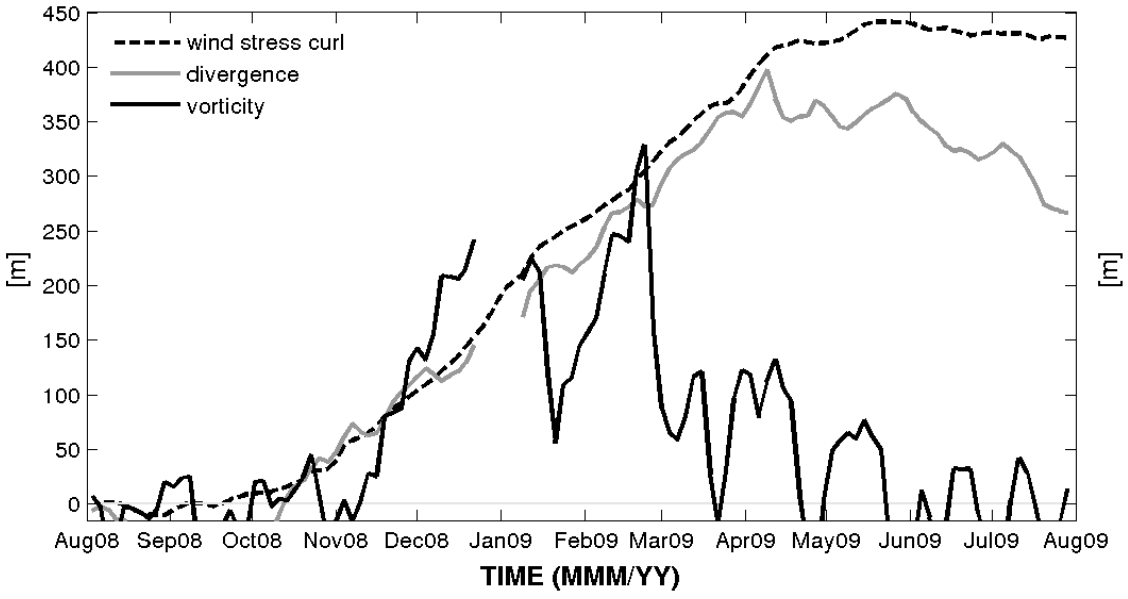

FIGURE 3.21: Vorticity overlaid with time integral of wind stress curl and divergence confined within the Ekman layer ($H_E = 32\ m$).

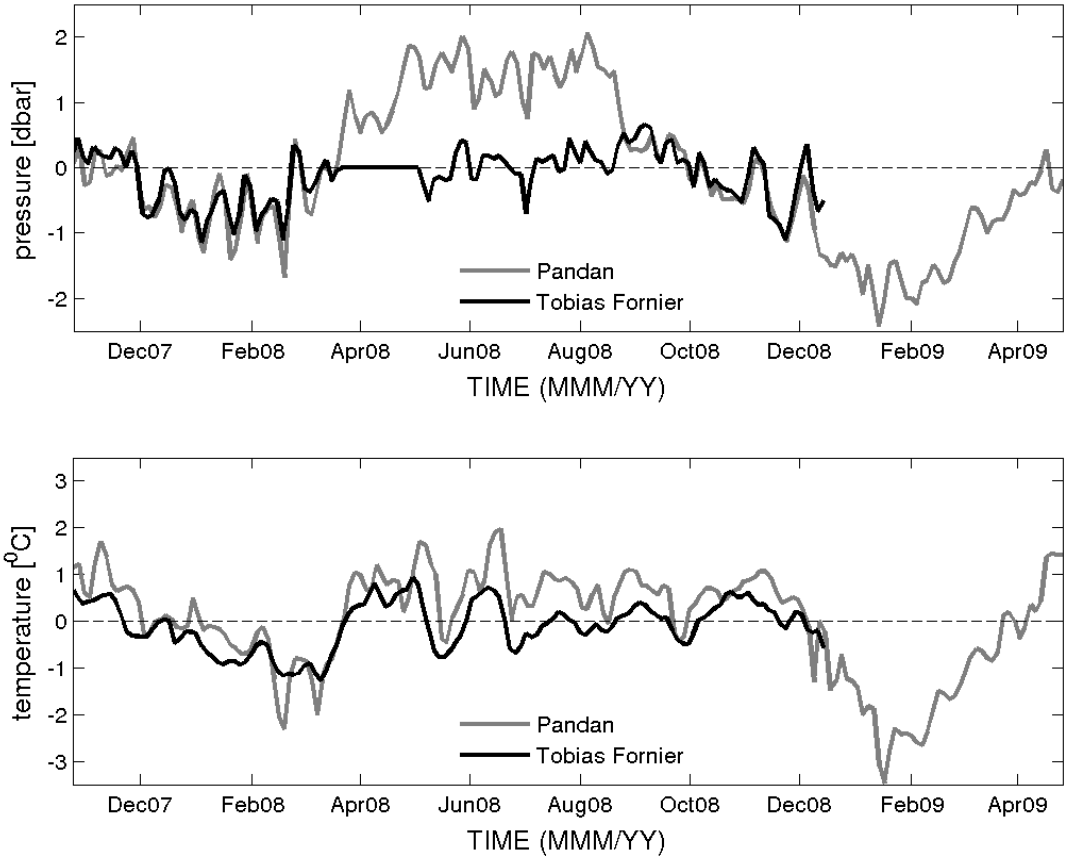

FIGURE 3.22: Time series (top) sea level and (bottom) temperature anomaly from Pandan and Tobias Fornier shallow pressure gauges.

Chapter 4

Coastal sea response to atmospheric forcing in Panay Strait, Philippines

4.1 Abstract

High-resolution 10 m wind forecasts from the Coupled Ocean/Atmosphere Mesoscale Prediction System (COAMPS) show the local atmospheric patterns in Panay Island, that were not fully resolved by the gridded QuikSCAT wind data during the Regional Intensive Observational Period cruises in February-March 2009 (RIOP-09) for the Philippine Straits Dynamics Experiment (PhilEx). The Northeast (NE) monsoon is characterized by distinct wind jets between islands and mountain gaps that generates an alternating band of positive and negative wind stress curl to the right and left downwind of each island. These bands are also observed in the Envisat Synthetic Aperture Radar (SAR) images. The Panay coastal sea response includes formation of a cyclonic Panay Lee (PL) eddy, the relatively smaller cyclonic Panay Tip (PT) eddy on the northwest flank of the island, and the localized coastal upwelling in Pandan revealed by the sea level measurements from the moored shallow pressure gauge and temperature from SBE37 CTD. Multiple sample iterations with TRIAXUS and ADCP repeatedly map subregions covering the PL and PT eddy which resolve tidal variability and low-frequency variability that represents the seasonal response to monsoon winds. The observed features were confirmed by satellite observations of sea surface temperature and chlorophyll concentration provided in near real-time during the PhilEX cruise.

4.2 Introduction

The Philippine Archipelago region is a complex array of islands and semi-enclosed seas with interconnecting straits and sills. Atmospheric circulation is governed by the reversal of the East Asian monsoon and the relatively steady Pacific trade winds. Circulation within and around the Philippines is mainly influenced by a range of processes such as tidal variations, seasonal reversal of the monsoon, sea level variations between West Philippine Sea to the west and the western Pacific Ocean to the east, inter-annual variations such as El Niño Southern Oscillation, and episodic occurrence of monsoon surges and tropical cyclones.

Within the island archipelago, however, finer scale variability both in the atmosphere and the ocean are primarily controlled by island topography and morphology, which adds complexity to the interisland circulation. In a one-way coupled atmosphere and ocean simulation of the Philippine region, monsoon winds interacting with the volcanic topography, lead to strong wind jets between islands and through gaps in the rugged terrain [Pullen et al., 2008]. The model simulations show that steady monsoon winds form stationary lee eddies, while monsoon surges frequently occurring during the winter season trigger oceanic eddy formation and propagation depending on the orientation of the winds in the lee of the islands. Another simulation shows the regional and local nature of atmospheric patterns and the ocean response during RIOP-09 cruise [May et al., 2011]. It confirms that prominent, topographically generated wind jets in the gaps between the islands, and the wakes downwind of the islands are persistent features during the NE monsoon. Local details of the ocean response were revealed using fine-scale atmospheric and ocean model grids while the presence of upwelled nutrient-rich water was supported by elevated chlorophyll concentration in satellite imagery and in-situ measurements [May et al., 2011].

The linkage between atmospheric dynamics and oceanic eddy characteristics was inferred from high-resolution air-sea modelling [Pullen et al., 2008]. Though in reasonable agreement with contemporaneous satellite and in-situ historical data, high spatial and temporal resolution, in both observations and modeling are still needed to confirm.

In this study, coastal sea response to local atmospheric forcing is investigated using current profiles from shipboard ADCP and CTD/fluorometer sections in conjunction with satellite

observations of sea surface temperature and chlorophyll concentration. Along with in-situ measurements during the RIOP-09, time series data of sea level from shallow pressure gauge (SPG), temperature from SBE37 CTD collocated with SPG, and inferred surface current from High Frequency Doppler Radar (HFDR) are used to investigate how the influence of island topography on the local wind regime translates to sea level, surface flows and hydrographic variability.

4.3 Methods

The Office of Naval Research (ONR)-sponsored Philippine Straits Dynamics Experiment (PhilEx) Intensive Observational Period cruise was conducted focusing on the dynamically narrow straits of the Philippines. This multi-disciplinary research cruise was held in February 2009 (RIOP-09) under the NE monsoon regime on-board the R/V Melville (Figure 4.1). Directed by real-time data support such as sea surface temperature, wind speed and ocean color images, successive and multiple transects employing towed profiling vehicle and hull-mounted shipboard 150 kHz ADCP provided the nearly synoptic views of water column hydrography and velocity along the ship track. The hydrographic sections were made by towing a TRIAXUS, an undulating vehicle equipped with physical and optical sensors making quasi-synoptic, high-resolution, three-dimensional surveys of the upper ocean [see Jones et al., 2011, on the TRIAXUS sampling approach]. TRIAXUS maintained a vertical speed of 1 ms^{-1} while typically being towed at 7 knots, with along-track horizontal resolution of 1 km or less, dependent on profile depth. TRIAXUS carried two pairs of Sea-Bird temperature and conductivity sensors along with upward (1200 kHz) and downward (300 kHz)-looking RDI acoustic Doppler current profilers. Here we used all the synoptic measurements obtained during the seven-day period between February 8 and 15, 2009 by TRIAXUS focusing north of Panay Strait which include the Thalweg section between Mindoro and Panay Island, the transect on the northwest (NW) tip of Panay Island, and repeated sections over Pandan Bay to investigate the coastal sea response to local wind forcing. Concurrent and subsequent along-track velocity profiles and repeated sections over Pandan Bay (Figure 4.2) over a 24-hour span were used to resolve the tidal variability within each survey pattern. Cruise data used for analysis were depth profiles of velocity from the shipboard ADCP and conductivity, temperature and chlorophyll concentration from CTD/fluorometer.

In addition, the Naval Research Laboratory (NRL) supplied the real-time atmospheric and oceanic forecasts for the cruises. This NRL coupled atmosphere-ocean model provides simultaneous high-resolution studies of both the meteorology and oceanography of the region. The numerical simulations for the Philippines used the Coupled Ocean/Atmosphere Mesoscale Prediction System (COAMPS), which consists of an atmospheric model coupled with the Navy Coastal Ocean Model (NCOM) [see May et al., 2011, for a more detailed description of the model]. Daily near-surface winds from COAMPS in 9 km resolution and from QuikSCAT in $25km$ resolution were analyzed to determine the effects of the surface winds on the ocean features observed.

The vertical component of the wind stress curl was estimated from the COAMPS 10 m wind stress fields.

$$(\nabla \times \tau).\hat{k} = curl_z(\tau) = \frac{\partial \tau_y}{\partial x} - \frac{\partial \tau_x}{\partial y} \tag{4.1}$$

τ is the 10 m wind stress, x and y are the east and north coordinates, respectively.

Time-series observations of sea surface current in Panay Strait (July 2008 – August 2009) provided by HFDR in conjunction with sea level measurements from shallow pressure gauges (October 2007 – April 2009) were used to examine modifications in the surface flows and sea level in response to local wind forcing. The vector currents generated from the radial component of the current from three HFDR sites located at Pandan, Laua-an, and Tobias Fornier at the western coast of Panay Island undergo quality control prior to the analysis (see Chapter 2 for more detailed description of the data processing). At each, grid point, 75 % temporal coverage of over a year data were used.

The sea level data were obtained from shallow pressure gauges deployed approximately 5-10 m depth just in front of the north HFDR site. Pressure is measured every ten minutes by a Paroscientific quartz pressure sensor with an accuracy of 0.3 mb. Correction for the static inverse barometer (IB) effect of fluctuations in atmospheric pressure on sea level was disregarded since it was found to be far smaller (order of 10^{-2} to $10^{-1} cm$) than the magnitudes of the sea level variability observed. In addition, surface temperature and salinity were obtained from SBE37 CTDs collocated with the shallow pressure gauge.

The tidal components in the time-series data were estimated by performing a harmonic tidal analysis using T-Tide, an open source MATLAB toolbox as described by Pawlowicz et al. [2002]. The tidal prediction time-series were obtained and compared with the shipboard ADCP resolving the tidal variability within each survey pattern.

4.4 Results and Discussions

4.4.1 Cruise Observational data

4.4.1.1 Velocity field

The complexities of the flow of the Panay coastal waters were captured by HFDR and shipboard ADCP that obtain high horizontal resolution of sub-mesoscale features. Though the measurements were made in different temporal resolutions, both the mean and synoptic measurements show predominant surface flows composed of a cyclonic Panay lee (PL) eddy, and a northward Panay coastal (PC) jet which flows along the coast, branches out to the left forming the northern limb of the PL eddy and to the right flowing further north, veers westward and retroflects to form the small cyclonic Panay tip (PT) eddy off the promontory (Figure 4.3).

Two successive surveys in February 8-10, 2009 and February 11-15, 2009 focused on two eddy formations at the lee and off the tip of Panay headland, generating synoptic maps of the apparent flows (Figure 4.4A and B). Multiple sample iterations of each region were performed over a 24-hour span, thus resolving tidal variability within each survey pattern. The first survey focused on the PL eddy (Figure 4.4A). The near-surface velocities (with maximum speed of 95 cms^{-1} over the shallow shelf show a strong shear centered near 11.25 ° N, 121.7 ° E indicating the core of the PL eddy. Its eastern limb, the strong northward PC jet flows along the coast with subsequent flow separation as it encounters the Batbatan Island. The left branch flows westward and shears forming the northern limb of the PL eddy. The relatively weaker right branch flows north close to the coast. An offshore flow is evident as it passes across the mountain gap, then intensifies northward and veers westward as it encounters an abrupt change in the angle of the coastline. It

then slightly shears past the tip of the Panay headland, indicating the formation of the PT eddy.

Figure 4.4B shows a detailed survey of the PT eddy. The measurements start a little further north, which barely captures the shear at 11.3 ° N indicating the core of the PL eddy. However, the survey reveals an energetic cyclonic eddy with maximum speed of about 100 cms^{-1}. Two sections that traverse from the lee of Panay to the tip of the headland clearly show the PL eddy extending further north near $11.64°N$, defined by the strong northwestward PC jet. The strong shears are now clearly visible with subsequent return flow in the surveys close to the NE corner of Panay over Pandan Bay, distinctly indicating a smaller coastal eddy structure.

The two surveys span the seven-day period with one-day sampling (February 10-11, 2009)in Tablas Strait in between, which was designed to obtain measurements across the strait, separating the islands of Mindoro and Panay. The combination of both monsoon-driven and tidally-driven currents predominate in the study area. The first survey was conducted during spring tide and relatively stronger winds, in contrast to the second survey during neap tide and weaker winds. Several locations were occupied during the survey, obtaining one-time measurements of the velocity structure during different wind conditions. The multiple cross-shore surveys covering the eddies over a 24-hour span on the other hand, give an opportunity to resolve current structure during varied tidal conditions.

Panay Lee (PL) Eddy Panay Strait sea level has semidiurnal tidal cycles based on measurements from the shallow pressure gauge moored at Pandan, Antique (Figure 4.5). During the 24-hour successive cross-shore survey of Panay Strait, mixed tidal variability at K_1 (23.9 hours), O_1 (25.8 hours) and M_2 (12.4 hours) periods predominated (Figure 4.6A). The survey was conducted during the NE monsoon regime and spring tide. The sequence of synoptic current vectors from different depths obtained through the tidal cycle has significantly different flow structures (Figure 4.6B and C). During flood tide (left panels), the near-surface current from the 12 m depth bin was intensified over the shelf with maximum speed of 94.5 cms^{-1}, while during the ebb tide (right panels), the intensified flow (60 cms^{-1}) was at about 200 m depth over the channel. This is consistent with the high percentage of variance explained by the four major tidal constituents (O1,

K1, M2 and S2) over the shallow shelf from the HFDR inferred surface currents and in the distinct layer centered at about 250 m from the moored ADCP (see Chapter 5).

Figure 4.7A to D shows the full velocity profiles during the flood tide (left panels) and ebb tide (right panels), providing a comparison of the water-column current structures during different tidal conditions under the NE monsoon regime. Generally, an enhanced current flow with strong shear in the upper (0-130 m) layer is clearly visible indicating the northward PC jet (in red) and the southward flow (in blue) comprising the wind-driven cyclonic PL eddy. Over the deep channel below the PC jet is a southward flow (in blue) with core at depth of about 200 m. A considerable modification of these dominant flows are noticeable over the tidal cycle, with a strengthening of current near the surface during flood tide (Figure 4.7 A and C), and at subsurface (130 m) during the ebb tide (Figure 4.7 B and D).

This sampling period coincides with relatively stronger wind as shown in Figure 4.4 from observations at Caticlan airport. The combined influence of wind and relatively strong tides generate an intensified flow reaching the shallow bottom of the Cuyo Shelf (Figure 4.7A and B). While a more wind-driven surface flow is clearly visible during weaker tides in response to the more easterly prevailing wind (seen in Figure 4.4A) which considerably moved the shear region to the west indicating a shift of the PL eddy westward (Figure 4.7D).

Panay Tip (PT) Eddy Figure 4.8A shows that semidiurnal tidal variability dominates sea level during the intensive survey north of the PT eddy in February 13-14, 2009 (Figure 4.5A). The sequence of synoptic near-surface current maps from the 12 m depth bin obtained through the tidal cycle, as colored accordingly, are shown in panels B to C. Starting at low tide (Figure 4.8B), a transect traversing up to the tip of Panay (in blue) shows a strong wind-driven northwestward flow with maximum speed of 61 cms^{-1} and a strong shear near the tip of the headland, an indication of a PT eddy in that area. At flood tide (in purple), a strong northwestward flow near the tip of the headland is evident with shift of the eddy to the east toward the coast as the tidal height attains a maxima on February 13, 2006 at 1600-hour period. During the subsequent ebb tide (Figure 4.8C, top left), the flow near the tip of the headland veers southwestward and consequently shifts the eddy away from the coast. This oscillation in the current pattern goes on through the tidal cycle. The eastward current towards the coast during flood tide and the westward

current away from the coast during the ebb tide are consistent with the tidal current extracted from the surface current inferred from the HFDR, despite the fact that regions close to the coast were disregarded due to Geometric Dilution of Precision (GDOP).

4.4.1.2 RIOP-09 Cruise Hydrographic data

The TRIAXUS survey near the Panay tip (Figure 4.9) did not coincide with shipboard ADCP. The survey observations started during the slack water at low tide and continued to the flood and ebb tide period as colored accordingly in the sea level measurements in Figure 4.9A. Distributions of temperature, salinity and density show doming of isolines indicating the PT eddy structure captured near the headland, specifically during the 1200-1300 hour survey and during 1700-1800-hour survey. The doming is associated with high chlorophyll concentration with stronger signal at the dome (1200-1300-hour) during flood tide when the current velocity is stronger and the eddy reached deeper (about 100 m) in the water column (Figure 4.9 E)).

Thalweg Distributions A Thalweg section between Mindoro and the Panay straits spanned a 15-hour period during the ebb tide covering a distance from 0 to 87 km (08-Feb-2009 14:01:00 to 08-Feb-2009 21:00:00) and the flood tide at the rest of the transect (08-Feb-2009 21:00:00 to 09-Feb-2009 05:01:35) (Figure 4.10). An examination of this section directly over the channel and across gap between islands provides insight into tidally and wind-driven processes.

During ebb tide, an intrusion of warm and fresh water from Mindoro in the upper 50 m is clearly visible particularly in the salinity profile (Figure 4.10 C, bottom) reaching about 90 km south of the transect. A significant change however is notable at 40 km past the island of Mindoro, eroding the minimum salinity signature concurrent with the intensified southwestward surface current and a 70 m depth core of strong flow toward the Mindoro Strait from the current profile (Figure 4.10 B). This is accompanied further by outcropping of isotherms and isopycnals indicating an enhanced vertical mixing due to intensified northeasterly wind in the gap between the islands. A relatively weak and directionally variable surface current in the lee of the islands of Caluya and Sibay notably formed a weak stratification but as flood tide arrives and the survey track crosses the channel towards Panay Island, a stronger outcropping of isolines occur at about 100 km

followed by a doming which uplift the isotherms and isohalines by 50 m from 100 m depth. These outcropping of isolines in between islands centered at 70 km and 110 m is due to the wind and tidally-driven flow within these channels. Associated with it is an elevated chlorophyll concentration in the upper 80 m of the water column, more so in the section near south Mindoro where two principal rivers, namely Busuanga and Lumintao, drain that may supply nutrients, supporting higher biological productivity in the region. At 120-160 km, the resulting doming of the isolines is due to the PL cyclonic eddy captured during the survey (Figure 4.10 A).

4.4.1.3 T/S Distributions

The direct connection of the Philippine internal seas to the western Pacific are through the shallow San Bernardino Strait, with a sill depth of 92 m, Surigao Strait, with sill depth of 58 m and the deeper Luzon Strait with sill depth of 2200 m. The data from the western Pacific adjacent to San Bernardino Strait displayed a pronounced salinity maxima (s-max) in the 50 to 250 m depth range, 15 to 26 $°C$ temperature interval (Figure 4.11 C) that marks North Pacific Subtropical Mode Water [Hanawa and Talley, 2001].

In comparison, the temperature/salinity (T/S) profile within the Panay Strait region (Figure 4.11 B) shows a weak signal of the North Pacific Subtropical s-max while entering into the confines of the Mindoro and Tablas Straits. At the surface, there are two characteristic water masses, the salinity minimum (s-min) brought by lighter freshwater drained by two principal rivers south of Occidental Mindoro, and the relatively colder and saltier water mass due to shallow upwelling/doming that generates PL and PT eddies and the intense turbulent mixing in gaps between islands. Since the s-min layer lies well above the sill depth in Mindoro Strait, intrusion of this water mass was captured as subsurface flow into the Panay Strait and further south to the Sulu Sea Basin.

At the Mindoro Strait section of the Thalweg, the s-max core is greatly weakened, shown as slight T/S bend near 25.5 $°C$ at 70 m and near 24 $°C$ at 110 m in the Tablas Strait. A deeper s-max in the 150 m near 16 $°C$ however are depicted in all survey tracks, indicating access of Pacific water via the Mindoro and Tablas straits through the Verde Island Passage.

4.4.1.4 Coastal circulation and hydrographic response to atmospheric forcing

Over the NW corner of Panay Island, as the NE monsoon winds are channelled through the river valley, a narrow intense wind jet forms over the Pandan Bay. This offshore wind component directly forces water in the longshore direction. In response, sea level and temperature in front of the mountain gap drops significantly, as observed in the shallow pressure gauge (Figure 4.12, top).

This seasonal cycle is an obvious feature in the sea level and temperature records in response to the reversal of the monsoon wind and clearly defined wet and dry periods in the Philippines. The maximum wind occurs during the NE monsoon regime with magnitude greater than 15 ms^{-1} concurrent with the lowest sea levels and temperatures that reverses during the SW monsoon. However, in April though northeasterly wind still prevails, both sea level and temperature increases as the region experiences a hot dry summer months (February-April) with generally less rainfall. The salinity is forced mainly by local freshwater discharge from the land (Figure 4.12, bottom), closely following the wet season that starts in May to October due to the summer monsoon that brings heavy rains to the archipelago, and due to the intermittent occurrence of tropical typhoons. From the data, two typhoon events were captured, which considerably decreased the salinity readings, during Typhoon Fengshen, known in the Philippines as Typhoon Frank in June 18-13, 2008 that heavily flooded the Panay Island and during Tropical Storm Higos, known in the Philippines as Tropical Storm Pablo in September 29-October 2, 2008.

Seasonal rainfall in the Philippines is known to be modulated by the El Niño Southern Oscillation (ENSO) phenomenon, with ENSO warm (cold) events frequently contributing to drought (excessive rainfall) in many areas. On the regional-scale however, a seasonal rainfall signal reversal was observed affecting the north-central Philippines [Lyon et al., 2006]. The weak signal in 2008 may be attributed to a reasonably strong La Niña that peaked during February-March 2008, which brings less rainfall to Panay Island, in the central Philippines.

The 24-hour repeated shipboard ADCP surveys were averaged to suppress tidal variations and to infer flow generated by wind forcing. Off the coast of Pandan, the mean current weakens and veers with depth to the right of the prevailing wind, indicative of Ekman

dynamics (Figure 4.13A and B). Recall that Ekman layer velocities get more and more perpendicular with the direction of the wind as the water depth reaches the bottom of the Ekman depth. This Ekman transport is seen to reach about 50 m shown as northward flow (Figure 4.13 B, red contour) with about 15 cms^{-1} speed (Figure 4.13 A, with contour line), except at the southwest corner of the survey tracks where a southward retroflection (blue contour at 30 m distance) indicates the structure of PT eddy. This current is comparable with the Ekman drift calculated using the wind stress from COAMPS (not shown) estimated by:

$$\begin{aligned} u_e &= \frac{\tau^y}{f\rho H_e} \\ v_e &= -\frac{\tau^x}{f\rho H_e} \end{aligned} \tag{4.2}$$

where u_e and v_e are zonal and meridional components, τ^x and τ^y are zonal and meridional surface wind stress, $\rho = 1025kgm^3$ is water density and $H_e = 50m$ is the Ekman layer thickness.

A smaller band of positive wind stress curl at the northern tip of Panay (Figure 3.10 in Chapter 3) suggests Ekman pumping as the mechanism that generates the cyclonic PT eddy. And since the region is mainly driven by monsoon reversing winds, it can be considered as persistent and permanent feature similar to the PL eddy during the NE monsoon regime.

4.4.1.5 Satellite Imagery

MODIS Sea Surface Temperature (SST) 7-day composite images for February 7 to 13, 2009 show cooler SST (Figure 4.14, left) collocated with the intensified winds over Tablas Strait in between Mindoro and Panay and at the northwest tip of Panay that blows directly offshore, and warmer SST in the calm lee of Panay Island. In response to intensified winds, mean GHRSST SST data shows a remarkable tongue of cooler water advected by PL eddy over the Cuyo shelf .

The mean profile of water properties from repeated cross-shore surveys near the center of PL eddy shows doming of the isoline contours indicating upwelling of cooler and saltier waters to about 40 m (based on $\sigma_t = 22.5$) excursion near the core (Figure 4.15). This eddy feature was associated with a subsurface chlorophyll maxima (0.045 mg/m^3) found well above the thermocline, with the mixed layer concentration near the core two times greater than the periphery of the eddy.

The satellite imagery provided real time support to the cruise and confirmed the cooling and enhanced chlorophyll concentration over the Cuyo shelf region (Figure 4.16). The seasonal and spatial variations of chlorophyll concentrations, SST, wind fields and wind-induced Ekman pumping over this region were apparent in the 7-year monthly mean remote sensing measurements from October 1997 to December 2004 [Wang et al., 2006]. The seasonal variation of chlorophyll concentrations and SST distributions were associated with the seasonally reversing monsoon winds. The winter (December-February) phytoplankton blooming and the tongue of the cold waters were correlated to the vertical upwelling of cold and nutrient-rich waters drawn by the NE wind. The center of the blooms and location of cold tongues in the gaps between Mindoro and Panay coincide with the maximum of the wind speeds and the Ekman pumping velocities, consistent with the observational results in this study.

Previous studies during the transition to the NE monsoon (October) identified Cuyo Shelf as having abundant fish larvae and inferred it to be a major source of larvae to the Sulu Sea. This is an important information needed to establish an ecologically functional network of Marine Protected Areas (MPA) over the region [Campos et al., 2008].

The survey tracks measuring the water property distribution of the PT eddy did not perform multiple iterations along with the shipboard ADCP thus no mean profile was computed. However, a synoptic profile of temperature, salinity and density clearly revealed a doming of isolines of 50-55 m excursion near the core indicating the cyclonic PT eddy feature (Figure 4.9). This clearly altered the vertical phytoplankton biomass distribution as indicated by increased chlorophyll concentration near the core/doming.

4.5 Summary and Conclusion

In this paper, the response of the coastal ocean to forcing by tides and winds were investigated. Measurements in Panay Strait captured the predominant surface flows composed of the cyclonic Panay lee (PL) eddy, a northward Panay coastal (PC) jet which flowed along the coast, then branched and veered westward while another branch flowed further up north, retroflects and forms the small cyclonic Panay tip (PT) eddy off the promontory. The narrow intense wind jet through the mountain gap blowing directly offshore over Pandan Bay generated an Ekman current, reinforcing a branch of the Panay jet which comprises the eastern limb of the PT eddy.

Panay Strait has a semidiurnal tidal cycle based on measurements from the moored shallow pressure gauge. Repeatedly mapping subregions covering the PL and PT eddy resolved tidal variability. During flood tide, the PL eddy has an intensified near-surface flow over the shallow Cuyo shelf while at about 200 m over the deep channel during ebb tide. The spring tides generate an intensified flow and enhanced mixing over the shelf.

Tidal oscillation is evident for the PT eddy. It shifts eastward towards the coast during the flood tide and westward away from the coast during the ebb tide. A considerable deepening of the PT eddy is also evident reaching the depth of about 100 m during flood tide and only about 50 m during ebb tide.

The PL eddy is significantly bigger, about 100 km, than the PT eddy, less than 15 km in diameter. Since the PL eddy was within the HFDR coverage, details of its generation and evolution were well examined and discussed using inferred surface currents in high spatial and temporal resolution during the NE monsoon. Due to Geometric Dilution of Precision (GDOP) (see Chapter 3), the PT eddy was outside the reduced HFDR coverage thus the formation mechanism was inferred from in-situ shipboard measurements and real-time COAMPS ocean forecast provided during RIOP-09 cruise. Based on the observations and model data, formation and evolution of the PT eddy was inferred to be similar to the PL eddy, that is due to positive wind stress curl that may induce a divergent surface flow which in turn uplifts the thermocline and creates a pressure gradient that spins-up this geostrophic eddy. A branch of Panay coastal jet as its eastern limb was reinforced by the Ekman current driven by the wind jet through the mountain gap blowing directly

offshore over Pandan Bay. Since both are generated during the NE monsoon they tend to be permanent features that persist during this wind regime.

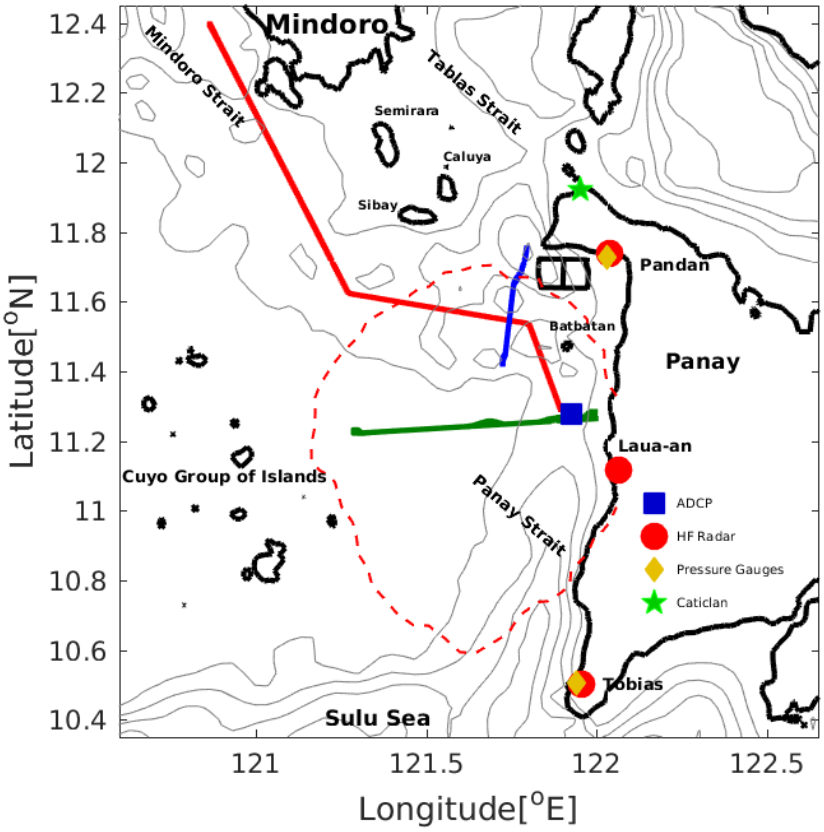

FIGURE 4.1: Bathymetry and TRIAXUS survey transects (solid thick line in red, green and blue) for the Panay Strait region during RIOP-09 in February 8-15, 2009. Marked are the 3 HFDR, SPG located just in front of the north and south HFDR sites, moored ADCP and the nearby Caticlan airport. The 200m, 500m, and 1000m isobaths are indicated by thin gray lines.

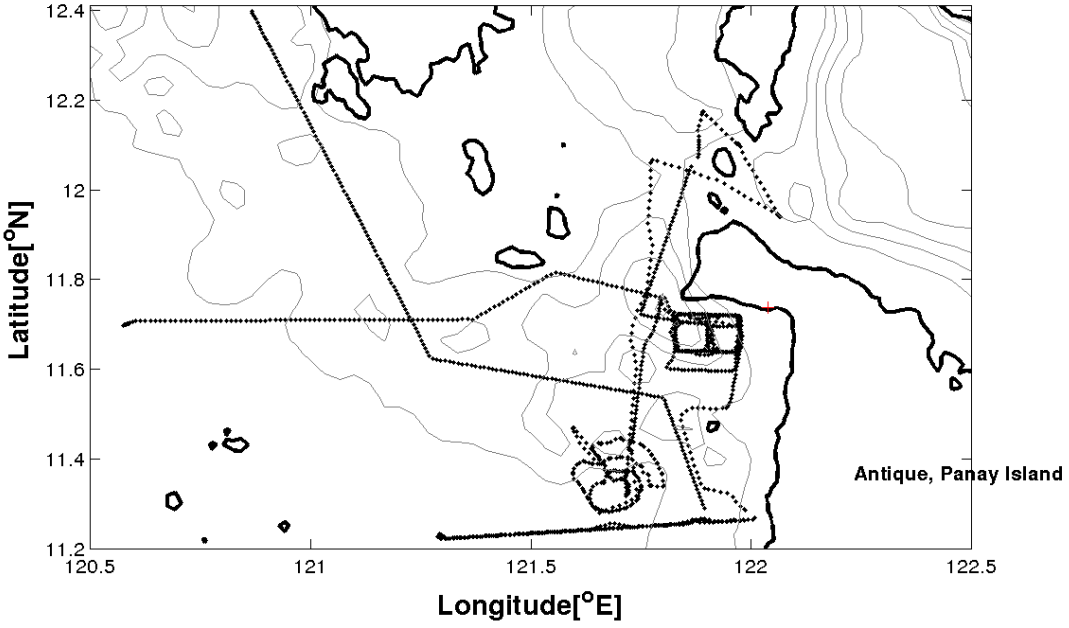

FIGURE 4.2: Bathymetry and shipboard ADCP tracks for the Panay Strait region during RIOP-09 in February 8-15, 2009. The survey region over Pandan bay close to the coast was repeatedly mapped for over a 24-hour period. The 200m, 500m, and 1000m isobaths are indicated by thin gray lines.

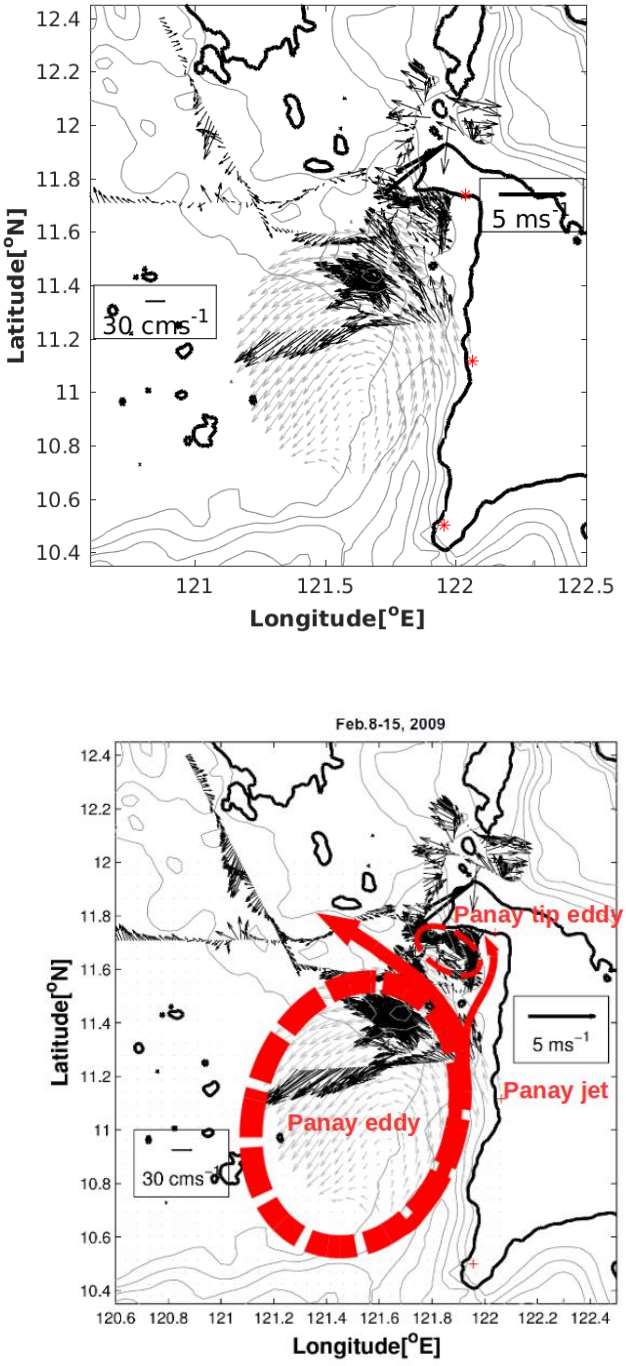

FIGURE 4.3: (top) Surface current from HFDR and from shipboard ADCP. (bottom) Major surface flows observed are the cyclonic Panay eddy, the northward Panay coastal jet and the small cyclonic eddy at the tip of Northwest Panay peninsula.

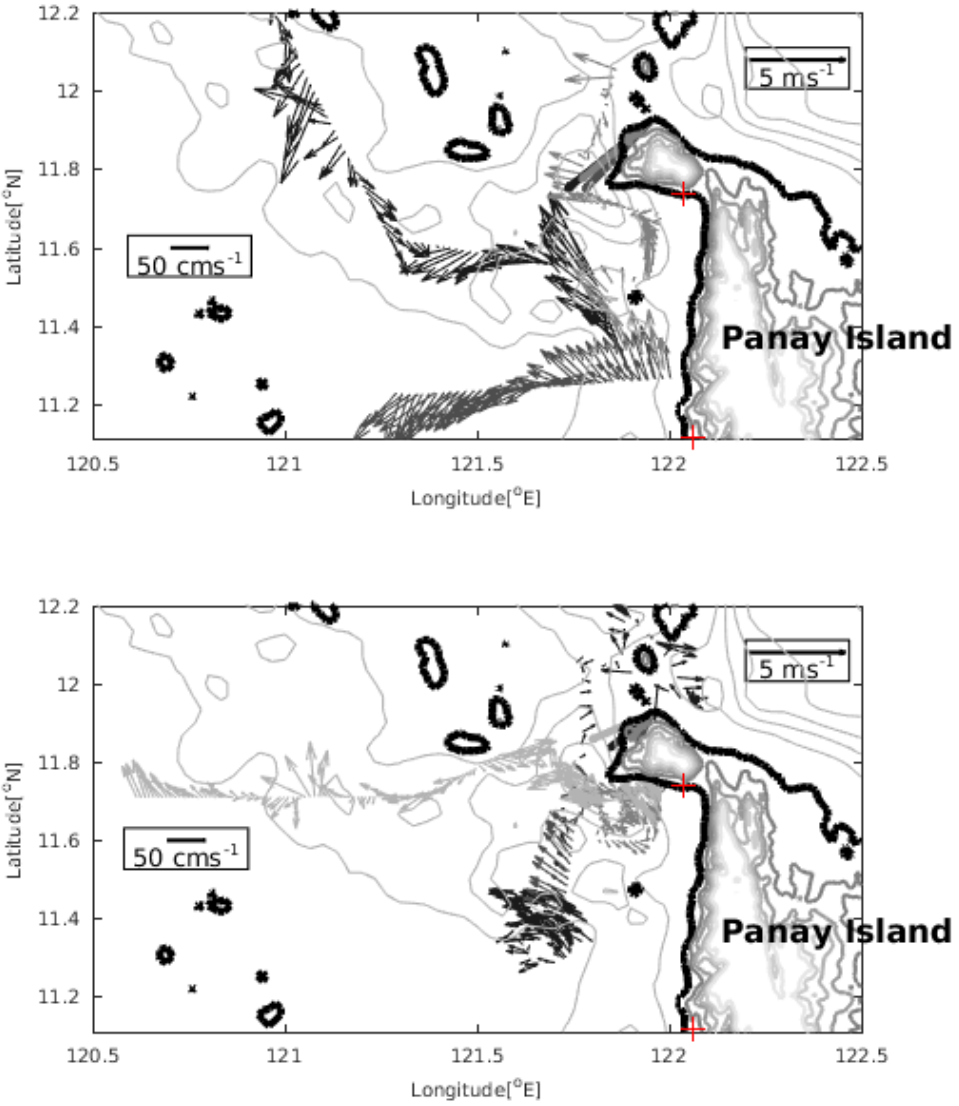

FIGURE 4.4: Near-surface current from shipboard ADCP 12 m depth bin and the prevailing wind from the Caticlan airport during two successive surveys on (top) February 8-10, 2009 and (bottom) February 12-15, 2009. The sampling time from start to end are shown with increasing lighter shadings. The current and wind vectors are color-coded accordingly.

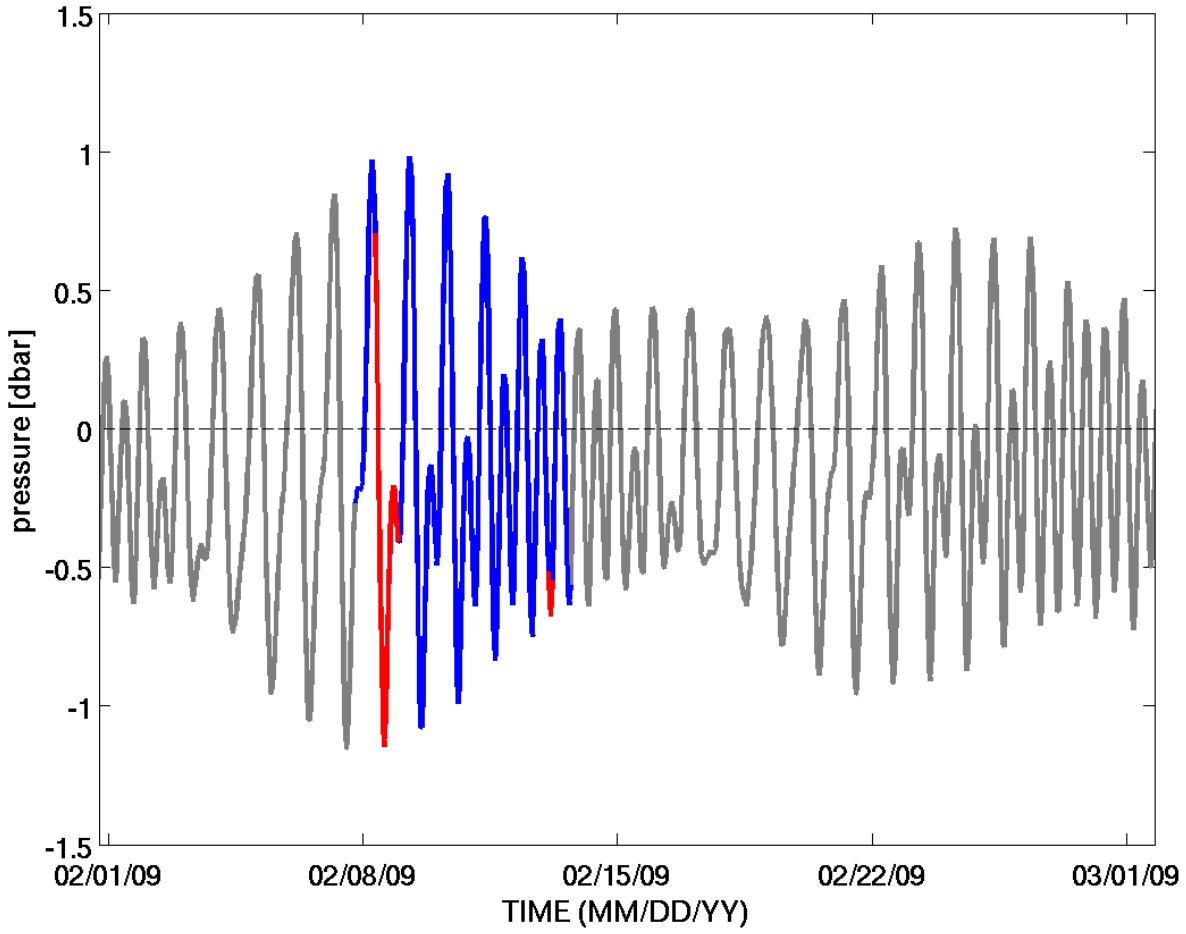

FIGURE 4.5: Measured tidal height at Pandan, Antique, Philippines for February 2009. The location of the shallow pressure gauge is indicated in Figure 4.1 marked with red dot. The blue line represents the tidal height during the survey period, February 8-14, 2009 while the red portion is the tidal height when the two TRIAXUS sections were covered.

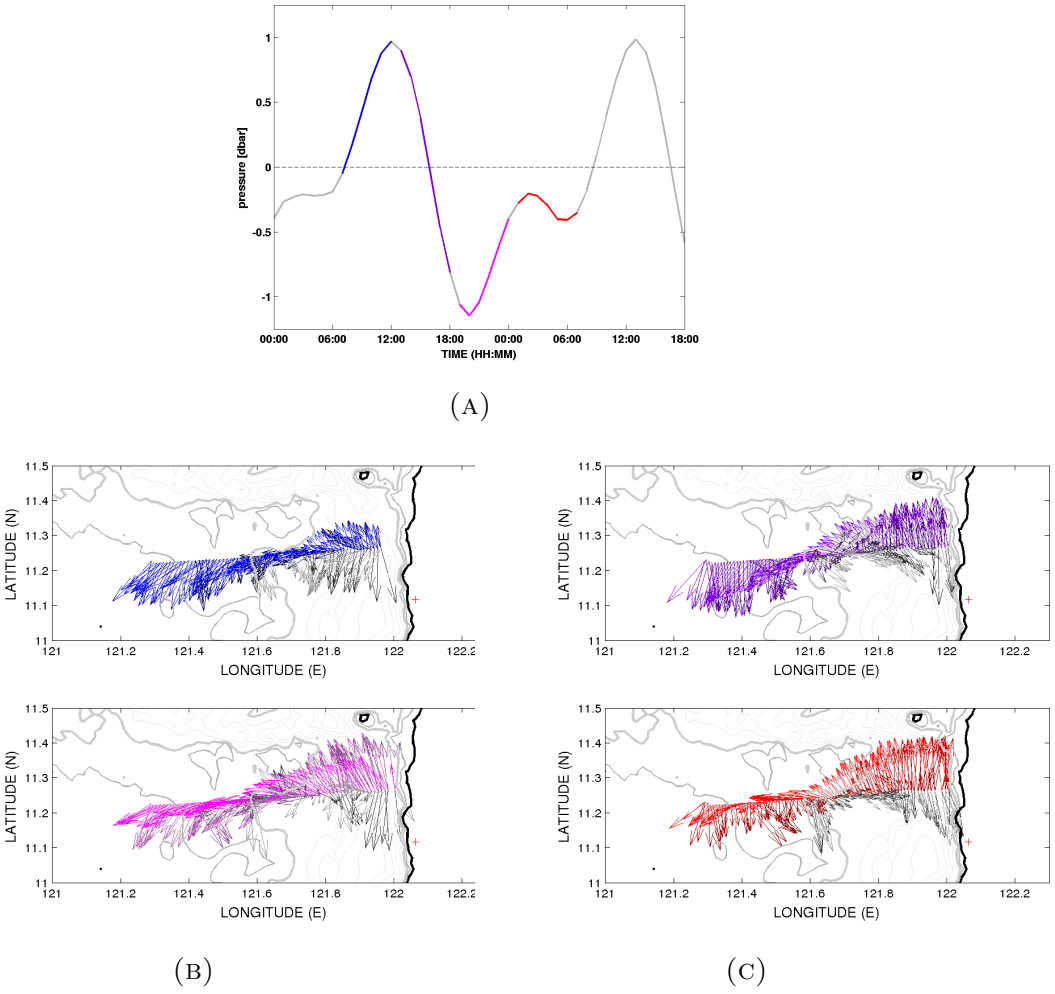

(A)

(B) (C)

FIGURE 4.6: (A) Measured sea level at Pandan, Antique, Philippines for the period of February 9-10, 2009. The colored portion of the tidal series are the tidal height during the period that multiple iterations of each cross-shore transect were covered, from transect 1 to 4 as colored accordingly. Current vectors during (B) flood and (C) ebb tide from 10 m, 50 m and 100 m (colored) and from 130 m and 150 m (gray) are shown. The color shade from light to dark as it goes deeper.

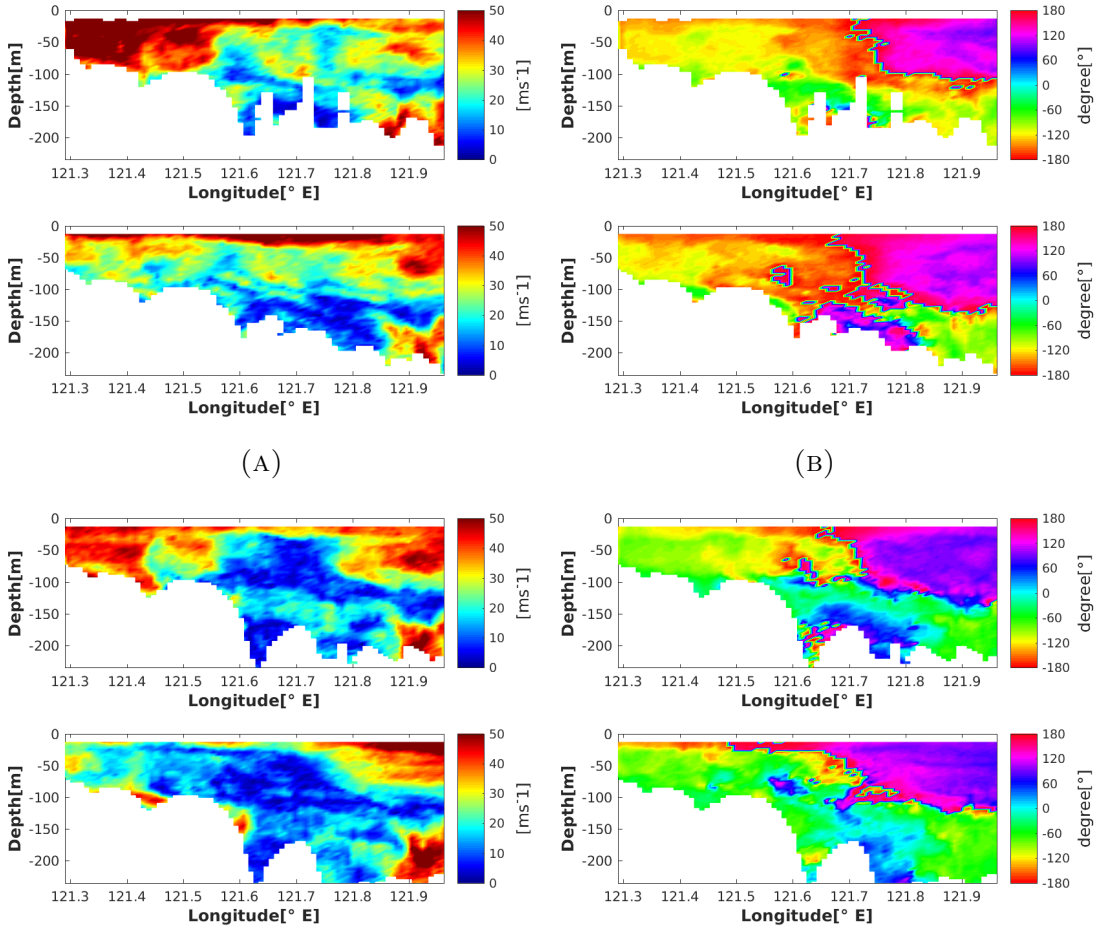

FIGURE 4.7: Speed (left panel) and direction (right panel). Left panel were sampled during flood tide while the right panel were sampled during ebb tide. Positive values are from northeast to northwest direction and negative values are from southeast to southwest direction. -180(° and 180(° is westward while 0(° is eastward.

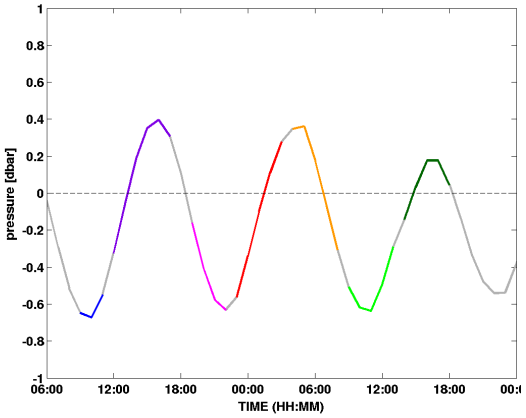

(A)

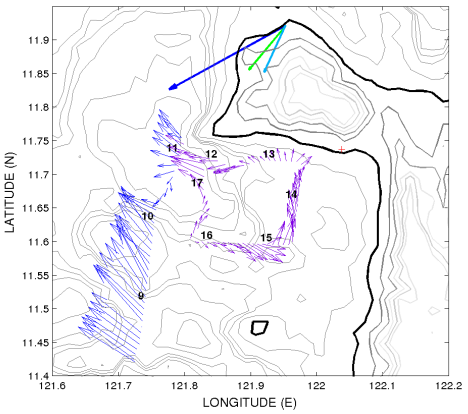

(B)

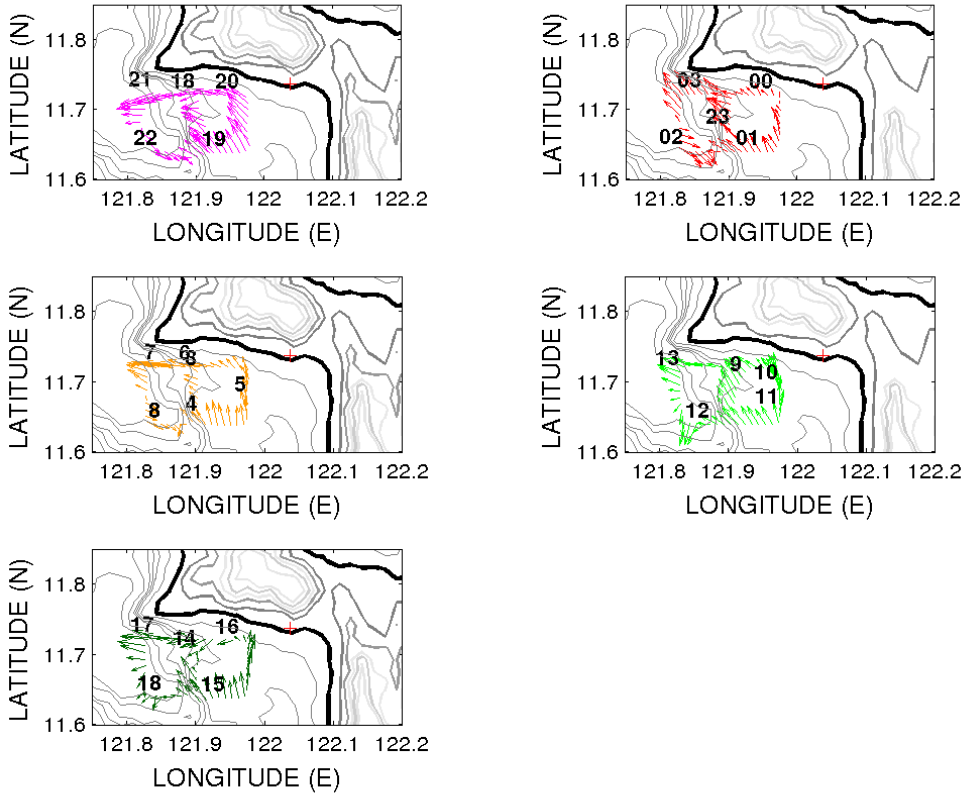

(C)

FIGURE 4.8: (A) Measured sea level at Pandan, Antique, Philippines for the period of February 13-14, 2009. The colored portion of the tidal series are the tidal height during the period that the (B) tip of Panay and (C) multiple iterations of each survey tracks were performed, as colored accordingly. The near-surface currents from 12 m depth bin were labelled with time in hours, left panel (C) were sampled during ebb tide while the right panel (C) during spring tide. The prevailing mean daily wind during February 13-15, 2009 from the nearby airport is shown (blue to green color).

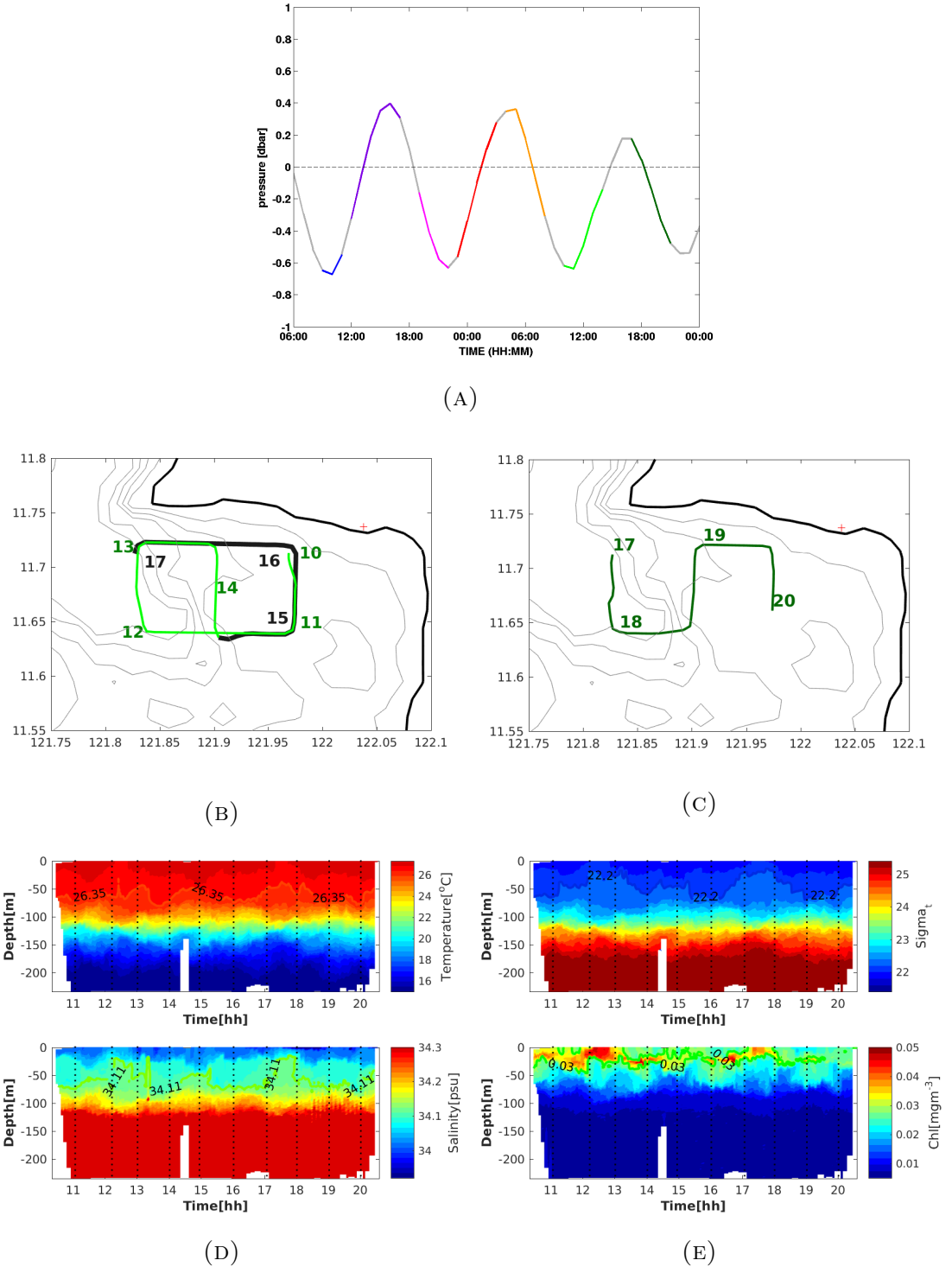

FIGURE 4.9: (A) Measured sea level at Pandan, Antique, Philippines for the period of February 13-14, 2009. The colored portion of the tidal series are the tidal height during flood (B) and ebb (C) tides TRIAXUS survey. The overlapping tracks were colored in gray during flood tide. The points are labelled with time in hours. (D) Temperature, salinity, (E) density and chlorophyll profiles from survey tracks covered above. Vertical dotted lines indicate the time on the tracks.

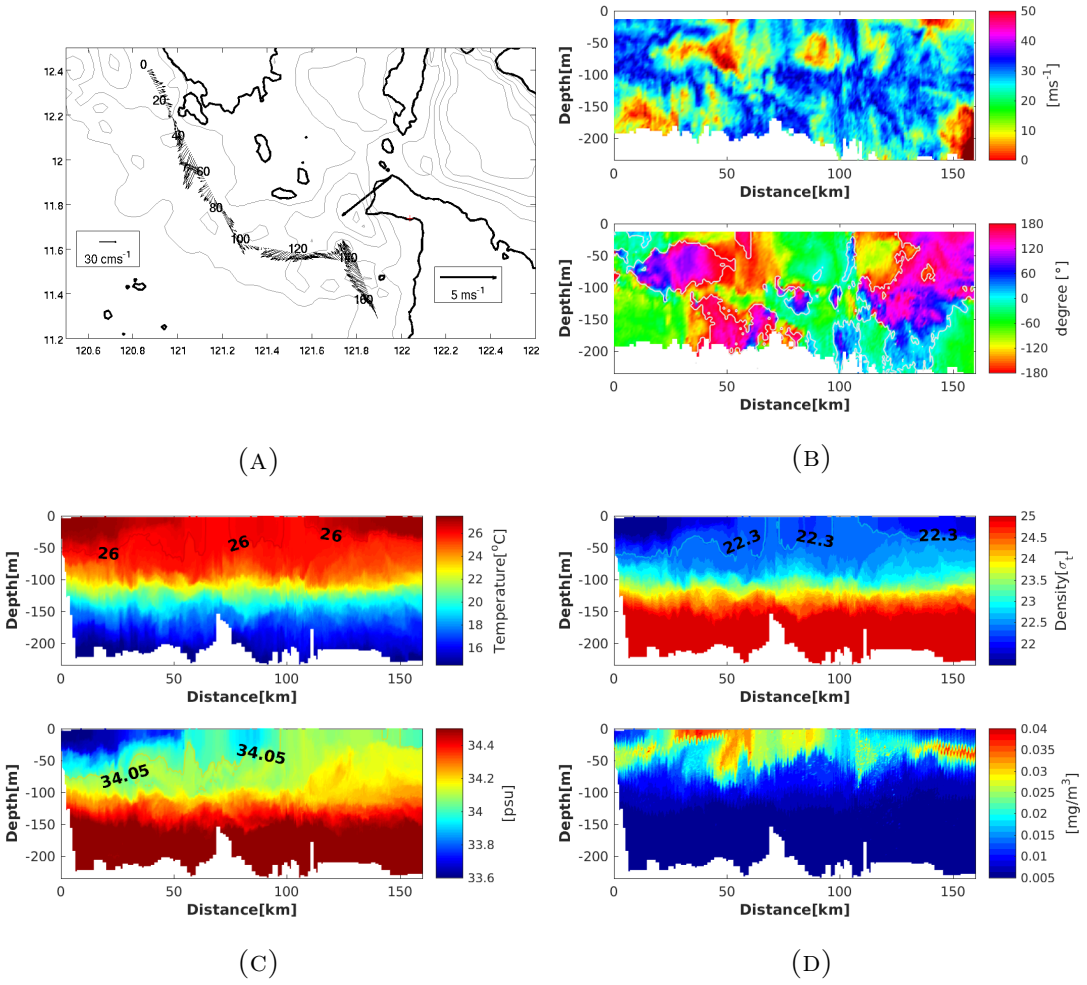

FIGURE 4.10: (A) Wind vectors at Caticlan airport, surface current vectors and (B) velocity profile (top: speed, bottom: direction) from the shipboard-mounted 150-KHz ADCP system. For direction, positive values are from northeast to northwest direction and negative values are from southeast to southwest direction. -180(° and 180(° is westward while 0(° is eastward. (C) Temperature, salinity, (D) density and chlorophyll concentration from CTD and fluorometer attached to TRIAXUS through the thalweg section.

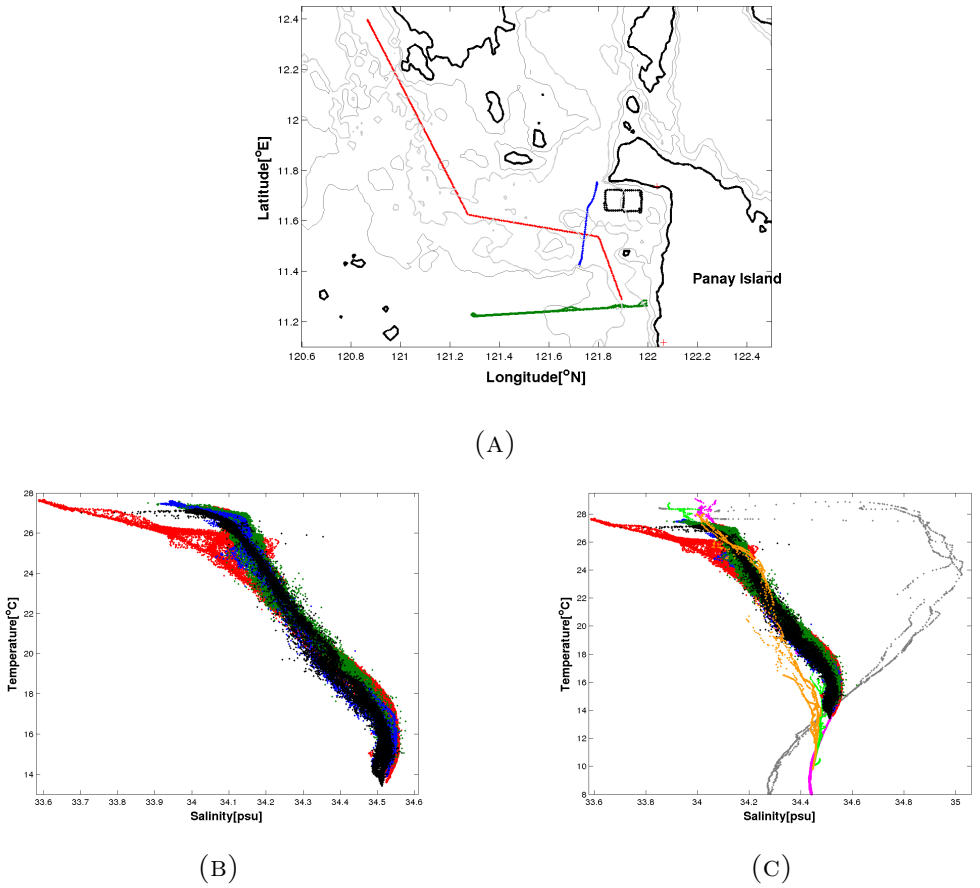

(A)

(B)

(C)

FIGURE 4.11: (A) The TRIAXUS survey tracks for Panay Strait region during February 8-14, 2009. (B) The Temperature and salinity obtained by CTD attached on TRIAXUS and (C) overlaid by temperature and salinity from CTD casts during March 2009 regional cruise showing characteristic water masses from Pacific Ocean and Tablas Strait.

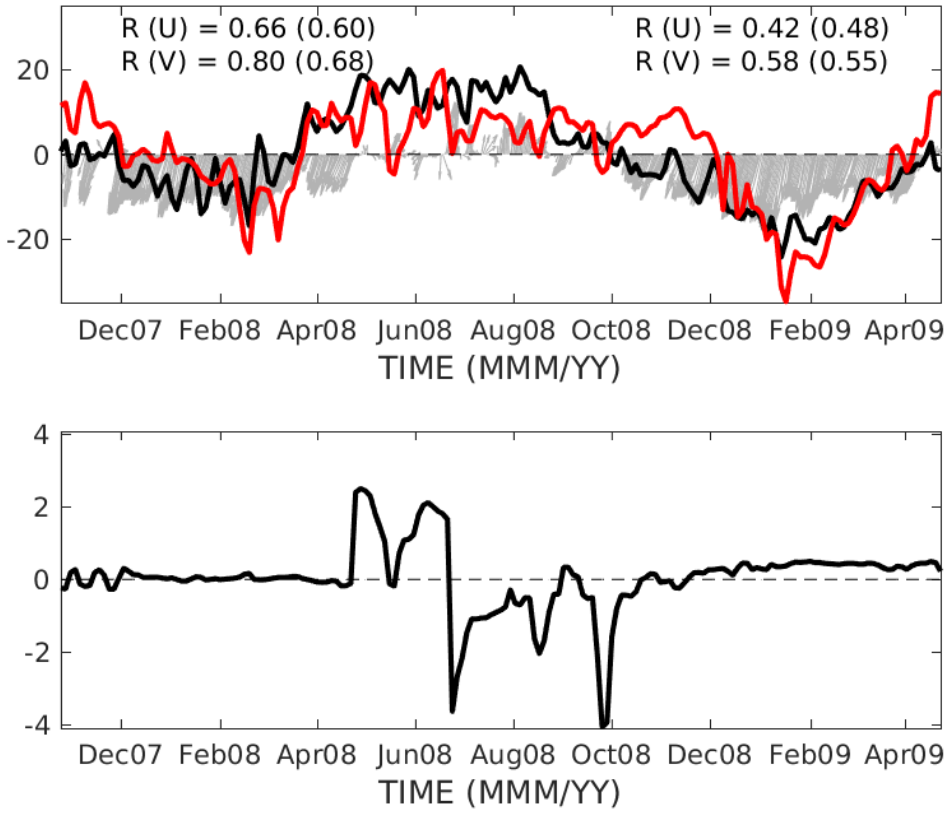

FIGURE 4.12: (top) 6-day medianed sea level anomalies (cm) and temperature (red line, ($^{\circ}C/10$)) from Pandan shallow pressure gauge overlaid with wind vectors (ms^{-1}) from the closest QuikSCAT data. Correlations, R between zonal, U and meridional, V wind component with sea level (left) and temperature (right) are indicated on the top of the plot. (bottom) The corresponding salinity (psu) anomalies.

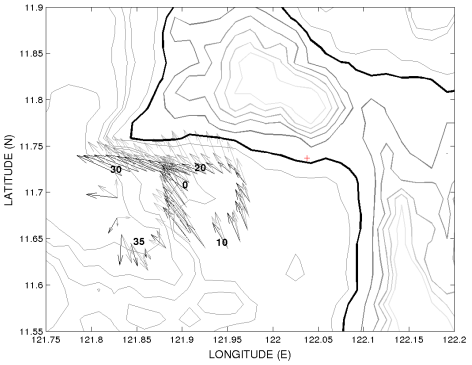

(A)

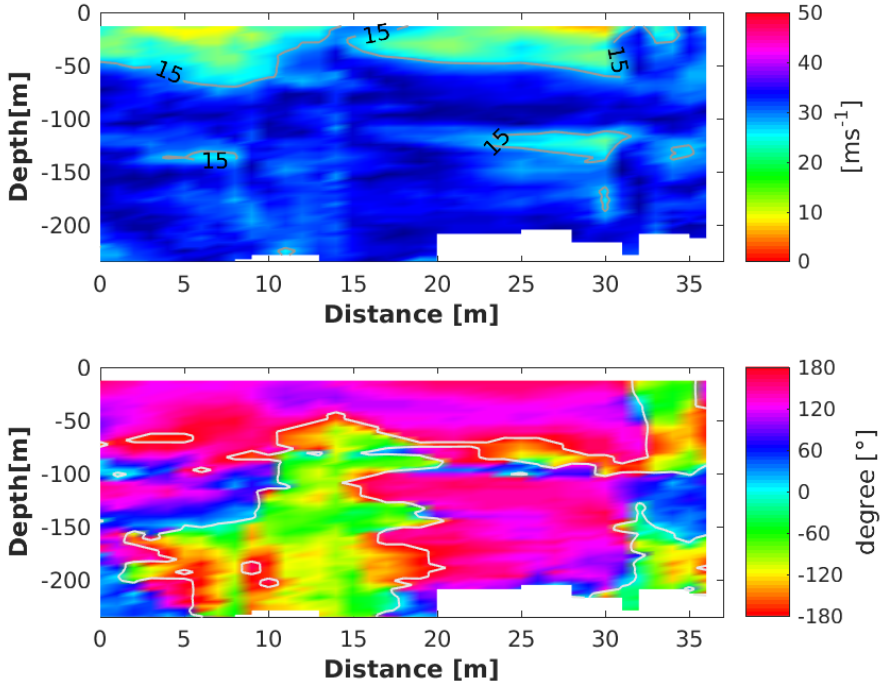

(B)

FIGURE 4.13: The 24-hour mean velocity profile from the NW corner of Panay Island. (A) Current vectors from $10m$, $75m$, and $125m$ with increasingly lighter shadings. (B) On top is the speed while on the bottom is the direction. Positive values are from northeast to northwest direction (white to red contour) and negative values are from southeast to southwest direction (white to blue contour). The y-axis is the distance marked in Figure 4.23 A.

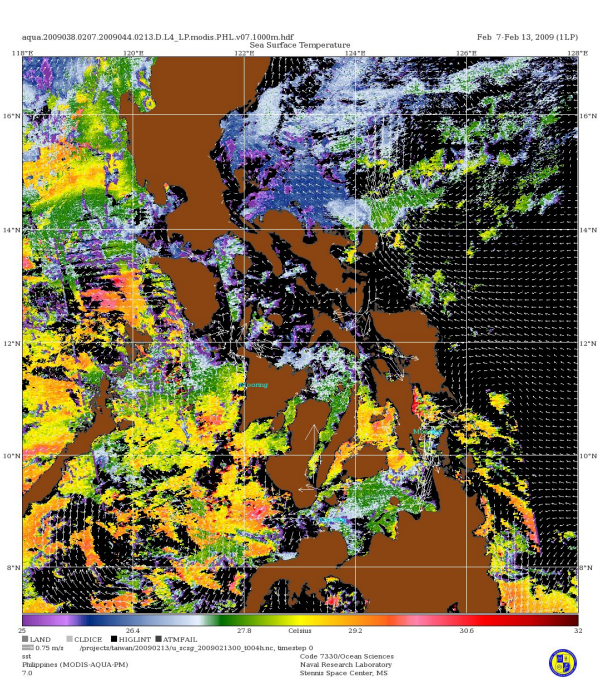

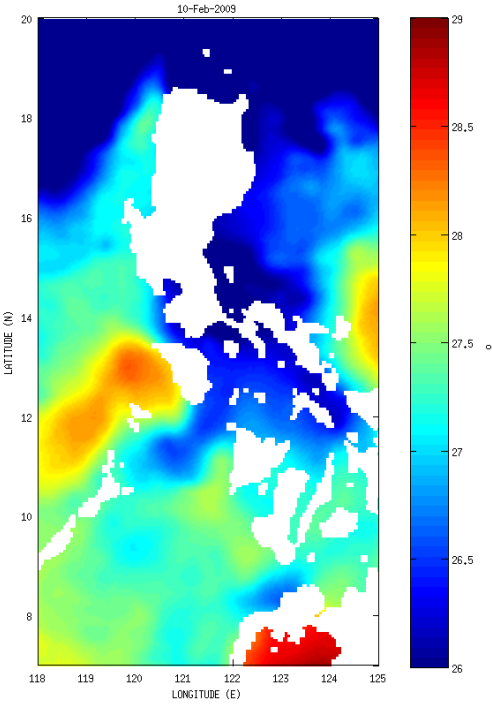

FIGURE 4.14: Sea surface Temperature (SST) for the Philippine Archipelago. The image is a 1 *km* composite of MODIS Aqua sensor image for the period February 7 to 13, 2009 (top) and the 6 *km* daily Group for High Resolution Sea Surface Temperature (GHRSST) Level 4 SST data (daily mean values provided by Physical Oceanography DAAC (http://podaac.jpl.nasa.gov/dataset/UKMO-L4HRfnd-GLOB-OSTIA) averaged over the same time period (bottom).

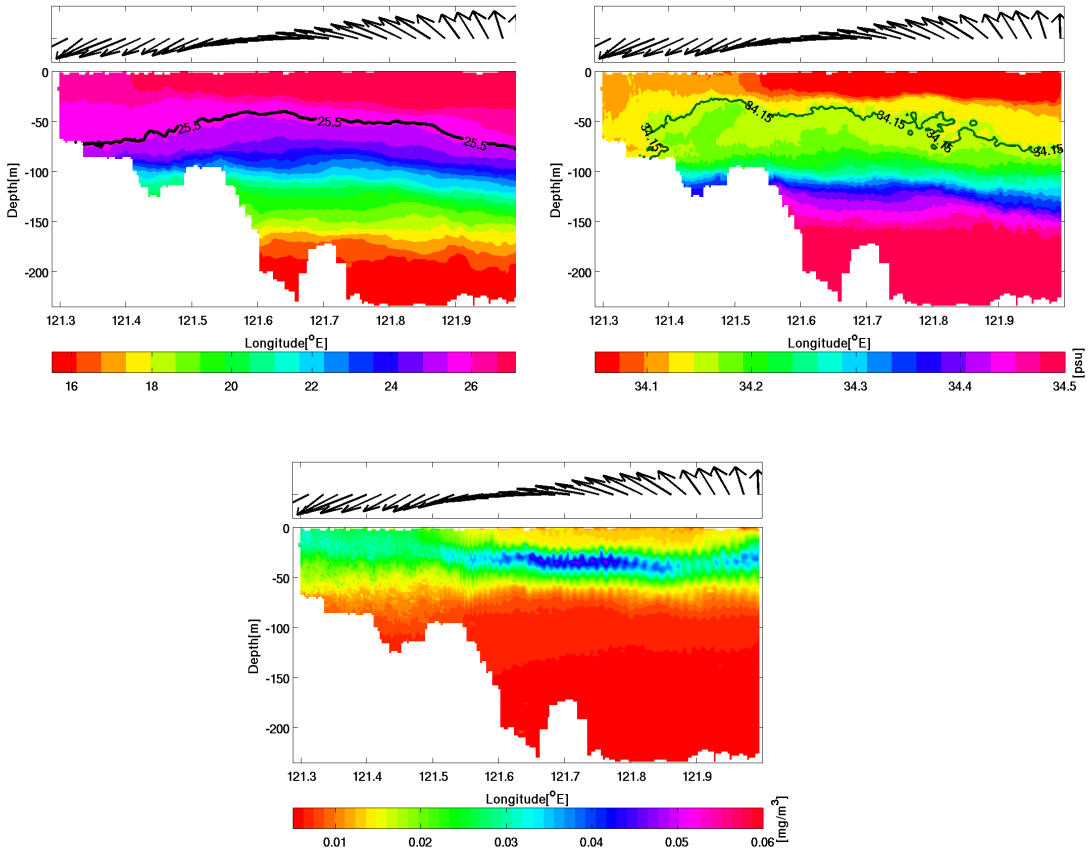

FIGURE 4.15: Mean profile of temperature, salinity and chlorophyll concentration across the PL eddy during the hydrographic survey (February 8-9, 2009).

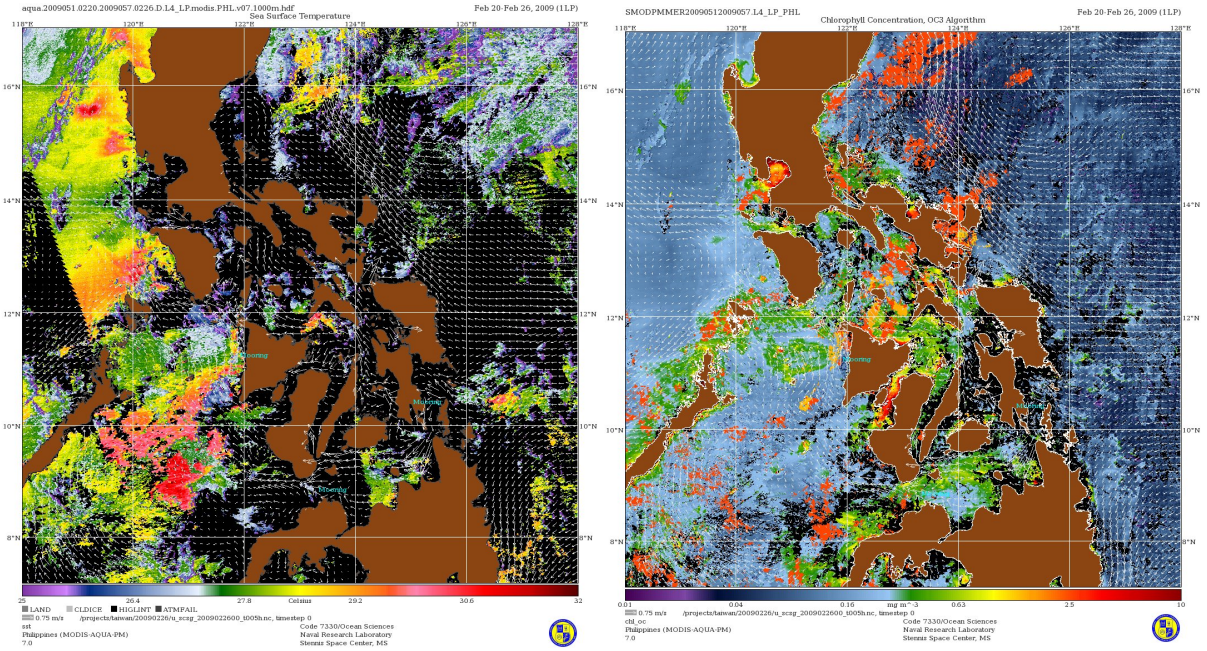

FIGURE 4.16: The Sea Surface Temperature (SST) 1 km MODIS Aqua Imagery composite images and the Chlorophyll concentration merged (MODIS, MERIS, SEAWIFS) composite images of Philippine archipelago for February 20 to 26, 2009.

Chapter 5

Barotropic and baroclinic tides in Panay Strait, Philippines

5.1 Abstract

The Panay Strait constitutes a topographically complex system with intense tidal currents. The four major tidal constituents in the total energy spectra inferred from sea level and current profiles are K_1, O_1, M_2, and S_2. Spatially, O_1 and M_2 dominate over K_1 and S_2, respectively. The diurnal tide accounts for highest amplitude variability over the shallow shelf while semi-diurnal tides over the deeper channel of the strait. Rotary spectra of surface currents shows inertial frequency peaks and exhibit an unusually broad peak in both the clockwise (CW) and counterclockwise (CCW) rotating components, indicating frequency shift by the vorticity of sub-inertial currents prevalent in the region. Vertically, variance of the horizontal velocity explained by the major tidal constituents peaks in two distinct depth bands; the upper layer centered at 110 m (11% variance) dominated by semi-diurnal tide (M_2) and the lower layer at 470 m (26% variance) dominated by diurnal tides (O_1). Semi-diurnal tidal current ellipses (M_2 and S_2) exhibit a dominance of CW motions at near-surface depth ($110m$), indicative of downward energy propagation and implying a surface energy source. These features from Acoustic Doppler Current Profiler (ADCP) deployed close to the sill is consistent with the dominant semi-diurnal tide (M_2) over the channel of the strait from the High Frequency Doppler Radar (HFDR). Comparison of incoherent to coherent tidal energy shows K_1 dominated the incoherent tidal

band. Spatially, incoherent energy is dominant over the channel particularly near the sill and the constricted part of the strait. The incoherent portion of the tide is presumably attributable to the surface expression of the internal tide which seems to be generated near the sill and then topographically steered west over the edge of the shallow shelf where incoherent energy is dominant.

5.2 Introduction

Tidal currents constitute the most ubiquitous signal in the coastal ocean. They can be difficult to interpret as they vary at multiple topographic scales. The Philippine archipelago bounded by the Pacific Ocean on the east and South China Sea (SCS) on the west, consists of a complex array of islands, embayments and seas connected by multitude of straits and sills. The barotropic (depth-independent) tidal components are significant in the region with strikingly different geographical structures, dominated by semi-diurnal tides in the Pacific and diurnal tides in the SCS. Within the Philippines, strong barotropic tidal flows through many of the passages reflect the substantial tidal surface height differences between the Pacific and SCS, as well as acceleration through topographic constrictions.

Tidal currents flowing over topography in a stratified ocean give rise to baroclinic internal tides. In the interior Philippine seas, the largest known internal tide sources are in the Sibutu Passage, south of Sulu Sea (SS)[Zhang et al., 2010]. A strong surface signature was illustrated by the Moderate Resolution Imaging Spectroradiometer (MODIS) true color sunglint image of the western SS [Hurlburt et al., 2011] and simulations of tides in the Philippine archipelago clearly represent this surface signal and further indicates that internal tides are pervasive within the Philippine seas. Jackson et al. [2011] found internal waves observed by satellite imagery and Girton et al. [2011] from in situ data in several areas within the Philippine archipelago. Likewise, Apel et al. [1985] found internal tidal beams generated in Sibutu Passage that propagate across the SS.

Aside from the well-known solitary wave occurrences in the SS [Apel et al., 1985; Hurlburt et al., 2011; Tessler et al., 2010] and the Sulu Archipelago [Jackson et al., 2011], concentrations of nonlinear internal wave activity on the shelf region (Cuyo Shelf) at

the northern end of the SS between Palawan and Panay islands was observed in synthetic aperture radar (SAR) and optical sunglint satellite imagery ([Jackson et al., 2011]. These waves dissipate over the shallower shelf region after 2.5days of traveling from several locations in the Sulu Archipelago [Jackson et al., 2011]. Simulations of tides in the Philippine seas by 1/12° Hybrid Coordinate Ocean Model (HYCOM) also note the strong sea surface height signature of internal tides in Mindoro strait [Hurlburt et al., 2011]. Internal wave measurements from two McLane Labs moored profilers (MMP) at either end of Mindoro-Panay Straits illustrate some similarities and dramatic contrasts over fairly short distances within archipelagic topography. There are more energies to both the diurnal and semidiurnal frequency band in Mindoro Strait to the SCS while at lower (sub-inertial) frequencies with larger isopycnal displacement at depth, south of Panay Strait entering into the SS [Chinn et al., 2012].

The Panay Strait serves as the major path way of water from the SCS via the Mindoro Strait to SS (Figure 5.1). A small basin ($1300m$ deep) known as the Semirara Sea separates the Panay Strait from the Mindoro Strait on the northwest and Tablas Strait on the northeast. A sill of 578 m depth forms the shallowest point within the strait. Defining the $100m$ isobath as the outer edge of the shelf, Panay Strait is bordered by the wider Cuyo shelf on the west and the very narrow Panay shelf on the east. On the shelf lies the low lying Cuyo Group of Islands and extensive reefs. The Panay Strait thus constitutes a topographically complex system of small low-lying islands, seamounts, shelves, sills, and a deep basin that may be a locale of intense tidal currents.

This study is primarily directed towards determining the structure of the barotropic and baroclinic tide in Panay Strait. Knowledge of oceanic processes, specifically tides is important to understand their specific impact on the currents, stratification, and nutrient distributions in the region.

5.3 Methods

For the description of tidal sea level and current oscillations, data from HFDR measurements, one moored ADCP and two shallow pressure gauges (SPG) were used. Their record lengths vary from 368 to 646 days (Figure 5.2) with about 142 days of overlap.

Failures in HFDR occurred at sites due to electrical power loss primarily because of burned power cables and generator failures during black-outs. In times when data are lost from one site, two sites were used to calculate vector currents. During the deployment period, the largest data loss was during the bistatic calibration performed from December 22, 2008 to January 9, 2009. Moored instruments were deployed and retrieved at different times, and overlaps of uninterrupted coverage were selected for analysis.

The HFDR current vectors underwent minor quality control prior to the analysis. Missing data segments were subject to temporal interpolation [Chavanne et al., 2007] in which a constant linear trend and sinusoids at M_2, K_1 and inertial frequencies were least squares fitted to the observations available in a 3-day window centered on each missing data segment shorter than 36 hours. The fit was performed only if more than 36 observations were available. This interpolation was carried out on hourly vector currents.

In conjunction with the HFDR, an ADCP mooring was deployed as part of the Exploratory Cruise on the R/V Melville in June 2007 to provide aspects of the full three-dimensional circulation in Panay Strait. An upward-looking RDI Teledyne Long Ranger 75-kHz, bottom mounted ADCP (11.2790 $°N$, 121.9244 $°E$) was located inside the region covered by HFDR, 2.5 km downstream from the narrowest constriction at Panay Sill of 578 m water depth. The passage width is 36 km determined between the 100 m isobaths on either side of the mooring as surveyed by multibeam echosounder. The ADCP included pressure and temperature sensors. Sampling rates were set to resolve the tides, and were 30 minutes for the ADCP and 15 minutes for the temperature sensors. The mooring was recovered in March 2009.

The ADCP returned 100 % of the velocity time series. However, due to surface reflection contamination, the bottom-mounted ADCP was unable to resolve the near surface velocity (upper 50 m). Pressure time series were used to correct for mooring blowover. The velocity data were then linearly interpolated onto a 10 m depth grid and a common time base of 1 hour.

As part of the PhilEx program, an array of shallow pressure gauges was deployed at approximately 5 - 10 m depth along Panay Strait (Pandan and Tobias Fornier, Antique). The location, deployment period and length of observation of the pressure gauges are provided in Figure 5.1 and (Figure 5.2). Absolute pressure is measured every ten seconds by a Paroscientific quartz pressure sensor with an accuracy of 0.3 mb (-1 % of the signal).

The data were averaged into hourly bins and were used to examine possible influences of sea level to the tidal variations in Panay Strait.

Spectral analysis is useful to partition the variance of a time series as a function of frequency [Emery and Thomson, 2004]. The present study utilizes power spectrum of sea level and rotary spectral analysis [Gonella, 1972] to the HFDR-derived surface current and current profile from the moored ADCP. These provide estimates of power (energy density) distributed over a range of given frequency bins [Press et al., 1996]. Spectral estimates were spatially-averaged for surface currents and vertically-averaged for the ADCP current profile. The sea level spectra were further assessed to extract the tidally-driven current from the time-series data.

HFDR and ADCP current components (zonal and meridional) and sea level, were harmonically analyzed using the T-Tide Matlab package [Pawlowicz et al., 2002] over the deployment period of each instrument. Four significant tidal constituents (K_1, O_1, M_2, S_2) inferred from sea level were least square fitted to the hourly observations, along with a constant and a linear trend. The 95 % confidence intervals were computed by a bootstrap method. Maps of tidal current ellipses, major axis amplitudes and phases will be use to characterize the surface tidal currents.

5.4 Results and Discussions

5.4.1 Tidal components inferred from sea level

Phase-locked tidal sea level explains 95.1 % and 96.9 % of the total sea level variance over a year (425 days) from hourly records from Pandan and Tobias Fornier, respectively. The frequency spectra of sea level variations shows energy peaks at four major constituents (K_1, O_1, M_2, and S_2) (Figure 5.3).

The contribution of major constituents to the total energy spectra of sea level is shown in Figure 5.4. An increase in the variance is largely attributed to K_1, O_1, M_2, and S_2, respectively. These four major constituents will therefore be use to extract tides for analysis.

5.4.2 Horizontal structure of the tidal components inferred from HFDR

The most energetic surface current variations for periods shorter than 5days are inertial and tidal currents. The spectral properties of surface currents within the radar domain shows diurnal peaks centered on K_1 and O_1, semi-diurnal on M_2 and S_2, and inertial frequency on f_i with period of 62 hours (2.59 days) at $11.1°N$ (Figure 5.5). The O_1, K_1, M_2 and a much weaker S_2 are the most significant with minor contributions from other constituents. Higher harmonics of diurnal and semi-diurnal constituents also display significant peaks.

The rotary spectra decomposes a vector time series into CW and CCW rotating components by frequency. At near-inertial periods, the CW predominates in the Northern Hemisphere due to the action of the Coriolis force to the right of the velocity vector. This is evident in the spectrum where inertial frequencies have more energy in the CW rotating band as expected and are unusually broad (maximum 1.46 $m^2s^{-2}.cph^{-1}$), possibly frequency-shifted due to vorticity of sub-inertial currents (see Chapter 3) and the forcing by wind, both prevalent during NE monsoon [Pullen et al., 2008]. For diurnal and semi-diurnal frequency bands, CW motions are also more energetic than the CCW components by 1.47 $m^2s^{-2}.cph^{-1}$ and 1.18 $m^2s^{-2}.cph^{-1}$, respectively.

Variance explained by the four major tidal constituents constitute 5.7 % and 9.4 % of the total variance of zonal and meridional current components over the 1-year record, respectively (Figure 5.6). The highest variance for the zonal current component is over the deep channel further south of the sill and for the meridional component north of the sill near a sharp bend in bathymetry where the Island of Batbatan is located. The semidiurnal tide contributed much to the highest variance over the deep channel while the diurnal tide over the shallow shelf (Figure 5.7).

To determine the relative contribution of the tidal currents to the mean kinetic and mean eddy kinetic energies (EKE), those parameters were calculated and are shown in Figure 5.8. The tidal currents, u_p and v_p were formed from the four major tidal current constituents analysed. EKE tends to be greatest where the mean circulation is strongest west of the radar domain, over the shelf but low on the east along the coast. This implies that the seasonal PL eddy derived more of its energy from the seasonal return flow as

a consequence to the positive Ekman pumping generated over this region during NEM regime and less energy from the persistent Panay coastal (PC) jet as the eastern limb of the PL eddy. In comparison, the mean tidal current kinetic energy is an order of magnitude less than both the mean current and mean EKE.

The relative contribution of the tidal currents to the mean kinetic energy was estimated by the ratio:

$$R_{tmke} = \frac{\overline{u_p^2}(x,y) + \overline{v_p^2}(x,y)}{\overline{u^2}(x,y) + \overline{v^2}(x,y)} \tag{5.1}$$

where u and v are observed current velocities and the overbar denotes a time mean of over a year record and, x and y denotes the conventional Cartesian coordinates.

Similarly, the contribution of the tidal currents to the mean eddy kinetic energy was estimated by

$$R_{teke} = \frac{\overline{u_p^2}(x,y) + \overline{v_p^2}(x,y)}{\overline{u'^2}(x,y) + \overline{v'^2}(x,y)} \tag{5.2}$$

where the primed quantities denote deviations from the time mean over a year.

The distributions of R_tmke and R_teke are shown in Figure 5.9, while the distributions of O_1 and M_2 constituents, which contribute much to the tidal kinetic energy, are shown in Figure 5.10.

The contributions of the tidal currents to both the mean current and the mean EKE show similar patterns though their contribution to the mean eddy kinetic energy is relatively large ($R_tmke = 0.043$ and $R_teke = 0.0510$). The regions with highest contributions are on the shallow areas of the Cuyo shelf where there are sharp bends in the 100 m isobath and over which the persistent northward PC jet exists. This suggests the influence of tidal currents on the PC jet, as it accelerates over the shallow part of the shelf. Another high contribution is on the west end of the radar domain, where a strong return flow indicating the PL eddy approaches the 100 m isobath of the shallow Cuyo shelf.

From the 4 major constituents, O_1 and M_2 contribute the highest to the mean tidal kinetic energy where O_1 dominates over the shallow shelf while M_2 over the deep channel

with sharp bends observed in the 100 m isobath and over which PC jet intensifies as it approach the narrowest constriction of the strait.

5.4.3 Vertical structure of the tidal component inferred from ADCP

For the mooring located near the relatively narrow part of Panay Strait, tidal variability makes up a large part of the velocity signal. The vertically-averaged frequency spectrum from the ADCP is very similar to the spectrum from HFDR for periods shorter than 5 days showing strong peaks at K_1, O_1, M_2, and S_2 tidal components (Figure 5.11). The O_1 and M_2 constituents dominate the diurnal and semi-diurnal bands, respectively. Strong energy in the inertial band is absent in the spectrum, presumably because the data in the upper profile (top 50 m) are missing. This suggests the importance of the local wind in generating the peaks in the near-inertial motions from HFDR-derived surface current spectrum.

The large percentage of variance explained by the 4 major tidal constituents (K_1, O_1, M_2, and S_2) are in two distinct layers, centered at 110 m and 470 m for both across and along-channel tidal current components (Figure 5.12). The highest variance at 110 m (11.32 %) accounts for the along-channel tidal currents which corresponds to the strong shear where upper layer flows northward into the SCS while strong southward flow below into the Sulu Sea during the NEM regime. The M_2 constituents mainly contribute to the variance. At 470 m, across-channel tidal currents account for the highest variance (26.33%) which corresponds with the intense thermocline near-inertial motions suggested to be due to Parametric Subharmonic Instability (PSI) of the diurnal internal tide found near 400 m at northern Mindoro Strait in the SCS, which undergoes similar or higher levels of near-bottom mixing than the Panay sill [Chinn et al., 2012]. Chinn et al. [2012] note that PSI of the internal tide can only occur equatorward of the critical latitude where half the tidal frequency is greater than the local inertial frequency (e.g., 14.52 ° N for K_1 and 13.44 ° N for O_1). Recent observational work under PhilEx program however, has shown convincing evidence that near the critical latitudes the rates of PSI are vastly enhanced and may be a dominant part of the redistribution of energy throughout the internal wave spectrum [Chinn et al., 2012]. The main evidence for PSI was the fortnightly modulation of the near-inertial band, indicating a signal that is often comprised of both upward and

downward propagating waves seen near 400 m [Chinn et al., 2012]. The specifics of the physical forcing that allow it to occur at this particular depth however, are uncertain and more work is needed to fully understand the dynamics at work in Mindoro-Panay Strait. The variance explained by mean tidal across-channel currents is attributed mostly to diurnal tide (O_1) over the Cuyo shelf to the west.

The vertical mean kinetic energy, eddy kinetic energy and tidal kinetic energy are shown in Figure 5.13. In contrast to the kinetic energies from the surface current, the mean eddy and the mean tidal current kinetic energies are relatively small, an order of magnitude less and two orders of magnitude less, respectively than the mean current kinetic energy. The mean current kinetic energy is highest at 520-m depth which corresponds with the hydraulically controlled benthic overflow derived from approximately 400 m deep in the SCS that acts to ventilate the Sulu Sea with little seasonal variance [Tessler et al., 2010]. Both the highest mean eddy and tidal current kinetic energies are at 470 m depth where a PSI-generated near-inertial wave signal was found by Chinn et al. [2012].

The vertical distributions of R_tmke and R_teke are shown in Figure 5.14 with a peak at 110 m and two distinct peaks at 110 m and 470 m, respectively, indicating the dominant tidal activities at shear depth (110 m) during NEM and confirming the PSI-generated thermocline near-inertial motions at 470 m depth discussed above.

5.4.4 Coherent tides

Harmonic analyses of surface and sub-surface current components (zonal and meridional) were performed using T-tide Matlab package [Pawlowicz et al., 2002]. Only the 4 major (K_1, O_1, M_2, and S_2) tidal constituents inferred from sea level were least-square fitted to the observations, along with a constant and a linear trend.

Maps of the observed tidal current ellipses, major axis amplitudes and phases of the four major constituents (K_1, O_1, M_2, and S_2) are shown in Figure 5.15. Tidal ellipses are a compact method used to describe tidal current variance using major and minor axes (Amaj and Amin), inclination and phase. The axes describe the magnitude of the current in 2 orthogonal directions, inclination provides orientation for the axes and phase indicates time lag from Greenwich when the time vector passes the northern semi-major axis. Diurnal peaks are more pronounced over the shelf with amplitudes increasing to the

shallow area. O_1 tidal ellipses are elliptical over the shelf, relatively narrow, and aligned along the channel axes. M_2 has broader and more circular tidal ellipses north of the strait, indicating that rotation is relatively important and/or due to transverse reflection effects. The M_2 major axis amplitudes increase towards the narrow constricted part of the strait. S_2 has similar patterns to M_2 though substantially weaker. The large phase gradients across the HFDR coverage indicate strong reversing tidal pressure gradients and likely locations of accelerated currents and internal tide generation. This is most obvious at the deep channel near the sill and at the edge of the shallow shelf with shoals and promontories.

The vertical structure of the tidal ellipses of 4 major tidal constituents (O_1,K_1, M_2 and S_2) remarkably exhibit two sharp peaks consistent with the location of highest variance explained by the tides at 110 m and 470 m, suggesting contributions from baroclinic tidal current. The coherent portion of the semi-diurnal tide (M_2) dominates at 110 m while the coherent diurnal tide (O_1) dominates at 470 m, consistent with the PSI of the diurnal internal tide found at this depth by Chinn et al. [2012].

5.4.5 Ratio of Incoherent to Coherent Energy

Observed ratios of the averaged diurnal and semi-diurnal power spectra for residual currents and tidal currents are shown in Figure 5.17).

The diurnal frequency band was defined as:

[O_1 + 1/T >diurnal >K_1 – 1/T]

and the semi-diurnal frequency band as:

[M_2 + 1/T >semi-diurnal >S_2 – 1/T]

where T is the record length.

The K_1 constituent dominated the incoherent tidal band, (note the difference in scale, Figure 5.17). Incoherent diurnal energy is strong over the northern region of the channel in between the shoals, slightly further down south towards the sill and again increased into the Sulu Sea (Figure 5.17A). The incoherent semi-diurnal energy is most significant in the more confined regions than the diurnal, between the shoals north of the channel

and further south of the sill. A considerable increase of energy westward is evident, particularly the incoherent diurnal energy (Figure 5.17B). The incoherent portion of the tide is presumably attributable to the surface expression of the internal tide, which seems to be generated near the sill and then topographically steered west over the shallow shelf where incoherent energies are high.

After removing the coherent tidal component as identified by the least squares fit, the diurnal and semi-diurnal tidal bands remained the dominant peaks due to incoherent tidal energy, though K_1 now dominates the diurnal tide band instead of O_1 (Figure 5.18). Chinn et al. [2012] found no evidence to support local or remote forcing mechanism for internal wave generation from their moorings located at both ends of Mindoro-Panay Strait complex. The highly variable internal wave field from HFDR in between those moorings over the Panay Strait, even within the small region covered by HFDR, indicates topographic interactions playing an important role in defining the scales of this variability. Another notable feature in the spectrum is the higher harmonics of diurnal constituents that are still apparent.

Vertically (Figure 5.19), over the channel, incoherent diurnal energy dominates the upper layer and displays a mode 1, two layer structure with a node at 120 m. The incoherent semi-diurnal energy has more complex modal structure with nodes near the surface and at 240 m.

5.5 Summary and Conclusion

The combination of long duration and high resolution in space, depth and time data from multiple instruments (HFDR, ADCP, and SPG) are used to characterize tides in Panay Strait. The dominant tidal components are K_1, O_1, M_2, and S_2. Diurnal tides are pronounced over the shallow shelf while semi-diurnal tides are seen in the channel and the shelfbreak. Vertically, tidal currents are baroclinic. The distributions of incoherent diurnal and semi-diurnal energies vary spatially, which may be related to complex internal tide generation and dissipation in Panay Strait, suggesting that topographic interactions may play an important role.

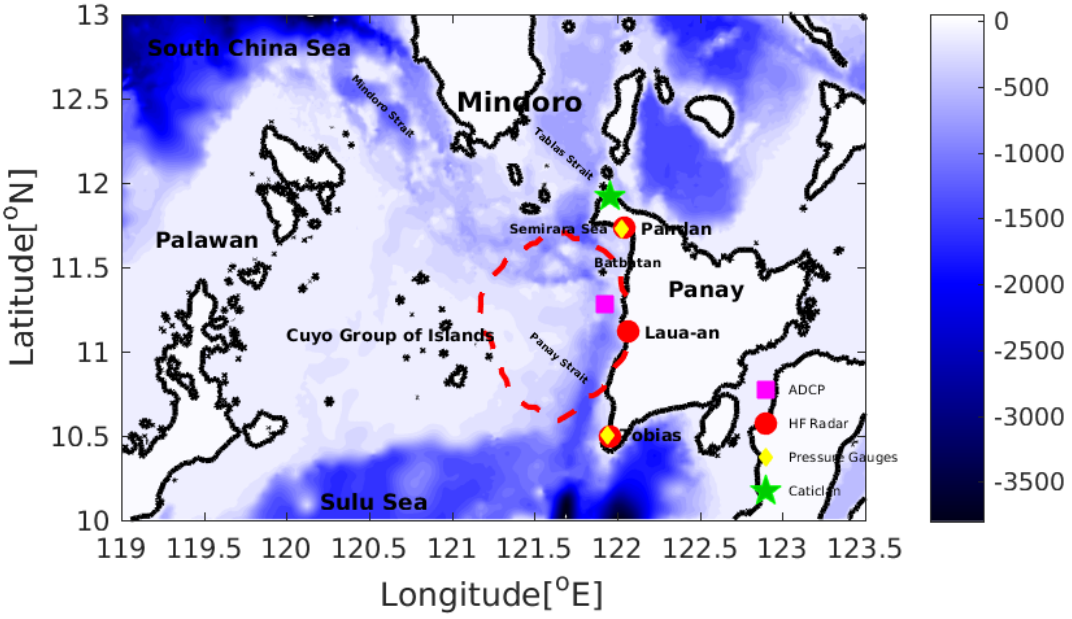

FIGURE 5.1: Map of study area. Bathymetry contours are in meters. The color bar represents color depth in meters. Instrument locations are indicated as follows: HFDR (red circle), moored ADCP (magenta square), and SPG (yellow diamond). The magenta dashed lines indicates 75 % coverage of the HFDR.

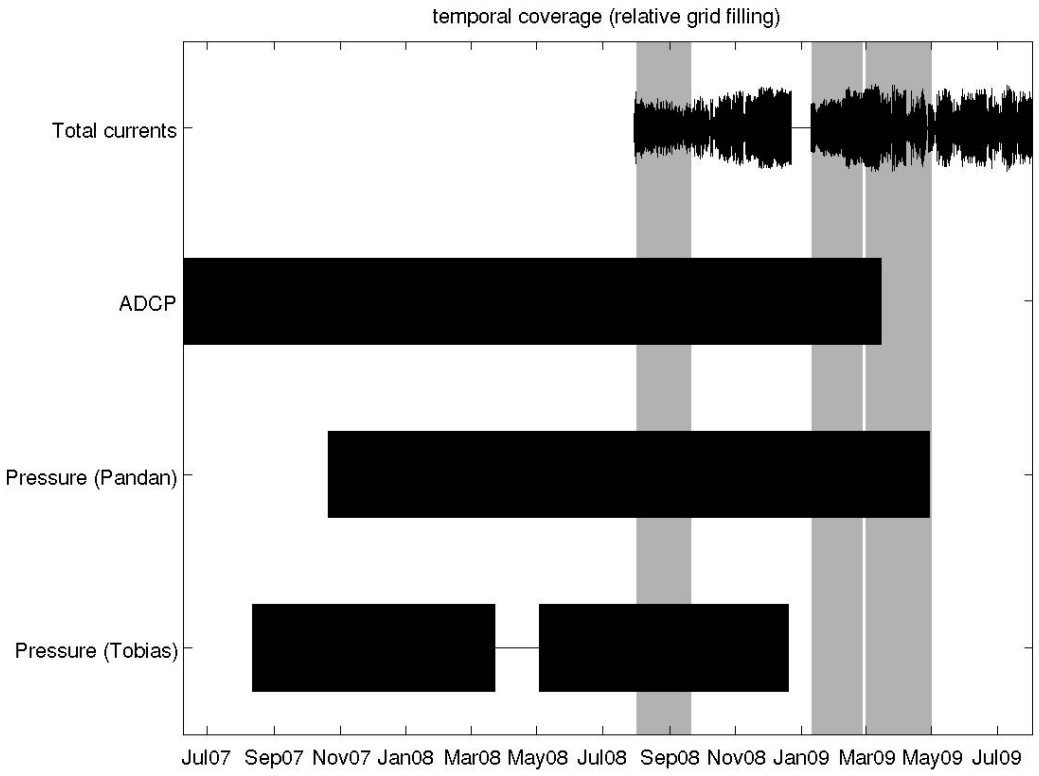

FIGURE 5.2: Temporal coverage of the instruments. The thickness corresponds to the percentage of grid points with data.

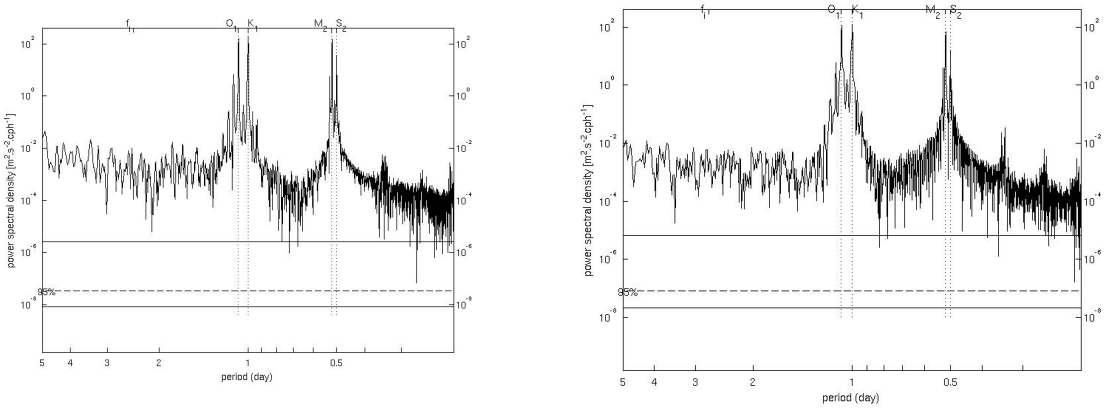

FIGURE 5.3: Power spectral density of the time series overlap of a)Pandan and b) Tobias Fornier SPG.

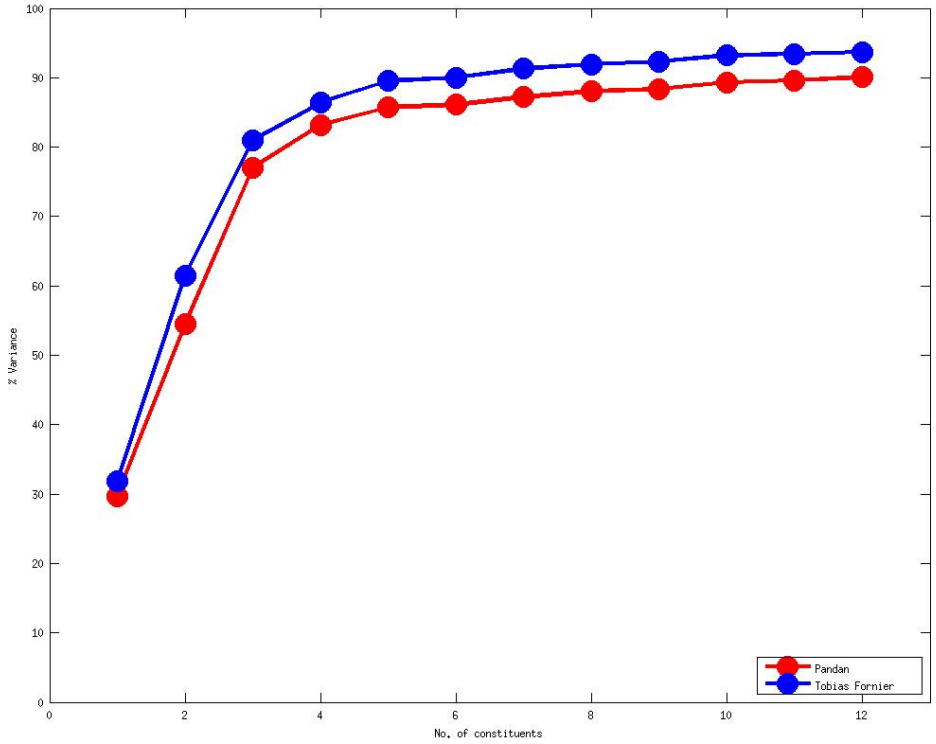

FIGURE 5.4: Increment variance (%) of major tidal constituents. The first 4 marked dots indicate the variance of (1) K_1, (2) K_1 and O_1, (3) K_1, O_1, and M_2, (4) K_1, O_1, M_2, and S_2.

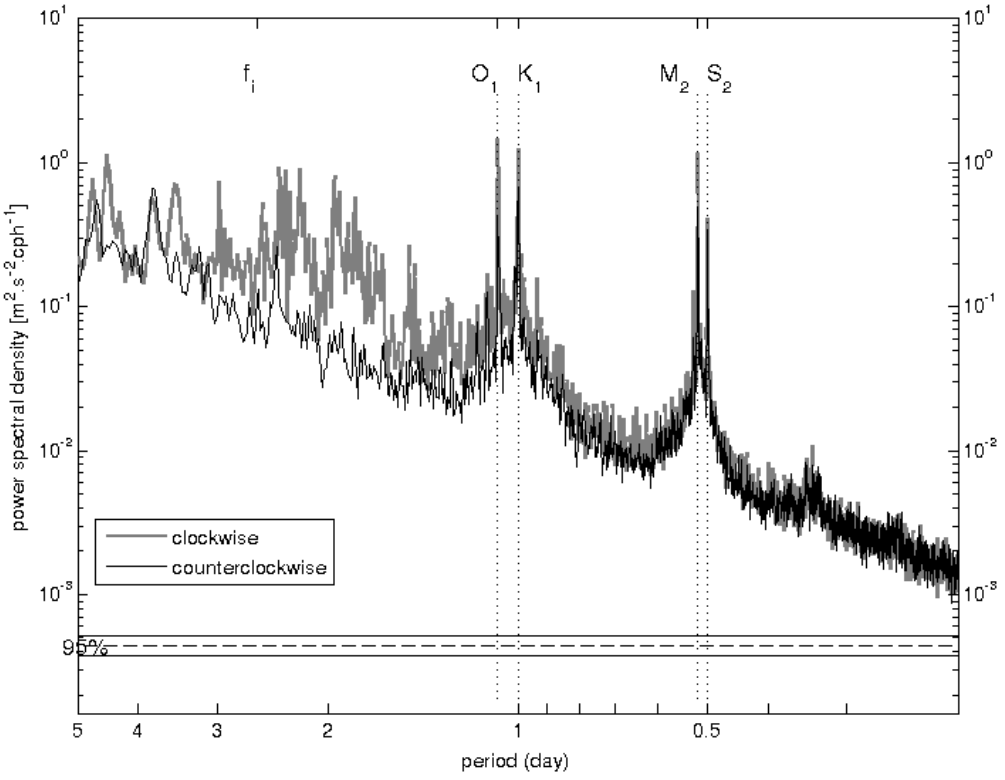

FIGURE 5.5: Rotary power spectra for one year of HFDR data over 212 grid points with more than 75% temporal coverage. Major tidal constituents and inertial frequency, f_i are indicated on the top x-axis, indicated by vertical dotted lines.

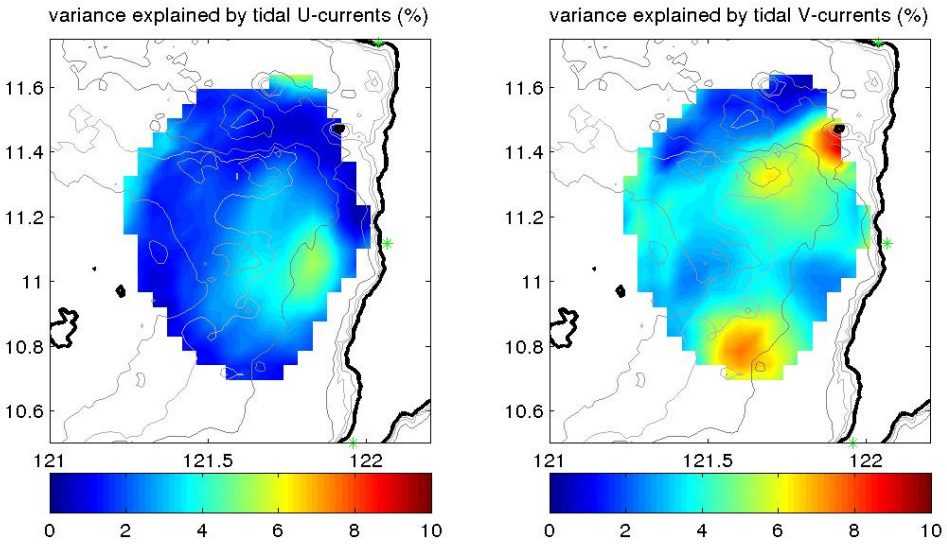

FIGURE 5.6: Variance explained by 4 major tidal constituents (K_1, O_1, M_2, and S_2).

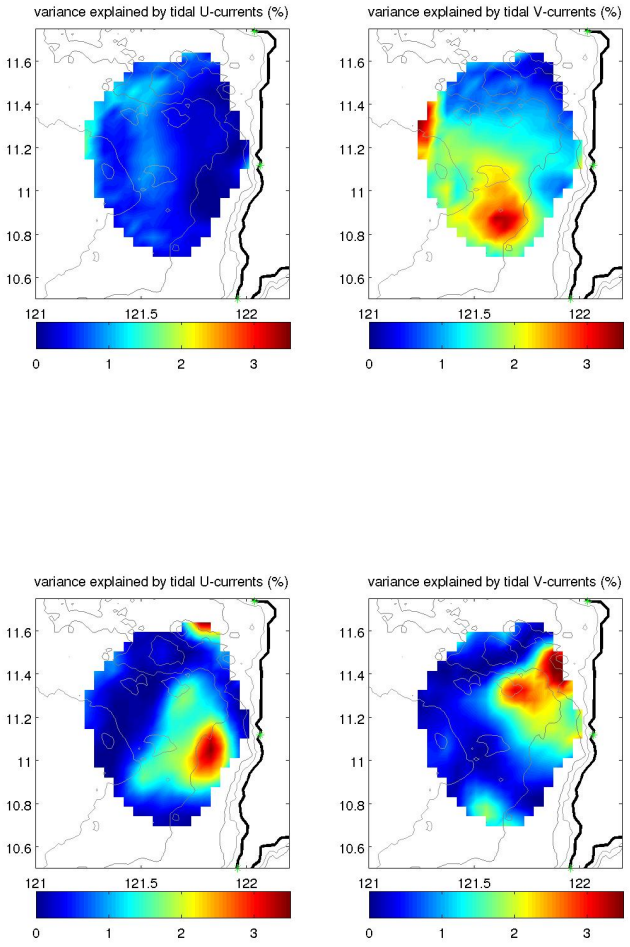

FIGURE 5.7: Variance explained by (top) diurnal and (bottom) semidiurnal tidal constituents.

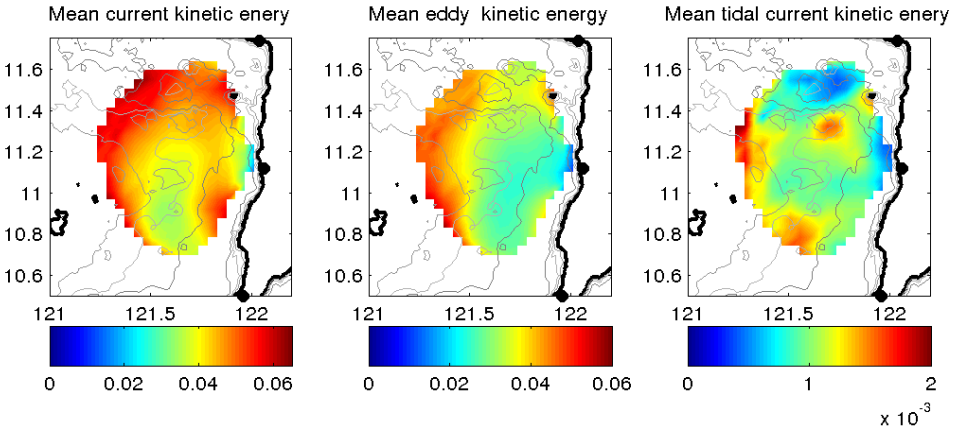

FIGURE 5.8: Mean kinetic energy, eddy kinetic energy and tidal kinetic energy.

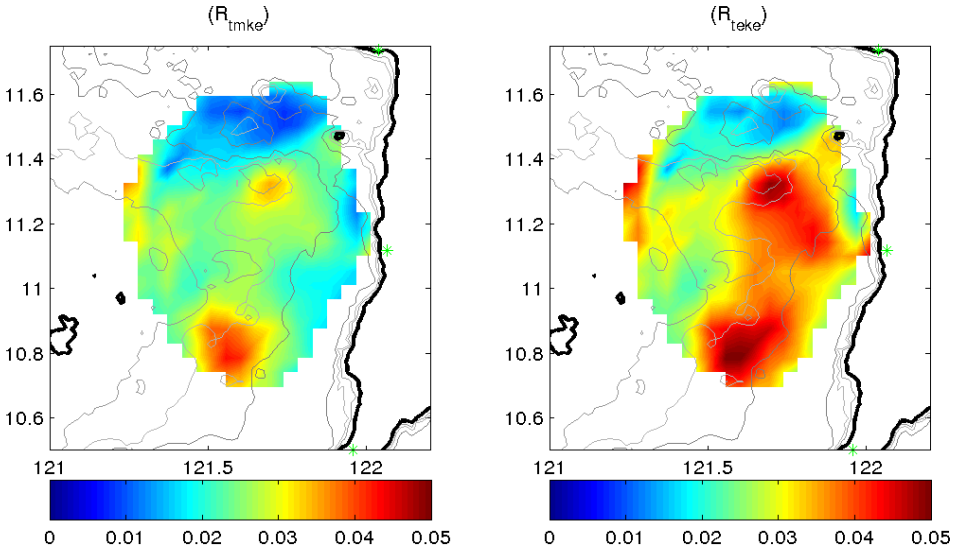

FIGURE 5.9: Contribution of tidal currents to the (A) mean kinetic energy, R_{tmke} and the (B) eddy kinetic energy, R_{teke}.

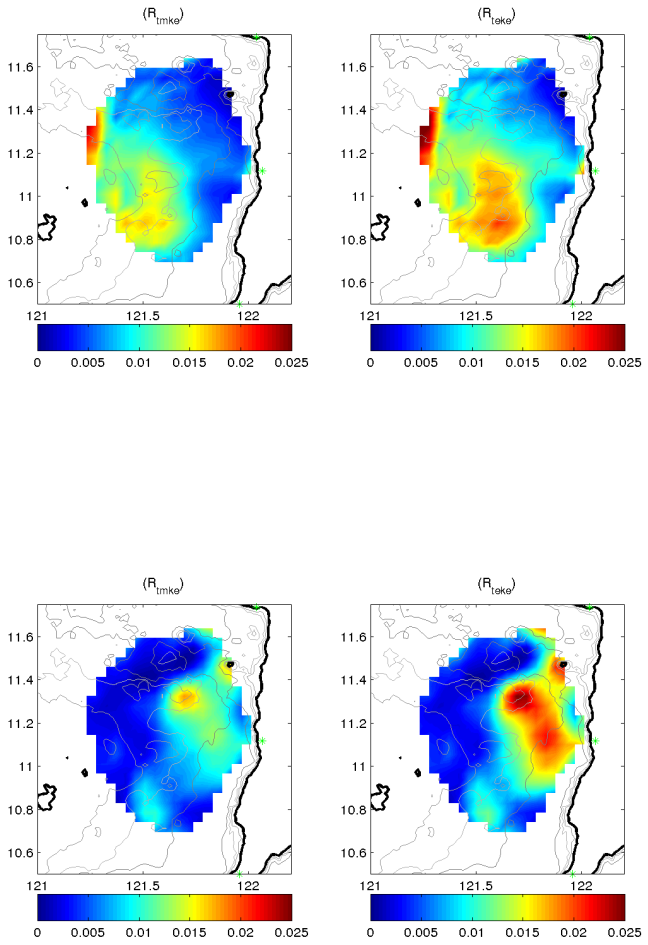

FIGURE 5.10: Contribution of diurnal tidal currents, (top) O_1 and (bottom) M_2 to the total mean kinetic energy, R_{tmke} and the eddy kinetic energy, R_{teke} averaged for over a year.

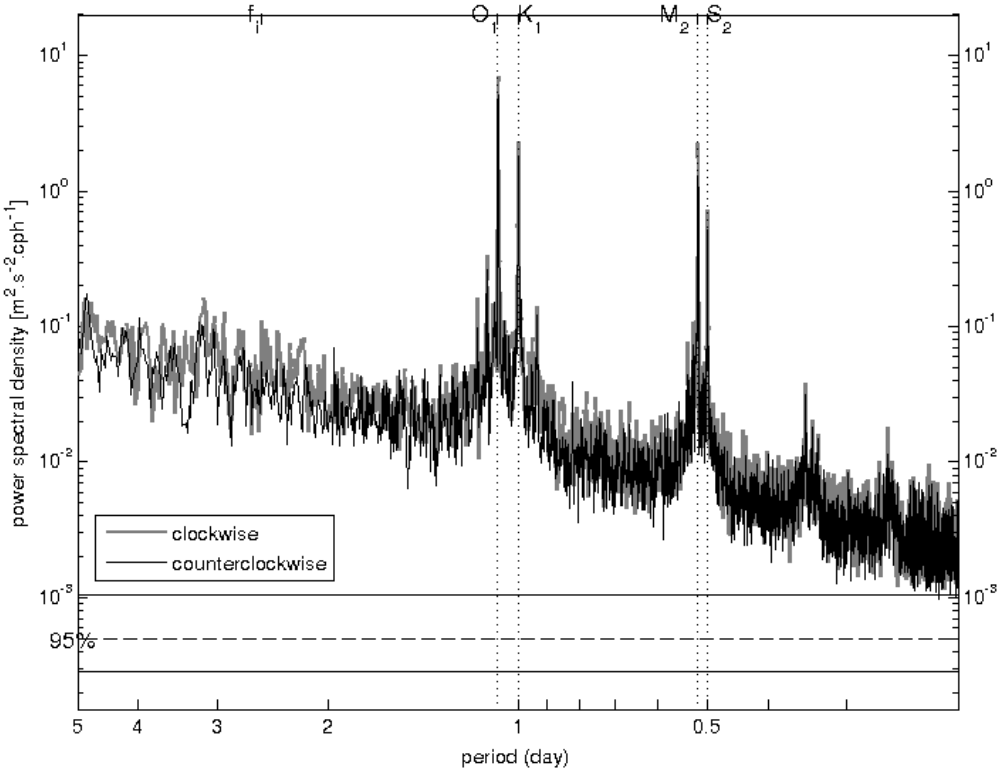

FIGURE 5.11: Rotary power spectra from vertically averaged frequency spectra from ADCP. Major tidal constituents and inertial frequency, f_i are indicated on the top x-axis, indicated by vertical dotted lines.

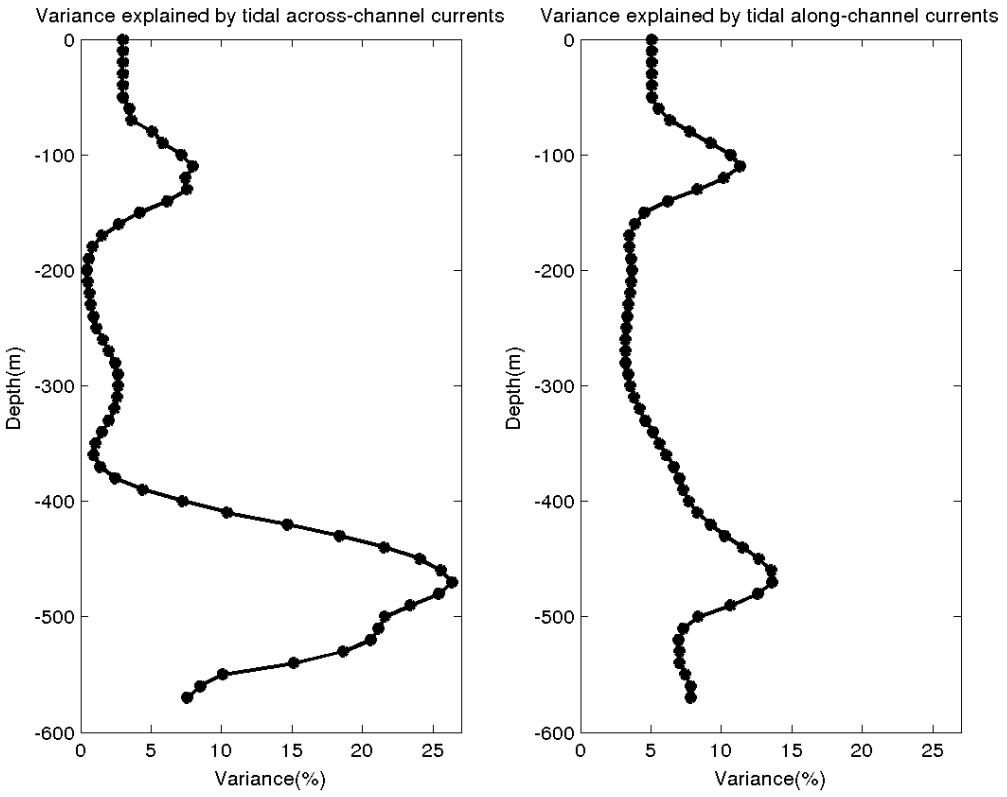

FIGURE 5.12: Variance explained by 4 major constituents (K_1, O_1, M_2, and S_2).

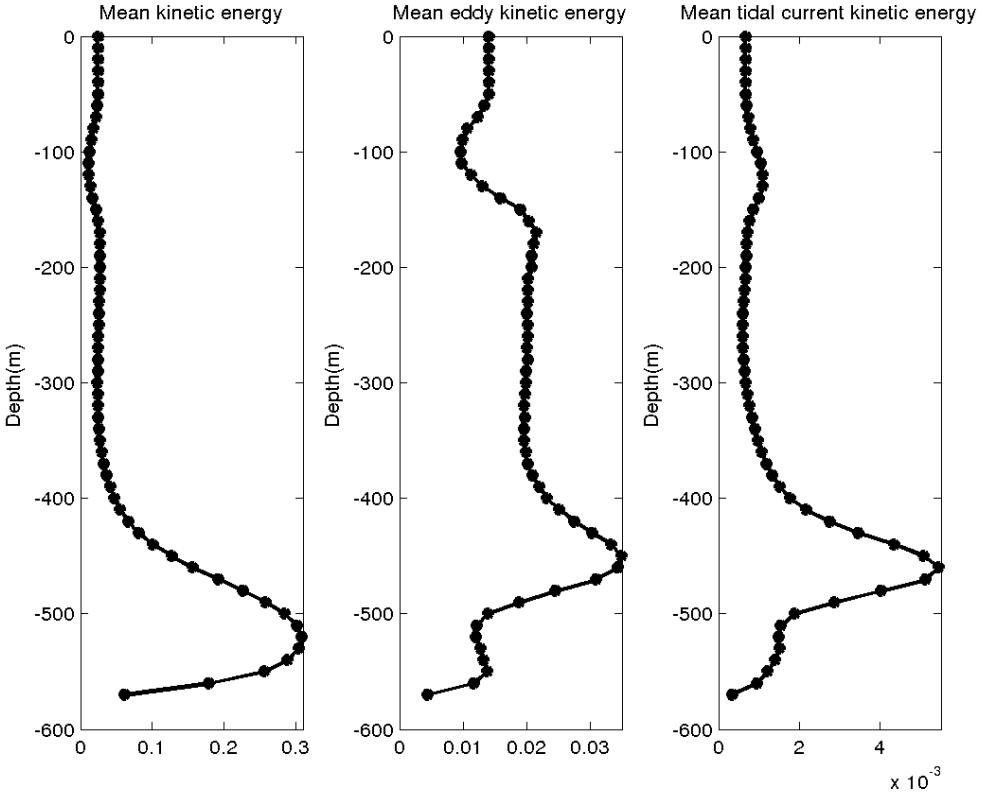

FIGURE 5.13: Mean current, eddy, and tidal current kinetic energies.

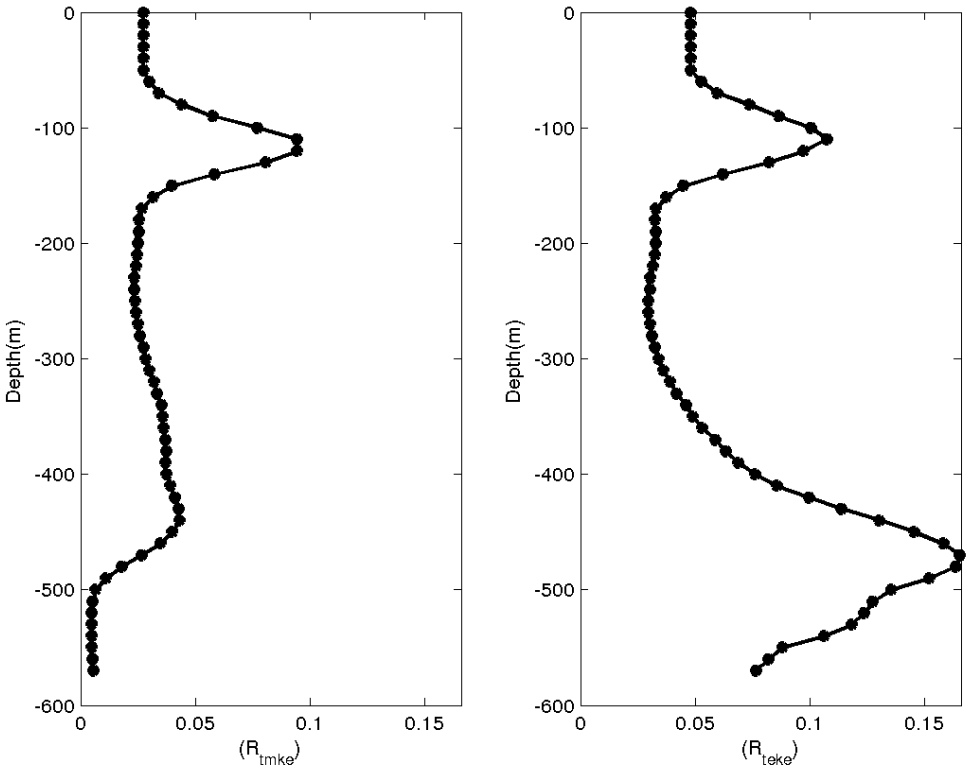

FIGURE 5.14: Contribution of tidal currents to the (A) mean kinetic energy, R_{tmke} and the (B) eddy kinetic energy, R_{teke}.

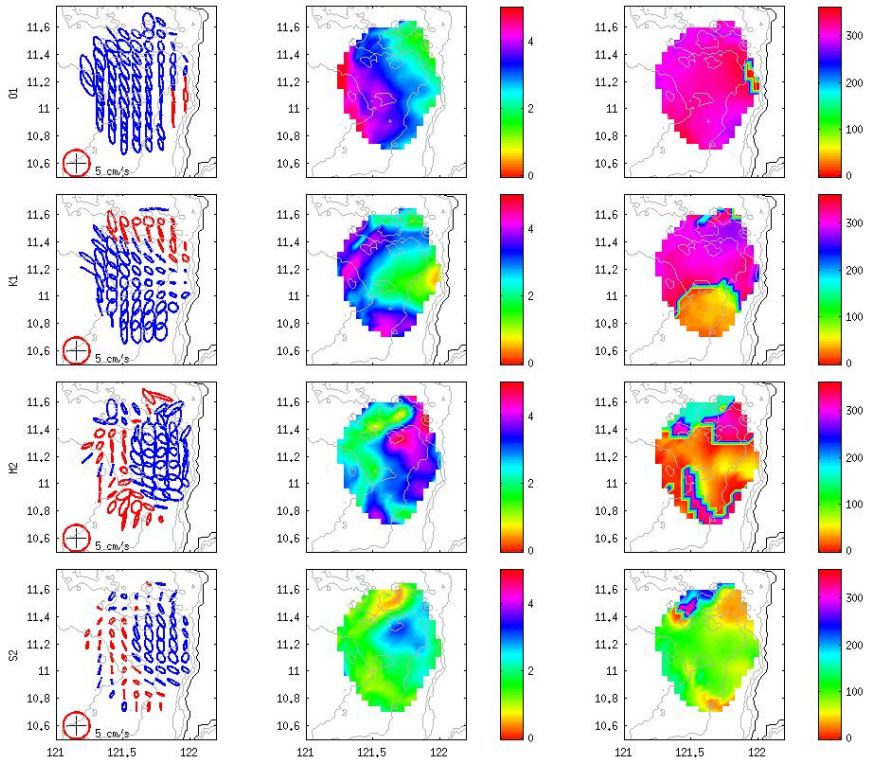

FIGURE 5.15: (top to bottom) O_1, K_1, M_2, and S_2 (bottom) (left column) ellipses, (middle column) major axis amplitude, and (right column) Greenwich phase of HFDR tidal current. Counterclockwise and clockwise ellipses are plotted in red and blue respectively. The phase is defined as the lag of the maximum current (along the northern semi-major axis) with respect to the astronomical phase of M_2 at $0°E$.

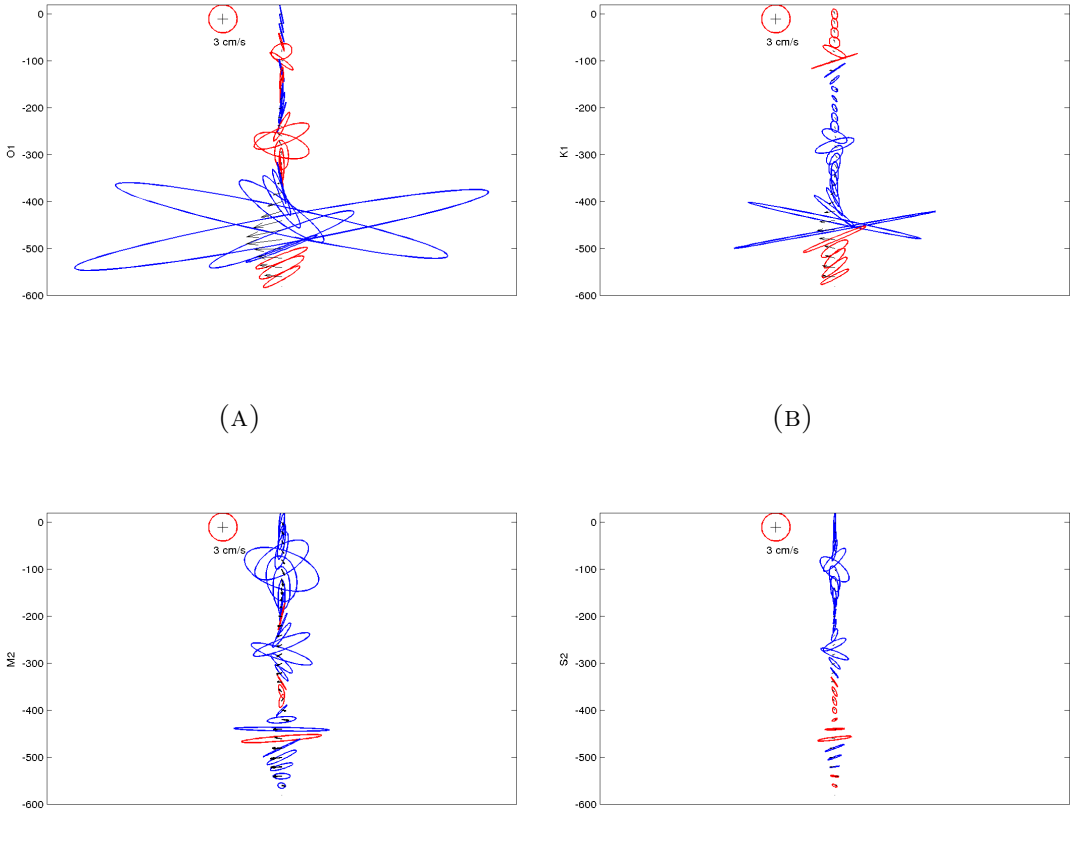

(A) (B)

(C) (D)

FIGURE 5.16: O_1, K_1, (top) M_2, and S_2 (bottom), averaged ellipses with depth Counterclockwise and clockwise ellipses are plotted in red and blue respectively.

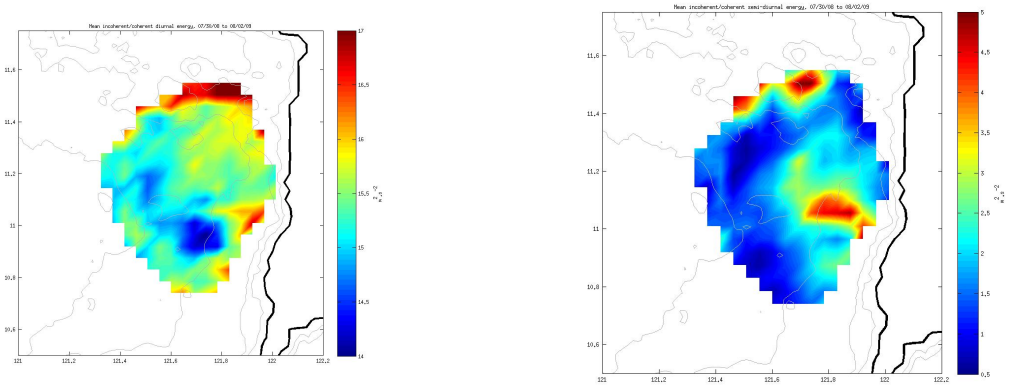

(A) (B)

FIGURE 5.17: Ratio of incoherent to coherent diurnal and semidiurnal tides as observed in surface current record.

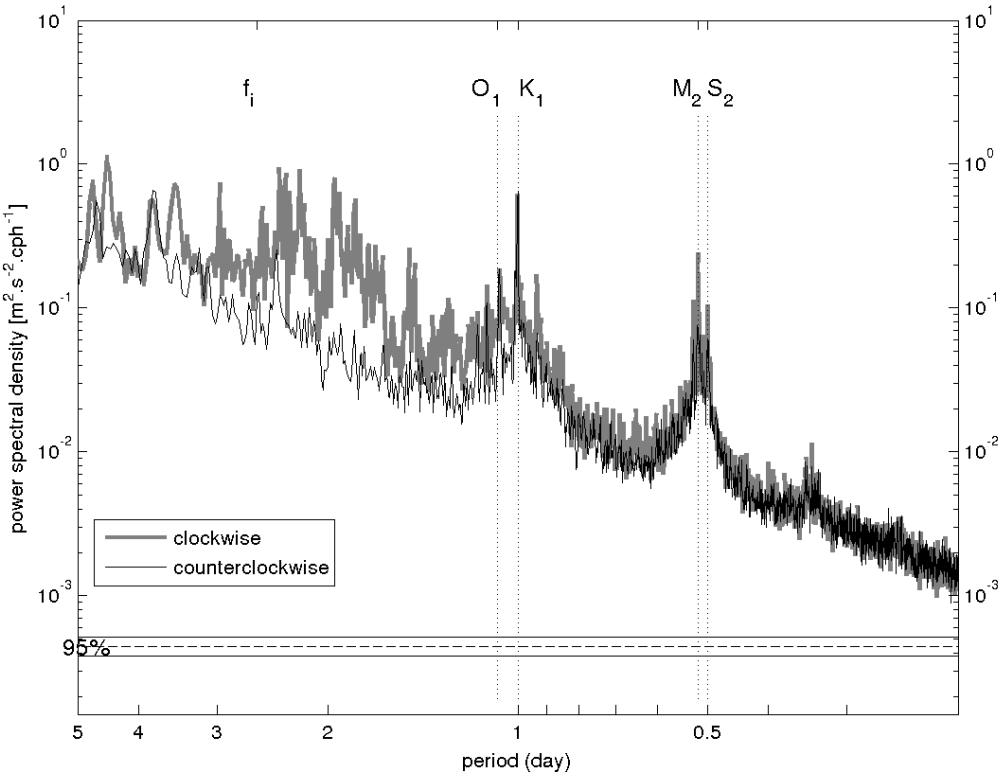

FIGURE 5.18: Rotary power spectra for one year of residual HFDR data over 212 grid points with more than 75 % temporal coverage. Major tidal constituents and inertial frequency, fi are indicated on the top x-axis, indicated by vertical dotted lines.

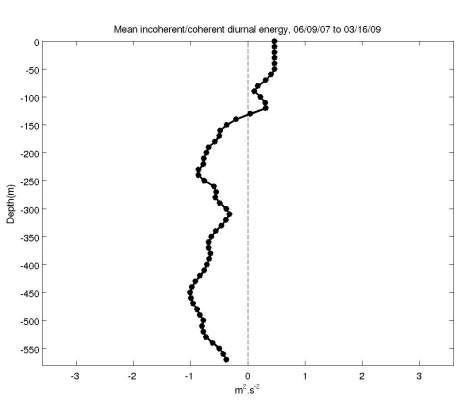

(A) Diurnal

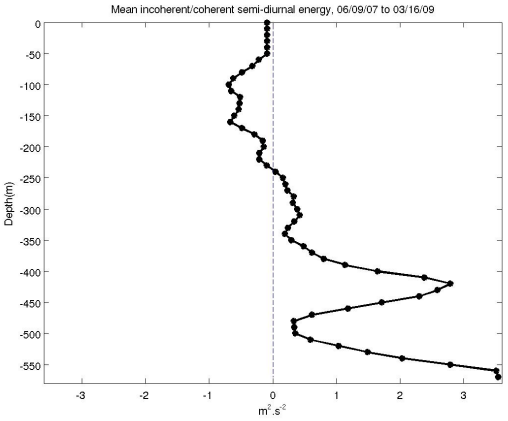

(B) Semidiurnal

FIGURE 5.19: Ratio of incoherent to coherent diurnal and semidiurnal tides as observed in the current profile record.

Chapter 6

Summary and Conclusion

The internal Philippine seas have a unique oceanographic environment, with complex bathymetry confined within the intricate configuration of the Philippine Archipelago connected by multiple array of narrow straits. Strong archipelago throughflow interacts with abrupt changes in bathymetry within and between the basins, swift tidal currents are present, while the island orographic effects on the monsoonal reversing winds generate an energetic wake of eddies through Ekman pumping.

The locally generated mesoscale eddies in the lee of major islands occur west of the Philippines during the stronger and more stable NE monsoon. In the lee of Mindoro and Luzon Islands, steady monsoon winds form stationary lee eddies while episodically strengthened wind jets lead to simultaneous detachment of counter-rotating eddies in the model, with propagation directions dependent on the orientation of the winds during monsoon surges [Pullen et al., 2008].

The installed HFDR array in Panay Island, south of Mindoro, produces time series of 2-D maps of surface currents with high spatial and temporal resolutions that provide observations of the dominant surface flows: the steady Panay coastal (PC) jet and the seasonal cyclonic eddy in the lee of the island. The PC jet is generally northward, in which variations are mainly influenced by the eddy and the presence of the shallow Cuyo shelf. In contrast, the cyclonic eddy is highly seasonal, forms during NE monsoon and intensifies during the peak of the season (December - February) dominating over and occupying the whole HFDR domain. The shift of the eddy close to the coast results in a

more southward mean flow and weaker PC jet while a considerable shift westward leads to an intensified PC jet, which replaces the eastern limb of the eddy.

A synthesis of the HFDR, ADCP, satellite imagery, hydrographic data, and satellite and model-derived winds provide descriptions of the eddy generation and evolution due to Ekman pumping without a strong oceanic flow passing the island. The seasonal evolution of the cyclonic eddy is an oceanic response to the prevailing local wind. The strong wind jets through Tablas Strait, in between Mindoro and Panay and a calm lee generate a positive wind stress curl, which in turn induces divergent surface currents and thermocline uplift. The upwelling of the thermocline due to Ekman pumping reached more than 15 $m.day^{-1}$ based on the snapshots of wind stress curl calculated from COAMPS wind. The instantaneous Ekman pumping velocities indicate a wind-induced divergent Ekman transport, which agrees with the mean divergence calculated from HFDR during the same time period.

Repeated cross-shore surveys revealed the center of the eddy as a doming of isotherms and isopycnals. It corresponds well with the near-surface along-shore current shear from the shipboard ADCP reaching about 130 m, indicating the depth of the eddy. The eddy formation is evident in the mean vorticity, in which the center coincides with the location of the largest Ekman pumping and the doming. The correlation coefficient of R=0.50 and R=0.67 between divergence and vorticity with Ekman pumping velocity, respectively indicate the significant link between these terms.

The temporal variation of each term in the vorticity balance equation averaged over the specified box shows that the evolution of the vorticity within the vortex core generally is dominated by frictional processes. The frictional forcing is induced dominantly by the wind stress curl, driving the cyclonic vorticity growth after a time lag of about 10 days, while the β term causes the cyclonic eddy to propagate westward.

By comparing the temporal variation of thermocline depth anomaly (proportional to vorticity) with the integrals of the Ekman pumping velocity (proportional to wind stress curl) and divergence, we find a robust mechanism linking cumulative local wind stress curl to eddy kinetic energy. Further, unlike vorticity, the Ekman divergence is an instantaneous response to the positive wind stress curl forcing.

Once generated, the ocean vorticity responds effectively to fluctuating local wind magnitude and direction, and to the β term causing the cyclonic eddy to propagate westward. Eddy shedding however, was not observed unlike in the lee of Luzon and Mindoro [Pullen et al., 2008] due to the size of the eddy and the limited HFDR coverage. Shedding is unlikely to occur due to the presence of low lying Cuyo Group of Islands and extensive shallow reefs that may retard or inhibit further cross-shelf propagation of the eddy by bottom friction [Pringle, 2001].

A smaller band of positive wind stress curl, downwind off the northern tip of Panay headland (Figure 3.10 in Chapter 3) also suggests Ekman pumping as mechanism that generates the cyclonic PT eddy. Similar to PL eddy, this feature may be considered as persistent and permanent during the NE monsoon regime. Due to limited HFDR coverage, PT eddy was only observed from the shipboard ADCP in which velocity profiles indicate an Ekman dynamics. Synoptic measurement of currents revealed a tidal oscillation of the PT eddy, which moves towards the coast during the flood tide while away from the coast during the ebb tide. A corresponding deepening (100 M) during flood tide and shoaling (50 m) during ebb tide was also observed.

The enhanced chlorophyll concentration coincide with the intensive Ekman pumping in terms of location and time for both PL and PT eddy. These suggest that the Ekman pumping that spin-up these geostrophic eddies is important to the blooming of phytoplankton. These eddies formed in the lee of the island and headland therefore have important implications in the determination of locations of high primary productivity and fisheries.

The barotropic tidal flows in Panay Strait reflect the effect of complex bathymetry as it accelerates through shallow areas and topographic constrictions. Diurnal tides are pronounced over the shallow shelf while semi-diurnal tide on channel and shelfbreak. Vertically, tidal currents are baroclinic. A complex internal tide generation and dissipation indicate the important role of topographic interactions. Further, Panay Strait is exposed to mesoscale eddies and upwelling. This seasonally varying dynamics may affect the stratification and thus the generation and propagation of internal tides in this area.

Bibliography

Apel, John R; Holbrook, James R; Liu, Antony K, and Tsai, John J. The sulu sea internal soliton experiment. *Journal of Physical Oceanography*, 15(12):1625–1651, 1985.

Barton, Eric D; Argote, María Luisa; Brown, Juan; Kosro, P Michael; Lavin, Miguel; Robles, Jose M; Smith, Robert L; Trasviña, Armando, and Velez, Hector S. Supersquirt: dynamics of the gulf of tehuantepec, mexico. *Oceanography*, 6(1):23–30, 1993.

Barton, Eric D; Basterretxea, Gotzon; Flament, Pierre; Mitchelson-Jacob, E Gay; Jones, Bethan; Arístegui, Javier, and Herrera, Felix. Lee region of gran canaria. *Journal of Geophysical Research: Oceans (1978–2012)*, 105(C7):17173–17193, 2000.

Caldeira, Rui; Stegner, Alexandre; Couvelard, Xavier; Araújo, Isabel B; Testor, Pierre, and Lorenzo, Alvaro. Evolution of an oceanic anticyclone in the lee of madeira island: In situ and remote sensing survey. *Journal of Geophysical Research: Oceans*, 119(2): 1195–1216, 2014.

Calil, Paulo HR; Richards, Kelvin J; Jia, Yanli, and Bidigare, Robert R. Eddy activity in the lee of the hawaiian islands. *Deep Sea Research Part II: Topical Studies in Oceanography*, 55(10):1179–1194, 2008.

Campos, WL; II, PD Beldia; Villanoy, CL, and Aliño, PM. Using ichthyoplankton distribution in selecting sites for an mpa network in the sulu sea, philippines. In *Proceedings of the 11th International Coral Reef Symposium, Ft. Lauderdale, Florida*, volume 1, pages 431–435, 2008.

Chavanne, C; Janeković, Ivica; Flament, P; Poulain, P-M; Kuzmić, Milivoj, and Gurgel, K-W. Tidal currents in the northwestern adriatic: High-frequency radio observations and numerical model predictions. *Journal of Geophysical Research: Oceans (1978–2012)*, 112(C3), 2007.

Chavanne, Cédric; Flament, Pierre; Lumpkin, Rick; Dousset, Bénédicte, and Bentamy, Abderrahim. Scatterometer observations of wind variations induced by oceanic islands: Implications for wind-driven ocean circulation. *Canadian Journal of Remote Sensing*, 28(3):466–474, 2002.

Chinn, Brian S; Girton, James B, and Alford, Matthew H. Observations of internal waves and parametric subharmonic instability in the philippines archipelago. *Journal of Geophysical Research: Oceans (1978–2012)*, 117(C5), 2012.

Couvelard, X; Caldeira, RMA; Araújo, IB, and Tomé, R. Wind mediated vorticity-generation and eddy-confinement, leeward of the madeira island: 2008 numerical case study. *Dynamics of Atmospheres and Oceans*, 58:128–149, 2012.

Dong, Changming; Mavor, Timothy; Nencioli, Francesco; Jiang, Songnian; Uchiyama, Yusuke; McWilliams, James C; Dickey, Tommy; Ondrusek, Michael; Zhang, Hongchun, and Clark, Dennis K. An oceanic cyclonic eddy on the lee side of lanai island, hawai'i. *Journal of Geophysical Research: Oceans*, 114(C10), 2009.

Emery, WJ and Thomson, RE. Data analysis methods in physical oceanography elsevier. *Amsterdam 638pp*, 2004.

Gaberšek, Saša and Durran, Dale R. Gap flows through idealized topography. part i: Forcing by large-scale winds in the nonrotating limit. *Journal of the atmospheric sciences*, 61(23):2846–2862, 2004.

Gaberšek, Saša and Durran, Dale R. Gap flows through idealized topography. part ii: Effects of rotation and surface friction. *Journal of the atmospheric sciences*, 63(11): 2720–2739, 2006.

Gill, Adrian E. *Atmosphere-ocean dynamics*, volume 30. Academic press, 1982.

Girton, James B; Chinn, Brian S, and Alford, Matthew H. Internal wave climates of the philippine seas. *Oceanography*, 2011.

Gonella, Joseph. A rotary-component method for analysing meteorological and oceanographic vector time series. In *Deep Sea Research and Oceanographic Abstracts*, volume 19, pages 833–846. Elsevier, 1972.

Gordon, Arnold L and Villanoy, Cesar L. The oceanography of the philippine archipelago. *Oceanography*, page 13, 2011.

Han, Weiqing; Moore, Andrew M; Levin, Julia; Zhang, Bin; Arango, Hernan G; Curchitser, Enrique; Di Lorenzo, Emanuele; Gordon, Arnold L, and Lin, Jialin. Seasonal surface ocean circulation and dynamics in the philippine archipelago region during 2004–2008. *Dynamics of Atmospheres and Oceans*, 47(1):114–137, 2009.

Hanawa, Kimio and Talley, Lynne D. Mode waters. *International Geophysics Series*, 77: 373–386, 2001.

Hurlburt, Harley E; Metzger, E Joseph; Sprintall, Janet; Riedlinger, Shelley N; Arnone, Robert A; Shinoda, Toshiaki, and Xu, Xiaobiao. Circulation in the philippine archipelago simulated by 1/12 degrees and 1/25 degrees global hycom and eas ncom. *Oceanography*, 2011.

Jackson, Christopher R; Arvelyna, Yessy, and Asanuma, Ichio. High-frequency nonlinear internal waves around the philippines. *Oceanography*, 2011.

Jia, Y; Calil, PHR; Chassignet, EP; Metzger, EJ; Potemra, JT; Richards, KJ, and Wallcraft, Alan J. Generation of mesoscale eddies in the lee of the hawaiian islands. *Journal of Geophysical Research: Oceans (1978–2012)*, 116(C11), 2011.

Jiménez, B; Sangrà, P, and Mason, E. A numerical study of the relative importance of wind and topographic forcing on oceanic eddy shedding by tall, deep water islands. *Ocean Modelling*, 22(3):146–157, 2008.

Jones, Burton H; Lee, Craig M; Toro-Farmer, Gerardo; Boss, Emmanuel; Gregg, Michael C, and Villanoy, Cesar L. Tidally driven exchange in an archipelago strait: Biological and optical responses. *Oceanography*, 24(1):142, 2011.

Kersalé, Marion; Doglioli, AM, and Petrenko, AA. Sensitivity study of the generation of mesoscale eddies in a numerical model of hawaii islands. *Ocean Science*, 7(3):277–291, 2011.

Lumpkin, CF. Eddies an currents of the hawaiian islands. *Ph.D. thesis. Sch. of Ocean and Earth Sci. and Technol. Univ. of Hawaii at Manoa*, page 282, 1998.

Lyon, Bradfield; Cristi, Hannagrace; Verceles, Ernesto R; Hilario, Flaviana D, and Abastillas, Rusy. Seasonal reversal of the enso rainfall signal in the philippines. *Geophysical research letters*, 33(24), 2006.

May, Paul W; Doyle, James D; Pullen, Julie D, and David, Laura T. Two-way coupled atmospher-ocean modeling of the philex intensive observational periods. Technical report, DTIC Document, 2011.

McClean, Julie L; Ivanova, Detelina P, and Sprintall, Janet. Remote origins of interannual variability in the indonesian throughflow region from data and a global parallel ocean program simulation. *Journal of Geophysical Research: Oceans*, 110(C10), 2005.

Pawlowicz, Rich; Beardsley, Bob, and Lentz, Steve. Classical tidal harmonic analysis including error estimates in matlab using t_tide. *Computers & Geosciences*, 28(8): 929–937, 2002.

Piedeleu, Marc; Sangrà, Pablo; Sánchez-Vidal, Anna; Fabrés, Joan; Gordo, Carmen, and Calafat, Antoni. An observational study of oceanic eddy generation mechanisms by tall deep-water islands (gran canaria). *Geophysical Research Letters*, 36(14), 2009.

Press, William H; Teukolsky, Saul A; Vetterling, William T, and Flannery, Brian P. *Numerical recipes in C*, volume 2. Cambridge university press Cambridge, 1996.

Pringle, James M. Cross-shelf eddy heat transport in a wind-free coastal ocean undergoing winter time cooling. *Journal of Geophysical Research: Oceans*, 106(C2):2589–2604, 2001.

Pullen, Julie; Doyle, James D; May, Paul; Chavanne, Cedric; Flament, Pierre, and Arnone, Robert A. Monsoon surges trigger oceanic eddy formation and propagation in the lee of the philippine islands. *Geophysical Research Letters*, 35(7), 2008.

Pullen, JulIe D; Gordon, Arnold L; Sprintall, Janet; Lee, Craig M; Alford, Matthew H; Doyle, James D, and May, Paul W. Atmospheric and oceanic processes in the vicinity of an island strait. Technical report, DTIC Document, 2011.

Rypina, Irina I; Pratt, Lawrence J; Pullen, Julie; Levin, Julia, and Gordon, Arnold L. Chaotic advection in an archipelago*. *Journal of Physical Oceanography*, 40(9):1988–2006, 2010.

Sangrà, Pablo; Pascual, Ananda; Rodríguez-Santana, Ángel; Machín, Francisco; Mason, Evan; McWilliams, James C; Pelegrí, Josep L; Dong, Changming; Rubio, Anna; Arístegui, Javier, and others, . The canary eddy corridor: A major pathway for long-lived eddies in the subtropical north atlantic. *Deep Sea Research Part I: Oceanographic Research Papers*, 56(12):2100–2114, 2009.

Sprintall, Janet; Gordon, Arnold L; Flament, Pierre, and Villanoy, Cesar L. Observations of exchange between the south china sea and the sulu sea. *Journal of Geophysical Research: Oceans (1978–2012)*, 117(C5), 2012.

Tessler, Zachary D; Gordon, Arnold L; Pratt, Larry J, and Sprintall, Janet. Transport and dynamics of the panay sill overflow in the philippine seas*. *Journal of Physical Oceanography*, 40(12):2679–2695, 2010.

Thompson, Donald R and Beal, Robert C. Mapping high-resolution wind fields using synthetic aperture radar. *Johns Hopkins APL Technical Digest*, 21(1):58–67, 2000.

Trasviña, A; Barton, ED; Brown, J; Velez, HS; Kosro, P Michael, and Smith, Robert Lloyd. Offshore wind forcing in the gulf of tehuantepec, mexico: The asymmetric circulation. *Journal of Geophysical Research: Oceans (1978–2012)*, 100(C10): 20649–20663, 1995.

Tsing-Chang, Chen and Weng, Shu-Ping. Some effects of the intraseasonal oscillation on the equatorial waves over the western tropical pacific-south china sea region during the northern summer. *Monthly weather review*, 124(4):751, 1996.

Wang, Bin; Wu, Renguang, and Lau, KM. Interannual variability of the asian summer monsoon: contrasts between the indian and the western north pacific-east asian monsoons*. *Journal of Climate*, 14(20):4073–4090, 2001.

Wang, Guihua; Su, Jilan, and Chu, Peter C. Mesoscale eddies in the south china sea observed with altimeter data. *Geophysical Research Letters*, 30(21), 2003.

Wang, Guihua; Chen, Dake, and Su, Jilan. Winter eddy genesis in the eastern south china sea due to orographic wind jets. *Journal of Physical Oceanography*, 38(3):726–732, 2008.

Wang, Jing; Qi, Yiquan, and Jones, Ian SF. An analysis of the characteristics of chlorophyll in the sulu sea. *Journal of Marine Systems*, 59(1):111–119, 2006.

Weber, Rudolf O and Kaufmann, Pirmin. Relationship of synoptic winds and complex terrain flows during the mistral field experiment. *Journal of Applied Meteorology*, 37 (11):1486–1496, 1998.

Webster, Peter J; Magana, Vo Oo; Palmer, TN; Shukla, J; Tomas, RA; Yanai, M u, and Yasunari, T. Monsoons: Processes, predictability, and the prospects for prediction. *Journal of Geophysical Research: Oceans (1978–2012)*, 103(C7):14451–14510, 1998.

White, Warren B; Tourre, Yves M; Barlow, Mathew, and Dettinger, Mike. A delayed action oscillator shared by biennial, interannual, and decadal signals in the pacific basin. *Journal of Geophysical Research: Oceans*, 108(C3), 2003.

Whiteman, C David and Doran, J Christopher. The relationship between overlying synoptic-scale flows and winds within a valley. *Journal of Applied Meteorology*, 32 (11):1669–1682, 1993.

Wrytki, K. Physical oceanography of the south east asian waters: Naga report. *University of California*, 1961.

Yoshida, Sachiko; Qiu, Bo, and Hacker, Peter. Wind-generated eddy characteristics in the lee of the island of hawaii. *Journal of Geophysical Research: Oceans (1978–2012)*, 115(C3), 2010.

Zhang, B; Curchister, E; Levin, JC; Arango, HG, and Han, W. Modeling in the internal tides and energy flux in the sulu sea and adjacent area, 2010.